DOCTOR OF PHILOSOPHY

Multiscale Modelling of Cancer Response to Viral Therapy

Alzahrani, Talal Ali Mohammed

Award date:
2020

Multiscale Modelling of Cancer Response to Viral Therapy

Talal Ali Mohammed Alzahrani

Mathematics

University of Dundee

This dissertation is submitted for the degree of

Doctor of Philosophy

February 2020

Contents

List of Figures

List of Tables

Acknowledgements

First and foremost, I would like to thank the almighty God (Allah) for everything, without whom I would never have obtained a PhD. Second, i would like to acknowledge the support received from the Saudi Arabian Cultural Bureau in the UK on behalf of Umm Al Qura University. A special thanks goes for my PhD supervisor, Dr. Dumitru Trucu, as well as to all our faculty in the Division of Mathematics at University of Dundee for their support and kindness during my PhD studies. Last, but not least, special thanks go to my family and my friends who have supported and encouraged me during my program.

Dedication

I would like to dedicate this thesis to my mother, my wife, my daughter (Kinda), my sisters, my brothers and the soul of (my father, my father-in-law and my sister's husband) for their endless love and support.

To my mother, you will always have a special place in my heart!!

To my wife, every day with you is full of love and affection than the day before!!

To Kinda, you are the pleasant memories of the past, the happy moments of the present, and the hope of the future!!

No words are enough to express my gratitude and love.

Declaration

I declare that the following thesis is my own composition and that it has not been submitted before in application for a higher degree.

Talal Alzahrani

Certification

This is to certify that Talal Alzahrani has complied with all the requirements for the submission of this Doctor of Philosophy thesis to the University of Dundee.

Dr. Dumitru Trucu

Publications

1. Alzahrani, T., Eftimie, R., Trucu, D., (2019), Multiscale modelling of cancer response to oncolytic viral therapy, *Mathematical Biosciences* 310, pp 76-95, doi.org/10.1016/j.mbs.2018.12.018

2. Alzahrani, T., Eftimie, R., Trucu, D (2019), Multiscale Moving Boundary Modelling of Cancer Interactions with a Fusogenic Oncolytic Virus: the Impact of Syncytia Dynamics, *Mathematical Biosciences (21pp), Accepted, manuscript number:* $MBS-2019-275R1$.

Abstract

Oncolytic viruses (OV) are viruses that can replicate selectively within cancer cells and destroy them. While the past few decades have seen significant progress related to the use of these viruses in clinical contexts, the degree of success of viral oncolytic therapies is currently dampened by the relatively low level of understanding of the complex spatio-temporal tumour-OV dynamic interactions, whose main characteristics are yet to be deciphered. In this work, we present a novel multiscale moving boundary modelling for the tumour-OV interactions, which is based on coupled systems of partial differential equations both at macro-scale (tissue-scale) and at micro-scale (cell-scale) that are connected through a double feedback link. At the macro-scale, we account for the coupled dynamics of uninfected cancer cells, OV-infected cancer cells, extracellular matrix (ECM) and oncolytic viruses. At the same time, at the micro scale, we focus on essential dynamics of urokinase plasminogen activator (uPA) system which is one of the important proteolytic systems responsible for the degradation of the ECM, with notable influence in cancer invasion. While sourced by the cancer cells that arrive during their macro-dynamics within the outer proliferating rim of the tumour, the uPA micro-dynamics is crucial in determining the movement of the macro-scale tumour boundary (both in terms of direction and displacement magnitude).

In this investigation, we consider several scenarios for the macro-scale tumour-

OV interactions. While assuming the usual modelling context of reaction-diffusion-taxis coupled PDEs, these scenarios gradually explore the influence of the ECM taxis over the tumour - OV interaction, in the form of haptotaxis of both uninfected and infected cells populations as well as the indirect ECM taxis for the oncolytic virus. The complex tumour-OV interactions are also investigated numerically through the development a new multiscale moving boundary computational framework. Furthermore, as there is increasing biological evidence that a sub-class of viruses that contain fusion proteins (triggering the formation of syncytia) can lead to better oncolytic results, we continue our investigation by exploring several scenarios for the complex dynamics of syncytia formation in the presence of tumour - fusogenic virus interactions. Since the details of the tumour dynamics following syncytia formation are not fully understood, we consider a modelling and computational approach to describe the effect of a fusogenic oncolytic virus within the multiscale dynamics of a spreading tumour. For the parameter regimes that we considered, the numerical investigation shows that a tumour reduction can be obtained in terms of choosing different viral burst rates and death rates for individually-infected tumour cells in a comparison with syncytia structures. Furthermore, we investigate the impact that the type of syncytia diffussive transport (i.e., with either constant or density dependent coefficient) has upon the outcome of the oncolytic viral therapy. Finally, we study the local existence and uniqueness of solutions by using Banach fixed point theorem for several macroscopic and microscopic models. To achieve this, we take advantage of essential mathematical concepts involving the theory of semigroups, the sectorial operator, the lipschitzianity properties, space embeddings for Holder continuous functions, the triangle inequality, the continuity of the norm, and the property of the Lebesgue Integral and Bochner Integral.

Chapter 1

General Introduction

1.1 Thesis Outline

The main purpose of this thesis is to explore the dynamic interactions between tumour growth and oncolytic virus (OV) by accounting for the first time for key interlinked activities happening at both cell- and tissue- scales. To that end, we extend the moving boundary multiscale framework first introduced in Trucu et al. (2013) to describe the genuinely multiscale nature of tumour-OV interaction.

In Chapter 2 we will introduce the general multiscale moving boundary framework (Trucu et al., 2013) and how this approach can be applicable in our work. This approach is used to describe tumour invasion in the presence of matrix degrading enzymes (MDEs) of tissue. The mathematical modelling in this framework is based on coupled systems of partial differential equations at both macroscopic and microscopic scales. The framework considers at the macro-scale (tissue-scale) the dynamics of cancer cell population and its interaction with the surrounding extracellular matrix ECM, while at the micro-scale (cell-scale) they account for MDEs

dynamics within the tumour boundary outer rim.

In Chapter 3 we will study the cancer responses to oncolytic viral therapy. To that end, we will first extend the general framework of the moving boundary multi-scale technique (Trucu et al., 2013) to accommodate the cancer invasion interactions in the presence of oncolytic virus. At the macro-scale, we will investigate three distinct scenarios of tumour-OV interactions in terms of ECM haptotaxis directional motility interactions with different types of cancer cells and OV, namely,

- Macro-dynamics scenario (1): we will present the baseline modelling approach for the tumour-OV interaction;
- Macro-dynamics scenario (2): based on the modelling approach in scenario (1), in addition to the random diffusion of viral-infected cancer cell density in the evolving tumour site, this cells motility has also a haptotactic migration feature against ECM gradients;
- Macro-dynamics scenario (3): with respect to the modelling approach in scenario (2), the new macroscopic model will include ECM- OV taxis behaviour assumption.

On other hand, at the micro-scale we extend the general framework to include a different proteolytic enzymatic system (Trucu et al., 2016; Peng et al., 2017), namely, urokinase plasminogen activator (uPA). Furthermore, we will explore the "macro-micro cross-talk" connection between the macro-scale dynamics and the uPA micro-dynamics that takes place on a cell-scale neighbourhood of the tumour boundary. Finally, we will investigate numerically the macro-scale scenarios for the parameter regimes that we considered for which cancer response to oncolytic viral therapy would be achieved. On the numerical side, we will further develop the novel numer-

ical multiscale framework first introduced in Trucu et al. (2013) to include our new macro-micro scenarios.

In Chapter 4 we will investigate the impact of syncytia presence on the overall oncolytic therapy. Although syncytia formation within tumour site is not fully understood, our new approach opens the door for further mathematical researches to investigate this impact with more different scenarios and environments. However, in order to take a look at the influence of syncytium formation, we will extend our previous mathematical modelling framework of tumour-OV to include the cancer interactions with a fusogenic OV in the presence of syncytia dynamics. Following similar moving-boundary-multiscale technique (Trucu et al., 2013; Alzahrani et al., 2019), we will consider four distinct assumptions upon the macroscopic scale in terms of syncytium structures and motility within tumour site with respect to ECM components, namely:

- Macro-dynamics case (1): syncytia cancer structures do not diffuse, but they still play a central role on ECM remodelling and degradation;
- Macro-dynamics case (2): syncytia cells are able to diffuse, but they do not move haptotactically towards higher ECM gradients;
- Macro-dynamics case (3): in addition to syncytia cancer cells diffusion abilities, they also move haptotactically towards higher ECM gradients;
- Macro-dynamics case (4): syncytia diffusion coefficient is assumed to be a density dependent function.

These macro dynamics cases are considered at the tissue scale, while at the cellular scale we still have the same proteolytic enzymatic system, namely, uPA. Hence, we will present a numerical results of the possibility of tumour reduction in the presence

of OV and in terms of multiple syncytium factors such as: probability of syncytia formation, syncytia diffusion coefficient, or syncytia diffusion coefficient dependent.

In Chapter 5 we explore the local existence and uniqueness of the solutions for each of the coupled systems of PDEs involved at each scale. We will develop a fixed point approach to ensure the existence of a unique local solution in time for three mathematical models, namely, two macro-dynamics scenarios first introduced in Alzahrani et al. (2019) (section 3.3), namely, scenario (1) and scenario (3) and the micro-dynamics model introduced in section 3.4. In this chapter the proof of the existence of solutions will be investigated at two-scales (macroscopic and microscopic) to support our numerical findings in Chapter 3 and Chapter 4. Specifically, we use the classical semigroup methodology (Henry, 1981) applied on an appropriate Banach space with all the necessary properties that would ultimately enable us to apply the Banach contraction theorem to prove the uniqueness of the local solution for the macro-dynamics scenario (1) in section 3.3. Then, in the same manner, we will follow a sequence of steps to show that there exists a unique locally-in-time solution for the macro-dynamics scenario (3) section 3.3 and in addition to the microscopic model (section 3.4).

1.2 Biological Background

Cancer is considered as one of the leading causes of death over this century and, in particular, the biggest number of cancer deaths is due to metastases. The quest for a deep understanding of this complex multiscale disease received broad attention within the scientific community, motivating many researches to focus on exploring the dynamic behaviour of cancer, with the ultimate hope of establishing the innovative treatment strategies. One of the most important scientific efforts that focuses on

cancer treatment is the treatment by using a special type of virus, namely, oncolytic virus (OV). Indeed, viral therapy presents promising perspectives towards controlling the tumour growth and eventual cancer elimination. Therefore, this research direction has motivated the purpose of this thesis, which focus on a mathematical and computational investigation of the dynamic interactions between malignant tumour cells and an oncolytic virus as well as the impact that these have on the process of cancer growth and spread.

In the following, we will present an overview of the cancer invasion process within the human body alongside a biological background on OV and its related components such as viral-selective-replication mechanism. In this context, we will briefly revisit a number of key mathematical modelling developments for cancer invasion (based on both temporal and spatio-temporal approaches), with and without the presence of tumour-virus interactions.virus

1.2.1 Cancer invasion of tissue

Cancer is a fatal disease that involves several spatial and temporal scales, ranging from genes to cells to tissues. The cancer cells invasion of tissue is considered as one of the so-called *"hallmarks of cancer "*(Hanahan and Weinberg, 2000, 2011), as this not only leads to a degradation of the surrounding tissue, affecting their naturally organised structure (developed through controlled and organised growth of normal cells and naturally homeostatic molecular signaling pathways), but through abnormal cell proliferation and complex active cell migration mechanisms alongside the associated molecular processes this paves the way to metastatic spread of the malignant tumour in the entire body, ultimately resulting in the death of the individual.

Cancer invasion process is a key stage within the overall cancer growth and spread in the human body. Soon after significant local cancer growth and invasion of tissue, the angiogenesis process is triggered through the secretion and local molecular transport of vascular endothelial growth factors, which eventually lead to the establishment of an auxiliary network of blood vessels which extend the main normal vasculature until this eventually gets connected to the tumour (Pierce et al., 1978). Then, once the auxiliary blood vessels get attached and eventually protrude the tumour, some of the cancer cells will exercise an intravasation, penetration through the walls of the blood vessels and getting this way by the blood stream. Once in the blood stream these cancer cells are carried away by the blood, eventually getting to extravasate the blood vessels at remote locations within the body where these give rise to secondary tumours, called metastases, from where the process described so far is continued and repeated (Weinberg, 2006). At that stage the cancer is virtually out of control and if the metastases are not all detected early enough, then this usually result in the death of the individual. For that reason, it is important that cancer is detected early enough, eventually at the stage when the tumour is still avascular and only pre-metastatic tumour invasion will have occurred. For that reason, this thesis will consider that the cancer invasion process is in this particular local invasive stage (before angiogenesis), at which an engineered oncolytic virus is brought into the picture.

Taking advantage both on its heterotypic and heterogeneous nature, the tumour explore favourably the tumour microenvironment during the local cancer invasion to advance within the surrounding tissue (Russo et al., 2016). Indeed, right from its early stages of development, not only that primary tumour cells undergo mutations to secondary more aggressively invasive tumour cells, but besides the cancer cells themselves the tumour microenvironment contains lots of other cells types such as

immune cells, immune-inflammatory cells, macrophages, cancer associated fibroblasts, and remarkable is that altered molecular signalling mechanisms enable the cancer cells to positively instigate these other types of cells to undertake actions that get to favour the tumour progression (Hanahan and Weinberg, 2000, 2011). Furthermore, right from the early stages of its development, a well distinguished inner structure of the tumour emerges, namely, the tumour will present a necrotic core, a middle quiescent region, and an outer proliferating rim (which is the most viable part of the tumour that is ideally placed in direct contact with nutrients and oxygen). In this context, alongside random movement of the tumour cells and altering their cell-adhesion properties, the cancer cells from the outer proliferating rim of the tumour (alongside other types of cells present in that region) secrete various important proteolytic enzymes, such as several classes of matrix metalloproteinases (MMPs) as well as the urokinase plasminogen-activator system (uPA) (Degryse, 2011; Sobel et al., 1952). These proteolytic enzymes play a key role in local cancer invasion as once secreted and activated these come in contact with and degrade the extracellular matrix (ECM), calving away a significant part of its components (such as vitronectin (VN), fibronectin, and collagens), this way creating room for invasion and ultimately facilitating a change in tumour spatial morphology, ultimately leading to further tumour progression (Weinberg, 2006).

1.2.2 Molecular functionalities of two important proteolytic enzymes: MMPs and urokinase plasminogen activator components

Biological evidence shows that cancer invasion and migration is based on multiple factors which exercise their spatio-temporal actions and have impact on key cell- and tissue- scales associated processes (Hanahan and Weinberg, 2011), (Qian and

Pollard, 2010), (Kalluri and Zeisberg, 2006). One of these important factors is the proteolytic enzymes produced by cancer cells which degrade extracellular matrix (ECM) and that in turn leads to cancer cells migration to the surrounding tissue. Of notable importance among these proteolytic enzymes for cell-migration are the classes of matrix metalloproinanses (MMPs) and urokinase plasminogen activator (uPA), and for that reason in the following, we will revisit several biological characteristics for some of the MMPs and the uPA system. In particular, uPA's system contains the following components, urokinase plasminogen activator (uPA), urokinase receptor (uPAR), plasminogen activator inhibitor type1 (PAI-1), and plasmin.

MMPs The matrix metalloproteinases are a family of zinc-dependent enzymes with common or distinct properties working together to degrade all components of the ECM. The MMPs are secreted and activated both by the cancer cells (Endres et al., 2016) as well as other by cells from the tumour micro-environment such as the immuno-inflammatory cells or cancer-associated fibroblasts (Hassona et al., 2014). Once secreted, the MMPs could remain either as membrane-bound such as MT-MMP, or as freely diffusing through the ECM. Once MMPs reach ECM, they have the ability to destroy most important structural component for tissue connectivity namely, collagen. However, there are several MMPs types having different impact in ECM degradation, for instance MMP1, MMP2 and MMP14. Indeed, in some clinical trials, inhibitors of MMPs could be used to be anti-cancer medicine (Stamenkovic, 2000).

uPA Urokinase plasminogen activator is basically a serine protease induced via human or some animal cells. Indeed, the first description of the uPA system was given by MacFarlane and Pilling in 1947 (Degryse, 2011; Macfarlane and Pilling, 1947) even though they did not named it as *"uPA's system"*. However, in 1952 this

enzyme was named as uPA (Degryse, 2011; Sobel et al., 1952). The importance of uPA's system originally came from their presence in the extracellular matrix of various types of human tissues. As ECM degradation allows cancer cells to migrate then invade other tissues, uPA is considered as one of most proteolytic enzymes in which have more ability to destroy most ECM proteins. Precisely, the main role of (uPA) is focused on turning the plasminogen into plasmin where this transformation activates MMPs which promotes even more ECM degradation. Furthermore, (uPA) enhances the binding process of the receptor (uPAR).

uPAR Urokinase plasminogen activator receptor is mainly known as a binding multi-sites receptor for urokinase and vitronectin on the cell surface (Ploug, 2003). The multi-sites property of uPAR allows for having two separate sites for each components namely, uPA and vitronectin. Besides, in each distinct location on the cell surface, uPAR creates a perfect binding environment such as signalling and proteolysis regulatory. In fact, uPAR plays a key role in terms of tissue reorganization in a healthy body, therefore the malignant cells just hijack this role and takes advantage of it in order to invade the surrounding tissue. Sometimes, uPAR with other receptors could change the tumour from a dormancy to a metastasis scenario.

PAI-1 Urokinase plasminogen activator Inhibitor-1 is a serine protease considered as a principal inhibitor of uPA (Andreasen et al., 1990). In a healthy human tissue, the cells produce multiple types of inhibitors in order to protect themselves from proteolysis induced via uPA. However, one of most powerful uPA's inhibitor is PAI-1 where it plays a key role in terms of preventing the plasminogen activation. Again, as known cancer cells hijack the uPA's natural system role to exploit it in their benefit to migrate and invade the surrounding tissues. However, PAI-1 could prevent this exploitation case via their process of inhibiting uPA for which leading to decrease

the ability of uPA to degrade ECM components.

Effect of uPA on VN (in human) Vitronectin (VN) is a protein existed within ECM increasing cell adhesion and spread, in additional to regulating the proteolytic enzymes by plasminogen activation. At its N-terminal, VN interacts with several ligands such as PAI-1 and uPAR to promote cell migration, and invasion. Furthermore, VN-uPAR interaction enhances the clearance of apoptotic cells. Besides, the inhibitor PAI-1 could prevent VN to play its pro-active role in the conversion of plasminogen to plasmin. However, when VN is centralized on a neighbouring surface of cellular site, VN has the chance to neutralize PAI-1 by making an imbalance in benefit of the plasminogen activator and the active plasmin (Ploug, 2003).

Plasmin Plasmin is a serine protease (enzyme) present in ECM components induced through a conversion of a zymogen called plasminogen (Andreasen et al., 1997). Indeed, there are several enzymes that have the ability of converting the plasminogen into plasmin such as tissue plasminogen activator (tPA), and uPA. Besides, as mentioned above, uPAR plays a key role in this conversion and, in particular, within the activation process by uPA. However, the importance of plasmin in uPA's system comes from its diffusive spread within ECM components for which playing an important role in digesting ECM proteins. Furthermore, it enhances the MMPs Proteolysis process in order to increase the chance of ECM degradation.

1.2.3 Oncolytic virus (OV)

The aim of Oncolytic virus (OV) is to kill cancer cells by giving minimum effect to normal body health tissues. These virus have the ability of replication within tumour cells which drives to cancer cells lysis (Kim et al., 2014) (this tumour-OV interactions being illustrated in Figure 1.1). At the early years of the last century,

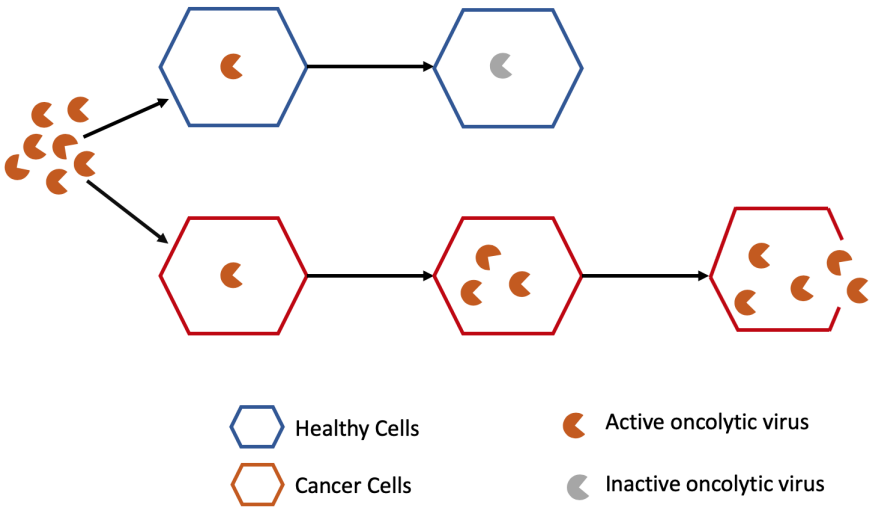

Figure 1.1: Schematic of tumour-OV interactions.

researchers were looking for natural oncolytic virus due to technological limitations of virus customization. Later on, development of technology provides the ability of construction new virus or modifying current ones. The Chinese state food and drug administration were the first organization that approved the world's first (OV) for clinical purposes in China, despite that the understanding of its spreading properties within the tumour remains a challenge and brings questions regarding its anti-tumour efficiency. Shanghai Sunway found the initial modified adenovirus H101, which then contributed to obtaining the most important oncolytic adenovirus ONYX-015 (Kim et al., 2014; Agarwal and Bhadauria, 2011).

The adenovirus ONYX-015 is a selectively "genetic-engineering" modified virus with two essential properties: it has the ability of replication and it enables to kill cells in the absence of p53 (Balachandran et al., 2001; Kim et al., 2014). The protein p53 is known as the human tumour suppressor, "the guardian of genome safety",

which has attributions in cells proliferation control and apoptosis. ONYX-015 can survive and replicate when it infects cells that have low quantity of p53, resulting in tumour cells death, otherwise, transcription factor of p53 will inhibit virus infection (Agarwal and Bhadauria, 2011). (Larson et al., 2015) has studied the modified version of ONYX-015 and its relation with E1b-55k gene. E1b-55k gene plays a central role in preventing the tumour suppressing function of p53. Therefore, ONYX-015 has been modified by deleting E1b-55k gene in clinical trials, so that p53 will act naturally on equivalency of cells proliferation with cells apoptosis. For 46% of patients that were injected with ONYX-015 in liver, the clinical trial shows that the tumour cluster increased after 21 days of injection. However, later on, the tumour cluster collapse started from the fourth month of the injection initial period to the tenth month, leading finally to a successful therapy.

The imbalance between normal cells proliferation and apoptosis (i.e., "programmed cells death") is a key factor contributing to the tumour initial growth. This imbalance is facilitated by many factors, such as antiviral proteins and virus-induced-carcinogenesis (i.e., "oncogenesis"). First, Antiviral proteins has important role in virus destruction. One of the antiviral proteins is zinc-finger antiviral protein (ZAP). This protein is produced by infected-cells to prevent viral replication and propagation of certain types of virus such as: leukemia virus, sindbis virus and alphavirus M1. Alphavirus M1 is a Getah-virus type extracted naturally from mosquitoes. In fact, Getah-virus type are not related to any human diseases or even mice, but they have the ability of transmission for some animals such as horses, therefore, alphavirus M1 was chosen as oncolytic therapy. The experimental study shows that, for 66 different cancer and normal cells lines, there was very low destruction of normal cells (even though using 100 virus particles per cell), while there was (30%)

destruction in 29 cancer cells lines (with only 10 virus particles per cell). Finally, it was noted in this experiment, the zink-finger antiviral proteins ZAP controled the temporal therapeutic dynamics, having the ability of speeding up or slowing down the therapeutic period (Lina et al., 2014).

Second, virus-induced-carcinogenesis is almost causing (15 %) of human cancers via accumulating the genomic transformations which in turn leading to DNA-deformation. DNA deactivation begins from a chemical transition of DNA base which making a disruption in DNA strands. This disruption originally come from p53 gene inhibition and inflammation resulting of virus. There are many types of virus-induced-carcinogenesis such as SV40, KSHV, EBV and HTLV-I. As an example, Simian virus 40 (SV40) "oncogene" has been used since 1970s for forming tumour in mice. SV40 plays a key role in p53 deactivation in which leading to stability of p53 production during time. In this case, p53 loses its ability of tumour suppressing function i.e. SV40 interaction with p53 implies that cells apoptosis in uncontrolled mechanisms. Moreover, SV40 has the ability for deactivating other proteins such as p107 and p130 in which driving to massive production of cells proliferation (Chen et al., 2014; Hudson and Colvin, 2016).

The tumour ECM plays a vital role in preventing the virus spreading, restricting the viral duplication and lowering the effectiveness of cytolytic. The other components that block the virus spread in neural ECM are hyaluronic acid (HA) and proteoglycans. These structural elements are also famous for delaying large therapeutic molecules. The utilization of ECM degradation enzymes can raise the effectiveness of OV treatments by allowing the virus to flow freely among uninfected tumour cells. The remodeling of ECM is also a main component of brain tumour

angiogenesis (Kim et al., 2014).

1.2.4 Virus tumour interactions

Heterogeneity Well documented biological evidence (Hanahan and Weinberg, 2000, 2011; Weinberg, 2006) highlights the presence of cancer heterogeneity manifested through the emergence and coexistence of several subpopulations of cancer cells who are sharing specific characteristics within a single neoplasm (Karev et al., 2006; Russo et al., 2016). Regardless of the complexity of cancer, there are a couple of mechanisms which enable viewing the cancer as a robust system and that manifest themselves through cellular redundancy and controlling the responses of systems at the cell level. Indeed, the importance of cancer robustness comes from its ability of enabling the system to maintain functionality and survival. In brief, two important emerging aspects here are: on one hand we have the tumour heterogeneity manifested through the non-uniform abilities of cells to be infected by the virus, moreover; and on the other hand the heterogeneity of virus implies leads to variability of cancer cells infection. The importance of heterogeneous tumour context comes from its ability to present various tumour phenomenons such as cancer cells recurrence and temporary dormancy, unlike that, homogeneous missed few tumour phenomenons such as dealing with tumour size as constant during time (Karev et al., 2006). Thus, heterogeneous nature of the cancer cell population and oncolytic virus plays a central role on one hand achieving cancer invasion and on the other hand ensuring the continuity of viral therapy.

Immunity mechanism In general, the immune system cells live in several body tissues such as lymphatic, thymus and bone marrow, while only (2%) of them moves

through human blood. T-cell is a particular type of immune system that produced by thymus in which has the ability to recognise any foreign substances such as virus and bacteria (anti-genes) via its receptor, simply called TCR. T-cells have three distinct types: "helper, regulatory, and cytotoxic" T-cells. The helper T-cells support immune cells to be more active in responses to anti-genes, unlike the regulatory T-cells who turn off immune functions. The most important type is the cytotoxic T-cells due to its ability of killing cancer and infected viral cells. Every cell has complex mechanisms for expressing parts of its internal proteins on its surface. Moreover, antigen presenting cells (AP-cells) helps the receptor TCR to connect and display the anti-genes by major histocompatibility complexes (MHC). MHC class I displays the anti-genes to cytotoxic T-cells, while class II displays the anti-genes to helper T-cells. Sometimes, the connection between TCR and MHC could be unstable, and in that case, for the binding purpose, the helper T-cells use their co-receptors CD4 while the cytotoxic T-cells use their co-receptors CD8 (Nowak and May, 2000).

Oncolytic virus interactions vs immune system Interferon (IFN) are small protein produced and released by virus-infected cells to improve their immunity. Moreover, INF are acting as signalling molecules for alerting surrounding cells. Oncolytic virus have distinct interactions with healthy tissues and tumour tissues. One experimental research has studied the influence of viral replication in different types of tissues: healthy, IFN responsive tumours, and IFN non-responsive tumours. On healthy tissues, infection of OV produces very low density of infected cells in which will be vanished by their IFN defence responses during time. On the IFN non-responsive tumours tissues, the released virus by the infected cells and the free virus particles diffuse quickly, leading to a faster diminution and eventual elimination of the cancer cell population. However, on the IFN responsive tumours tissues, the

therapeutic results depend on the balance between the virus production and the antiviral responses (Bœuf et al., 2013).

Oncolytic adenovirus release cytokines, which increase the immune reaction. Cytokines are a class of multi-types of proteins secreted by cells that plays an important role in cell signalling. Cytokines may work as inflammatory supporter such as IL-1β and IL-6, or as anti-inflammatory such as IL-4 and IL-10. One of the cytokines, Interleukin 12 (IL-12) acts as a T-cells motivating factor and promotes: T-cells growth, IFN production and NK-cells proliferation. Another cytokine, 4-1BBL, helps to distinguish T-cells and cytotoxic T-cells, in addition to its ability to stimulating T-cells and AP-cells. Finaly, in experimental studies on the interactions between cancer cells with OV therapy in mice, both IL-12 and 4-1BBl have been chosen carefully as anti-inflammatory cytokines in parallel with promoting the interferons levels and AP-cells activity for improving the immune responses (Zhang and An, 2007; Huang et al., 2009).

Viral-selective-replication mechanism Viral replication mechanism is a method for which having the ability for expanding during interactions with cancer cells and promoting immune responses (Rommelfanger et al., 2011). In general, the life cycle of viral-infection summarized into three basic procedures, namely: (1) viral-initial adhesion and invasion, leading to uncover virus genetic material; (2) production of virus proteins that on the one hand enable the interaction with the cancer cells, and on the other hand these are used for assembling new virus generation; and (3), releasing new virus for new life-cycle (i.e., starting a new process of adhesion and invasion) (Nowak and May, 2000). Over the above procedures, the interactions of virus and host cells could be understood after long-scale observation of immune responses during the viral therapy. This interaction release Interferons (i.e., "collec-

tion of signaling proteins"). The functional changes of the immune responses leads to oncolytic virus replications at the tumour location (Swift and Stojdl, 2016), i.e. in most tumour sites where the anti-viral cells will not contain the protein kinase R (which is a protein that is responsible for virus clearance) and that leads to viral replication increasing.

Induction of anti-tumour immunity Induction of anti-tumour immunity plays a key role in tumour destruction. Virus-infected cells release antigens (new-free-virus particles), cytokines, interferon and interleukin (IL-12), which in turn support the immune responses at the tumour location by activating the co-receptors (CD4 and CD8) (Kaufman et al., 2016). Although immune response plays a central role in tumour suppressing and control, tumour cluster size is another important factor. One of studies observes the efficacy of viral therapy for different tumour cluster sizes on mice. The mice were classified into different groups according to their tumour cluster size. After 7 days of the initiation of therapy, there was no change in all mice groups and their survival chance at that level remained unaltered. After 103 days, the mice group with the "smallest tumour cluster size" still survive. However, in mice with small tumour clusters, the viral therapy carried out in parallel to strong immune responses gives better and encouraging results (Rommelfanger et al., 2011).

Syncytium Formation As discussed in Section 1.2.3, Oncolytic viral therapy is a promising treatment for cancer due to the replication mechanism of viral particles within tumour site. Although this therapy technique show effective results in some clinical cases (Zeh et al., 2015), in addition to the physical barriers caused by ECM, questions regarding the viral systemic delivery and forced elimination induced via various immune responses remain as major challenges. However, there are multiple types of cancer - OV therapies in clinical trials with varying success rates

(Meerani and Yao, 2010; Kauman et al., 2015; Krabbe and Altomonte, 2018) that bring increasing evidence suggesting that the formation of syncytia might lead to better anti-tumour effects compared to the absence of fusogenic virus (Krabbe and Altomonte, 2018; Ebert et al., 2004). For that reason, in the following we focus on the syncytia formation mechanism.

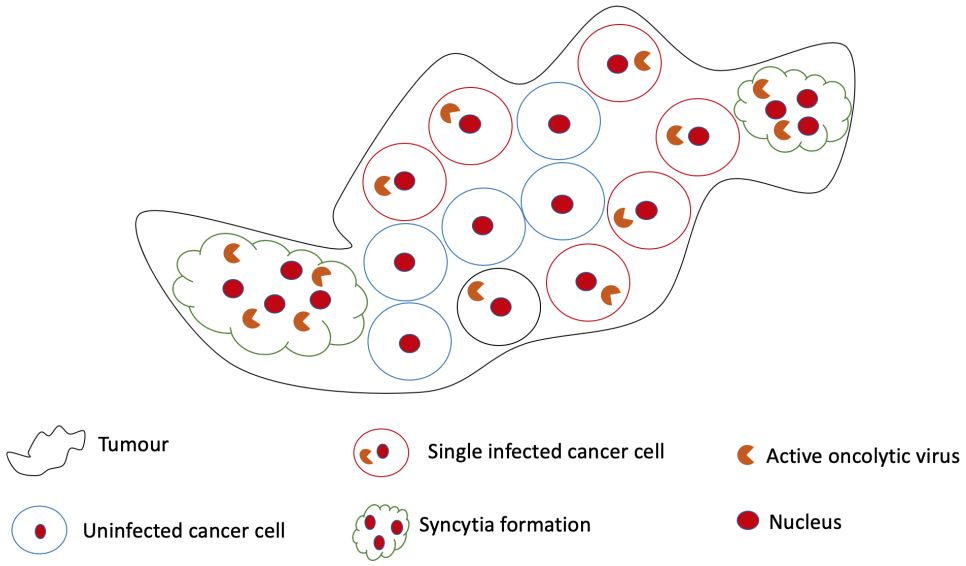

Figure 1.2: Schematic of tumour-OV interactions in the presence of syncytia.

The viral hemagglutinin protein H interacts with the cell membrane receptor CD46, leading to a transformation in the viral fusion F protein. This change in the viral fusion F protein allows for mixing up virus with cell membranes and this in turn leads to open up the cell's door for the viral particle. Then, in like manner we obtain the viral-infected cells population. Later, the viral-infected cell start to collect the new virus generation materials in the purpose of releasing new particles. Furthermore, the viral-infected cell will express parts of its internal proteins such as H and F proteins on its surface. Again, these surface "proteins" have the ability to making a connection with the receptor CD46 of the neighbouring viral-uninfected

cells for cell-to-cell fusion, i.e., viral-infected cells may be merged with neighbouring cells to form a Syncytia cells population (Biesecker et al., 2009). Notably, each Syncytium cell in the newly formed population contains multi-nucleus (for illustration, see Fig.1.2). Furthermore, it is notable that the average instantaneous velocity of Syncytia cells could be slightly larger than the velocity of the normal infected cells (Sylwester et al., 1993). Moreover, the presence of Syncytia cells could lead to increase the spread of the oncolytic virus through the uninfected tumour and, in addition to the natural deaths of Syncytia cells, this may lead to an increase in anti-tumour immune responses. Therefore, Syncytia cells enhance the therapeutic potential of the fussogenic virus for a faster destruction of cancer cells, offering the perspective of a better viral therapy (Ebert et al., 2004; Ayala-Breton et al., 2014; Krabbe and Altomonte, 2018). virus Finally, during the previous biological presentation, we have addressed some topics related to immune system mechanism, although the topic of immune system is not considered independently within this work. However, taking a look over the immunity mechanism provides to us a bigger picture on the interactions between cancer cells and oncolytic virus in terms of viral-selective-replication mechanism. Indeed, the immune system participates in the interaction process between cancer cells and OV either in a bad way through the elimination the oncolytic virus particles or standing for the benefit of viral therapy via enhancing the tumour destruction and promoting the viral replication mechanism. However, in this work we take into account the immune functions in indirect way, i.e., the lysis of viral-infected cancer cells is a result of the work of the immune system.

1.3 Modelling Background on Cancer Growth and Spread

Despite biological *in-vitro* and *in-vivo* advancements, cancer remains a tremendous disease whose understanding remains one of the greatest challenges of the scientific community. Cancer's genuinely multiscale nature, with its dynamics spanning on several interlinked spatio-temporal scales brings great difficulties to most lab investigations and involved imaging techniques, as, besides the costs involved, most of these approaches are usually one-scale only and can capture only a reduced representation of the actual tissue reality. Thus, the quest for identifying a suitable analysis framework remains one of the most difficult open problems, and to that end mathematical modelling and computational explorations became a natural avenue for exploring fresh ideas and advancing new biological and therapeutical hypotheses for controlling cancer. Indeed, the past thirty years or so have witnessed important mathematical modelling efforts and computational approaches aimed both at characterising various stages of cancer development as well as at exploring potential treatment avenues (Greenspan, 1976; Adam, 1986; Anderson et al., 2000; Chaplain and Stuart, 1993; Gatenby, 1995; Byrne and Chaplain, 1995b,a, 1996a,b; Gatenby and Gawlinski, 1996; Perumpanani et al., 1996, 1998; Byrne and Chaplain, 1998; Webb et al., 1999; Andasari et al., 2011; Anderson, 2005; Byrne et al., 2001; Chaplain and Lolas, 2005; Chaplain et al., 2006; Martins et al., 2007; Preziosi and Tosin, 2009; Stolarska et al., 2009; Alemani et al., 2012; Trucu et al., 2013; Deakin and Chaplain, 2013; Psiuk-Maksymowicz, 2013; Peng et al., 2017).

The mathematical models for cancer growth and spread proposed so far could be largely categorised as follows: discrete and individual base models, local ODEs and PDEs models, nonlocal PDEs models and finally hybrid (discrete macro-scales

models combined with ODEs and PDEs at the level of individual cells) and multi-scale models. In the following we present a brief overview of the developments of mathematical modelling of cancer invasion and growth that are relevant for research developed in this thesis.

1.3.1 ODEs modelling for cancer growth and spread

We start our short modelling synopsis on tumour growth modelling by considering early temporal approaches in the absence of any spacial considerations for tumour growth, namely ordinary differential equations based modelling. Although ODEs modelling faces lots of challenges in terms of representing a tumour growth scenario with a time dependance only, it accounts however for the rate of change in cells number per unit time. Clearly, the difference in cells number over time is based on two main factors, namely: cells production and cells decay. To illustrate this, let's consider the basic mathematical model of tumour growth described in Enderling and Chaplain (2013), namely:

$$\frac{dc}{dt} = \mu_0 c - \delta c, \tag{1.1}$$

where c is the total population size of cancer cells, while μ_0 and δ are the rates of proliferation and the removal of cancer cells over time, respectively. Obviously, the model (1.1) can be written in a simple exponential form (Malthusian growth modelling approach) as:

$$\frac{dc}{dt} = \mu_1 c, \tag{1.2}$$

where $(\mu_1 = \mu_0 - \delta)$ is the net growth rate of cancer cells population. Basically, the overall outcome of the tumour population size depends on three cases of the net growth rate μ_1, namely:

- when $\mu_1 = 0$, the population of cancer cells remains constant and that leads to tumour dormancy state.
- when $\mu_1 < 0$, the population of cancer cells is decreased over time.
- when $\mu_1 > 0$, the population of cancer cells is increased over time.

However, the tumour growth rate must depend on the total tumour population size c, hence μ_1 should actually be replaced by a function $f(c)$ instead of a constant μ_1, thus we have:

$$\frac{dc}{dt} = f(c)c. \tag{1.3}$$

Indeed, the function of the net growth rate of cancer cells population $f(c)$ has been represented in various forms, one such form is the logistic growth rate. The logistic growth or Verhulst model is generally used to describe the birth and death rates as a function of the total population and it can also be used to describe the tumour growth (Enderling and Chaplain, 2013; Sebastien et al., 2014) as

$$\frac{dc}{dt} = \mu_2 c(1 - \frac{c}{k_0}), \tag{1.4}$$

where μ_2 represents the growth rate and k_0 represents the carrying capacity. Precisely, the term $\mu_2 c$ indicates the growth rate, while the term $\mu_2 \frac{c^2}{k_0}$ corresponds to competitivity of cells to remain alive. Here, the function of the new growth of cancer cells is given by $f(c) = \mu_2(1 - \frac{c}{k_0})$. Thus, for a small tumour volumes i.e. $c < k_0$, the growth dynamics is exponential, while when c tends to k_0, the growth reaches to a growth saturation scenario. However, this model does show a reasonable prediction in vivo tumour growth (Sebastien et al., 2014). Furthermore, the function $f(c)$ could be represented by another growth law such as the power law and Gompertz modelling approach, but such models do not reflect the realistic picture of tumour growth

without taking the spatial dimension into a consideration. Therefore, most recent mathematical cancer researches take into account the cancer cells spatial transport (such as diffusive, advective or non-local transport) over time, and, in this regard, in the following section we will explore several existing spatio-temporal mathematical models that will be relevant for the research presented later in this thesis.

1.3.2 PDEs modelling for cancer growth and spread

Acknowledging the importance of space within the overall tumour evolution, we start this section by reflecting on one of the first important mathematical models for cancer invasion, namely the one proposed by developed by Gatenby and Gawlinski (1996), where a spatio-temporal perspective has been adopted. This spatial-temporal system considers the dynamics of cancer cells c in relative to healthy cells or extracellular matrix ECM u in the existence of Hydrogen ions (H+) a. Here, we show the dimensionless version of the coupled reaction diffusion system as follows, they first assumed that the population of cancer cells c is determined by the difference between the logistic growth at a rate μ_1 and their reaction diffusion with a motility rate D_c, while the extracellular matrix (normal cells) population is determined by the difference between the logistic growth of normal cells or ECM and their decay or degradation caused via the excess acid concentration at a rate δ_1. Furthermore, the excess Hydrogen ions a are produced and decayed at the same rate μ_2 with taking into account its chemical diffusion. Therefore, the mathematical model is shown by the following form:

$$\begin{cases} \frac{\partial c}{\partial t} = \nabla \cdot (D_c(1-u)\nabla c) + \mu_1 c(1-c), \\ \frac{\partial u}{\partial t} = -\delta_1 ua + u(1-u), \\ \frac{\partial a}{\partial t} = \Delta a + \mu_2(c-a). \end{cases} \tag{1.5}$$

It is obvious to see that the motility rate of cancer cells is controlled by the population of ECM where lowering ECM leads to higher cancer cells diffusion. Since, ECM population is determined by the difference between its growth and its degradation caused via H ions, therefore ultimately the secretion of H ions plays a key role in the cancer cells population. However, the main result of this study (where it is a harmonious with clinical observations) is centred on hypocellular gap between the normal or ECM and cancer cells. The expanding or shrinking of this gap depends on the value of the critical parameter δ_1, where in the case of $\delta_1 > 1$, the cancer invasion occurs, otherwise when $\delta_1 < 1$, this gap is expanding and that means that the tumour edge will be away from the surrounding ECM or heathy tissue.

Looking beyond the random motility expressed simply through diffusion, Anderson et al. (2000) developed one of the first modelling approaches for cancer invasion and growth in one and two spatial dimensions that take into account the directional movement against ECM gradients, referred to as "haptotaxis". The deterministic mathematical model is used to represent the dynamical interactions of cancer invasion c, extracellular matrix or host tissue u and a general form of ECM degrading enzymes a. In a comparison with the early model of cancer growth (Gatenby and Gawlinski, 1996), here they look for the overall cancer invasion, therefore there is no cancer logistic growth assumption. However, the cancer invasion density c is given by the spatial diffusion at a rate D_c in parallel with a haptotactic directional motility with a haptotactic rate η_c. Furthermore, the density of extracellular matrix u is only assumed to be decayed due to the enzyme degradation at a rate δ_1, while the degradation enzyme density a is given by the difference between a production caused via cancer invasion at a rate μ_1 and a natural decay at a rate δ_2 with taking into consideration their spatial diffusion at a rate D_a. Thus, the mathematical

model is given by the following formula:

$$\begin{cases} \frac{\partial c}{\partial t} = D_c \Delta c - \eta_c \nabla \cdot (c \nabla u), \\ \frac{\partial u}{\partial t} = -\delta_1 u a, \\ \frac{\partial a}{\partial t} = D_a \Delta a + \mu_1 c - \delta_2 a. \end{cases} \tag{1.6}$$

Despite the deterministic model of this study does not include a cancer proliferation term, it opens the door for the coming researches to investigate the ECM gradients, for instance the studies Chaplain and Lolas (2005, 2006); Peng et al. (2017) take into consideration the ECM degradation by the uPA proteolytic enzyme system. Moreover, the model in Anderson et al. (2000) assumed that the directional motility of cancer invasion is a haptotaxis towards gradients of a heterogeneous ECM. One of the main outcomes of this study consists in emphasizing the importance of ECM heterogeneity and the associated directional movement, and the takehome message is that that these should be assumed in any cancer model due to its similarity to the real ECM.

In a later study, Chaplain and Lolas (2006) investigate multiple scenarios of cancer invasion in terms of cancer proliferation, random motility and/or cancer directional motility through ECM gradients, in the presence of the proteolytic enzymes system enabled by the uPA (i.e., the urokinase plasminogen activator system). Here the cancer cells population is denoted by $c(x,t)$, ECM density is denoted by $u(x,t)$, and the density of uPA denoted by $a(x,t)$. The mathematical model assumes that the cell population exercises both random motility (expressed through diffusion) and directional movement of cancer invasion through ECM (representhed there through haptotaxis). Here, in addition to the previous model introduced in (Anderson et al., 2000), this model is assumed to include a cancer logistic growth at a rate μ_1. Furthermore, ECM density is not only represented in a decay case as proposed by 1.6,

but it grows logistically at a rate μ_2, therefore the density of ECM is represented by this balance between the logistical growth and the decay caused via proteolytic enzyme uPA. Thus, the resulting mathematical system of PDEs is:

$$\begin{cases} \frac{\partial c}{\partial t} = D_c \Delta c - \eta_c \nabla \cdot (c \nabla u) + \mu_1 c(1 - c - u), \\ \frac{\partial u}{\partial t} = \mu_2 u(1 - c - v) - \delta_1 u a, \\ \frac{\partial a}{\partial t} = D_a \Delta a + \mu_3 c - \delta_2 a. \end{cases} \tag{1.7}$$

The numerical results for this model is represented in one dimensional space. The initial outcome involves that the cancer cells moves to a region where ECM has higher density. This results leads to examine the effects of haptotaxis rate η_c over the overall outcome, therefore they have increased η_c ten times and then later on further more. Numerically higher haptotaxis rate shows that the cancer cells migrate much faster whenever η_c is increased. This migration does not necessary mean that the cancer invasion is expanding, but it could migrate backwards and forwards in respect to ECM gradients. Equally important is testing a different pattern of the proteolysis production at the tumour site and as well as its invading edge. To study this further case, Chaplain and Lolas (2006) assumed uPA's production is given by a logistic growth rule. Thereupon, the previous model 1.7 is rewritten in the following form:

$$\begin{cases} \frac{\partial c}{\partial t} = D_c \Delta c - \eta_c \nabla \cdot (c \nabla u) + \mu_1 c(1 - c - u), \\ \frac{\partial u}{\partial t} = \mu_2 u(1 - c - v) - \delta_1 u a, \\ \frac{\partial a}{\partial t} = D_a \Delta a + \mu_3 c(1 - c) - \delta_2 a. \end{cases} \tag{1.8}$$

In order to examine the new assumption numerically, the authors used the same parameter baseline values as for the previous model 1.7 except of increasing the rate of uPA's production μ_3 and decreasing the natural decay rate of uPA δ_2. Under those circumstances, the cancer cells start to accumulate at the tumour edge, then

as a result, ECM is degraded at the same place as well. Thus, the cancer cells are now able to migrate haptotactically to another region. However, there is an evidence of that the over-expression of uPA does not only affect cancer cells migration on the tumour edge, but it also affects both the proteolysis process and the proliferation of cancer cells. Hence, in order to adopt further assumptions to regulate cancer invasion, Chaplain and Lolas (2005) takes into consideration the interaction between cancer cells, $c(x,t)$, and ECM, $u(x,t)$ in the presence of the full uPA system, which alongside the urokinase plasminogen activator $a(x,t)$ also considers the plasminogen activator inhibitor-1 (PAI-1), whose density is denoted here by $p(x,t)$, and plasmin that has its density denoted by $m(x,t)$. In addition to the previously presented assumptions in the system 1.8, here it is assumed that the logistical proliferation (at a rate μ_1) of cancer cells is enhanced by the presence of uPA at a rate μ_2. Furthermore, cancer cells move in a chemotaxis directional cell movement in response to uPA and PAI-1 at rates η_a and η_p respectively, as well as they move in a haptotactic manner in response to ECM gradients at a rate η_u. Thus, the evolution of cancer cells density is represented by the following parabolic PDEs:

$$\frac{\partial c}{\partial t} = \underbrace{D_c \Delta c}_{\text{diffusion}} - \nabla \cdot [\ \underbrace{\eta_a c \nabla a}_{\text{uPA-chemo}} + \underbrace{\eta_p c \nabla p}_{\text{PAI-1-chemo}} + \underbrace{\eta_u c \nabla u}_{\text{ECM-hapo}}\ ] + \underbrace{\mu_1 c(1-c) + \mu_2 c a}_{\text{proliferation}}. \tag{1.9}$$

Besides this, the change per unit time in the extracellular matrix density is represented by the difference between the ECM remodelling and ECM degradation. The remodelling process is represented by the logistical growth at a rate μ_3 and the production caused by binding of uPA/PAI-1 at a rate μ_4. On other hand, the ECM degradation is caused due to binding with PAI-1 at a rate δ_1 and a decay caused via the impact of plasmin at a rate δ_2. Hence, the ECM dynamics can be represented

as

$$\frac{\partial u}{\partial t} = \underbrace{\mu_3 u(1-u)}_{\text{production}} + \underbrace{\mu_4 ap}_{\text{uPA/PAI-1}} - \underbrace{\delta_1 up}_{\text{PAI-1/ECM}} - \underbrace{\delta_2 um}_{\text{degradation}} . \tag{1.10}$$

While uPA is being produced by cancer cells at a rate μ_5, this diffuses on the tumour domain at a rate D_a, and at the same time it is removed from the system both due to inhibition induced via binding of PAI-1 at a rate δ_3 as well as by the binding exercised to the cells' surface uPA receptors (uPAR) at a rate δ_4. Therefore, the spatio-temporal dynamics of the uPA density is given by the following reaction-diffusion equation:

$$\frac{\partial a}{\partial t} = \underbrace{D_a \Delta a}_{\text{diffusion}} - \underbrace{\delta_3 pa}_{\text{uPA/PAI-1}} - \underbrace{\delta_4 ca}_{\text{uPA/uPAR}} + \underbrace{\mu_5 c}_{\text{production}} . \tag{1.11}$$

Moreover, the inhibitor PAI-1 density is produced through the activation of plasmin, hence (since the plasmin activation process is not captured explicitly by the model) here this us assumed to be indirectly brought into the system by the presence of plasmin at a rate μ_6. On the other hand, PAI-1 is removed from the system through binding to both uPA (at a rate δ_5) and the surrounding ECM (at a rate δ_6). In this context, as per unit time the inhibitor molecules are assumed to exercise a random motility (represented through diffusion), the dynamics of PAI-1 is given by the following PDE:

$$\frac{\partial p}{\partial t} = \underbrace{D_p \Delta p}_{\text{diffusion}} - \underbrace{\delta_5 pa}_{\text{uPA/PAI-1}} - \underbrace{\delta_6 pu}_{\text{PAI-1/ECM}} + \underbrace{\mu_6 m}_{\text{production}} , \tag{1.12}$$

where $D_p > 0$ is a constant diffusion coefficient.

Finally, the plasmin is assumed to be produced by the activation from plasminogen in the ECM both by uPA (bound to its cell-surface receptors uPAR) and by the binding of the inhibitor PAI-1 to ECM. Thus, as per unit time, in the presence of

these production factors and natural decay, plasmin molecular population exercise a random movement, its dynamics is therefore given by the following PDE:

$$\frac{\partial m}{\partial t} = \underbrace{D_m \Delta m}_{\text{diffusion}} + \underbrace{\mu_7 ca}_{\text{uPA/uPAR}} + \underbrace{\mu_8 pu}_{\text{PAI-1/ECM}} - \underbrace{\delta_7 m}_{\text{degradation}} . \tag{1.13}$$

where $D_m > 0$ is a constant diffusion coefficient, μ_7 represents the binding process between uPA and uPAR, μ_8 is the rate at which PAI-1 bind to ECM components (such as vitronectin), and $\delta_7 > 0$ is the constant natural decay rate.

1.4 Modelling Background on Tumour Virus Interaction

Despite the already very advanced mathematical models developed to describe the cancer growth and spread process, the modelling of tumour - oncolytic virus interaction still has a long way to go. This interaction has been approached over the past two decades mostly from temporal dynamics perspective (Wodarz et al., 2014; Laaroussi et al., 2014; Bajzer et al., 2008; Wodarz, 2016; Agarwal and Bhadauria, 2011; Wodarz and Komarova, 2009; Kim et al., 2015; Malinzi et al., 2015; Dingli et al., 2009; Nowak and May, 2000), with only few works in the area that considers also the spatial dynamics (Malinzi et al., 2015; Nowak and May, 2000; Wodarz et al., 2012; Wollmann et al., 2005; Camara et al., 2013; Malinzi et al., 2017). In the following we will present a synopsis of existing ODE and PDE based models of tumour - OV interaction that are relevant for the research carried out in this thesis

1.4.1 ODEs mathematical modelling on tumour virus interaction

Mathematical modelling helps experimental studies in virology to understand the complexity and nonlinearity of tumuor growth and the virus propagation dynamics which could be contributed in treatment scenarios. The initial and basic dynamical system to study the interactions between host cells and virus was proposed by Nowak and May (2000) and considers the coupled dynamics between an uninfected cancer cells population $c(t)$, an infected cancer cells population $i(t)$, and free virus density $v(t)$. This is expressed by three nonlinear ordinary differential equations;

$$\begin{cases} \frac{\mathrm{d}c}{\mathrm{d}t} = \mu_1 - \delta_1 c - \rho c v, \\ \frac{\mathrm{d}i}{\mathrm{d}t} = \rho c v - \delta_2 i, \\ \frac{\mathrm{d}v}{\mathrm{d}t} = \mu_2 i - \delta_3 v. \end{cases} \tag{1.14}$$

where μ_1 is the production rate of uninfected cells, δ_1 is the death rate of uninfected cells, ρ is the infection rate caused by virus, δ_2 is the death rate of infected cells, μ_2 is rate of the virus production caused by infected cells and δ_3 is the virus decay rate.

This basic model has been applied to study the dynamics of population behaviour during time for multi virus such as (HIV), Hepatitis B and C.

Based on the mass action assumption for only one infection cycle in vitro experiment, Wodarz et al. (2014) developed further model (1.14) and proposed the

following governing coupled dynamics

$$\begin{cases} \frac{\mathrm{d}c}{\mathrm{d}t} = \mu_1 c - \rho c v, \\ \frac{\mathrm{d}i}{\mathrm{d}t} = \rho c v - \delta_2 i, \\ \frac{\mathrm{d}v}{\mathrm{d}t} = -\delta_3 v - \rho c v \end{cases} \tag{1.15}$$

with taking into account that there is no any new virus production caused by infected cells. The term "ρcv" is usually ignored in the rate of change in virus density in most mathematical models of virus due to its very small contribution compared to the virus removal rate δ_3 caused by ECM.

Laaroussi et al. (2014) propose a model describing the interaction between oncolytic virus and tumour cells in the presence of logistic growth, namely

$$\begin{cases} \frac{\mathrm{d}c}{\mathrm{d}t} = \mu_1 c(1 - \frac{c+i}{k}) - \rho c v - \gamma c i, \\ \frac{\mathrm{d}i}{\mathrm{d}t} = \rho c v - \delta_2 i, \\ \frac{\mathrm{d}v}{\mathrm{d}t} = b\delta_2 i - \delta_3 v - \rho c v \end{cases} \tag{1.16}$$

Here, the rate of change in uninfected cancer cells $c(t)$ is given by a combination between logistic proliferation and removal from the system through viral infection and fusion between infected and uninfected cells. The constant $k > 0$ is the carrying capacity, ρ is the cell infection rate by virus, and γ is the rate of fusion of uninfected and infected cells. The rate of change in the infected cancer cells $i(t)$ is described by the difference between the infection rate and the cells death rate $\delta_2 i$. The rate of change of the free virus $v(t)$ is the difference between the virus ability of replication $b\delta_2 i$ and virus removal rate by any reason (ECM) $\delta_3 v$ or by infection ρcv. Analytically, reaching the free equilibrium points implies that tumour will be completely removed. The system free equilibrium stability is controlled by the basic

reproduction number $R_0 = \frac{b\rho k}{\rho K + \delta_3}$, when $R_0 < 1$, the equilibrium point is globally asymptotically stable and when $R_0 > 1$, the equilibrium point stability is monitored by a particular function performing the virus replication. While numerically, they show that when $R_0 > 1$; $c(t)$ decreases and both $i(t), v(t)$ increase, otherwise, when $R_0 < 1$, the viral therapy will be unsuccessful (Laaroussi et al., 2014). Moreover, the previous model was modified by Bajzer et al. (2008), by using a different form of tumour growth (Bertalanffy-Richards), namely

$$\frac{\mathrm{d}c}{\mathrm{d}t} = \mu_1 c(1 - \frac{c^\epsilon}{k^\epsilon}), \tag{1.17}$$

where the exponent ϵ is used for enabling the elasticity of growth curve, describing the shape of growth curve. In addition to that, Bajzer et al. (2008) model assume that the infected cells able to release new virus at rate α, namely

$$\begin{cases} \frac{\mathrm{d}c}{\mathrm{d}t} = \mu_1 c(1 - \frac{(c+i)^\epsilon}{k^\epsilon}) - \rho c v - \gamma c i, \\ \frac{\mathrm{d}i}{\mathrm{d}t} = \rho c v - \delta_2 i, \\ \frac{\mathrm{d}v}{\mathrm{d}t} = \alpha i - \delta_3 v - \rho c v \end{cases} \tag{1.18}$$

Wodarz (2016) considers again the model (1.18) and assumes that the virus is at steady state and obtains a governing dynamics as

$$\begin{cases} \frac{\mathrm{d}c}{\mathrm{d}t} = \mu_1 c(1 - \frac{c+i}{k}) - \delta_1 c - \rho c i, \\ \frac{\mathrm{d}i}{\mathrm{d}t} = \rho c i - \delta_2 i. \end{cases} \tag{1.19}$$

where $k > 0$ is the carrying capacity.

Agarwal and Bhadauria (2011) proposes a model that describes the interactions between cancer cells and oncolytic virus, also with the virus at stead-state. Their

model is expressed mathematically in the form of two nonlinear ordinary differential equations, namely:

$$\begin{cases} \frac{\mathrm{d}c}{\mathrm{d}t} = \mu_1 c(1 - \frac{c+i}{k}) - \frac{bci}{c+i+a}, \\ \frac{\mathrm{d}i}{\mathrm{d}t} = \mu_2 i(1 - \frac{c+i}{k}) + \frac{bci}{c+i+a} - \delta_2 i. \end{cases} \tag{1.20}$$

In this model, there are two new assumptions: first, the infected cancer cells proliferates at rate μ_2, and second, the term "$\frac{bi}{c+i+a}$" represents saturation effect, where a is the immune response measuring rate and b is the transmission and replication rate (i.e., improvement of immune system at one point will lead to prevent virus entry and replication). Simulation results show that tumour density will decrease when high virus replication is considered and $\mu_2 \leq \delta_2$.

Therefore, as formalised by (Wodarz and Komarova, 2009), in the absence of the immune responses, the basic ODEs modelling framework of tumour cells interaction with an oncolytic virus that is at steady-state is generally given by

$$\begin{cases} \frac{\mathrm{d}c}{\mathrm{d}t} = cF(c,i) - \rho i G(c,i), \\ \frac{\mathrm{d}i}{\mathrm{d}t} = \rho i G(c,i) - \delta_2 i. \end{cases} \tag{1.21}$$

The function $F(c,i) > 0$ denotes the growth law for the uninfected cancer cells, while $G(c,i) > 0$ represents the removal from the system of the uninfected cancer cells due to viral infection or fusion with the infected cells . Wodarz and Komarova (2009) have considered various scenarios for the two functions F and G, such as: "exponential" for $F(c,i) = 1$; "logistic" for $F(c,i) = 1 - \frac{c+i}{k}$; "2-D surface growth" for $F(c,i) = (\frac{\eta}{\eta+c+i})^{-\frac{1}{2}}$; and "3-D surface growth" for $F(c,i) = (\frac{\eta}{\eta+c+i})^{-\frac{1}{3}}$. It has been concluded that the use of exponential growth is not reasonable in tumour growth

due to its boundness of cells growth, while the logistic and surface growth model fit the data in a better way. Moreover, the logistic growth model has the lowest error based on previously experimental data, but "Why?". The logistic growth is the outcome of gradual saturation of the proliferation as this approaches the carrying capacity (i.e., there is a maximum number of cancer cells those could be alive in the system), while there is no upper limit for the number of cancer cells in surface growth models (i.e., the tumour growth is continuous over time until organism dies, which is not true in most human cancer cases).

Kim et al. (2015) models the rate of change at time variable for different cells population types and their interactions with four adenovirues, expressing and co-expressing of 4-1BBL adenovirues type, and expressing and co-expressing IL-12, namely as

$$\begin{cases} \frac{\mathrm{d}c}{\mathrm{d}t} = \mu_1 c - \rho\frac{cv}{N} - k(i)\frac{cT}{N}, \\ \frac{\mathrm{d}i}{\mathrm{d}t} = \rho\frac{cv}{N} - \delta_2 i - k(i)\frac{iT}{N}, \\ \frac{\mathrm{d}v}{\mathrm{d}t} = u(t) + \delta_3\delta_1 i - \delta_v v, \\ \frac{\mathrm{d}T}{\mathrm{d}t} = S_T(i) + pA - \delta_T T, \\ \frac{\mathrm{d}A}{\mathrm{d}t} = S_A(i) - \delta_A A. \end{cases} \tag{1.22}$$

The virus population v interacts with the overall cells population $N = c+i+T+A$, where c is uninfected cells, i is the infected cells, T is the T-cells and A is the AP-cells. The uninfected cells proliferate at rate μ_1, and initially they are being infected by v at rate ρ. The functions $k(i) = c_k i$ and $s_T(i) = c_T i$ represent the amount of cells production of 4-1BBL, T-cell death rate and T-cell supplying rate proportionally to i. The infected cells die after getting infected by virus at rate δ_2. The rate of change in virus size is given by the balance between injection at rate

$u(t)$, virus removal by infection at rate δ_3, and inactivated virus at rate δ_v. The T-cells activates by AP-cells at rate p and die at rate δ_T. Lastly, the AP-cells die at rate δ_A, and during the infection stage, the production of IL-12 leads to AP-cells motivation, which is explored through the term $S_A(i) = c_A i$.

The following mathematical model (Malinzi et al., 2015) represents the dynamical interactions between three cells types, namely: cytotoxic T-cells $T(t)$; uninfected cancer cells $c(t)$; and infected cancer cells by oncolytic virus $i(t)$. Its dynamics is mathematically given as

$$\begin{cases} \frac{\mathrm{d}T}{\mathrm{d}t} = s - \delta_1 T + \frac{fC_i}{g_1+i} - a_1 T i + (a_2 + a_3 p)c_z, \\ \frac{\mathrm{d}c}{\mathrm{d}t} = \mu_1 c(1 - k_1 c) - \frac{bic}{g_2+i}, \\ \frac{\mathrm{d}i}{\mathrm{d}t} = \mu_2 i(1 - k_2 i) + \frac{bic}{g_2+i} - a_1 ci + (a_2 + a_3(1-p))c_i, \end{cases} \tag{1.23}$$

where δ_1 is the death rate of cytotoxic T-cells, μ_1 and μ_2 are the growth rates of uninfected and infected cancer cells respectively, while k_1^{-1} and k_2^{-1} are the carrying capacities. The term $\frac{fC_i}{g_1+i}$ represents immune responses (i.e., cytotoxic T-cells proliferation), a_1 is the connection rate between c to i, a_2 is rate of infected cells lysis, $a_3 p$ is the probability of the complex cells death rate. Further, the function $\frac{bic}{g_2+i}$ describes the oncolytic virus replication into the cancer cells where b is the replication rate of OV. Finally, by receptor-ligand kinetics theory, the "complex cancer-cytotoxic T-cells" denoted by c_i is the output cell of the connection between T and i. This resulting complex cell lead to either infected cells death or cytotoxic T-cells suppression. Moreover, the destroyed infected cells release new virus particles, which motivate the anti-tumour cytotoxic T-cells responses. Hence, mathematically, this

was expressed as:

$$\frac{\mathrm{d}c_i}{\mathrm{d}t} = a_1 T i + (a_2 + a_3) c_i.$$

Furthermore, taking into account the differences on time scale of cancer and T-cells (slow-time-scale) and complex cells (fast-time-scale), it is assumed that $c_i = 0$, which results in the system

$$\begin{cases} \frac{\mathrm{d}T}{\mathrm{d}t} = s - \delta_1 T + \frac{\rho_1 T i}{g_1 + i} - l T i, \\ \frac{\mathrm{d}c}{\mathrm{d}t} = \mu_1 c(1 - k_1 c) - \frac{bic}{g_2 + i}, \\ \frac{\mathrm{d}i}{\mathrm{d}t} = \mu_1 i(1 - k_2 i) + \frac{bic}{g_2 + i} - m T i, \end{cases} \tag{1.24}$$

where $l = K a_3(1 - p)$, $\rho_1 = fK$, $m = K a_3 p$ and $K = \frac{a_1}{(a_2 + a_3)}$.

The following mathematical model shows the dynamical behaviour between cancer cells and oncolytic virus in the presence of syncytia cells s. Over the infection stage by the virus, the virus fragments bind with the cancer cells at rate ρ. This may lead to fusion scenario between infected and uninfected cells to form syncytia cells at rate γ. Both infected cells and syncytia cells release new virus at rate α. In this context, the total population of the cancer cells is given by $(c + i + s)$, where the infected cells population will be $(i + s)$. Denoting by λ the probability rate by which the new infected cell will remain in the infected cells density, the term $(1 - \lambda)$ is the probability by which the new infected cell will merge with uninfected cell to form syncytia cell. The infected and syncytia cells die at the same rate δ_1. The above biological assumptions were formalised mathematically by Dingli et al. (2009) through the system of ordinary differential equations as following:

$$\begin{cases} \frac{\mathrm{d}c}{\mathrm{d}t} = \mu_1 c(1 - \frac{(c+i+s)^\epsilon}{k^\epsilon}) - \rho cv - \gamma ci, \\ \frac{\mathrm{d}i}{\mathrm{d}t} = \rho cv - \delta_1 i + \lambda\gamma ci, \\ \frac{\mathrm{d}v}{\mathrm{d}t} = \alpha(i+s) - \delta_2 v - \rho cv, \\ \frac{\mathrm{d}s}{\mathrm{d}t} = (1-\lambda)\gamma ci - \delta_1 s. \end{cases} \tag{1.25}$$

Finally, alongside the usual uninfected cancer cells c, virus-infected cancer cells i, and the oncolytic virus v, the work proposed by Rommelfanger et al. (2011) brings into discussion also the immune response denoted by z, and so the resulting coupled is given by:

$$\begin{cases} \frac{\mathrm{d}c}{\mathrm{d}t} = \mu_1 c(1 - \frac{(c+i)^\epsilon}{k^\epsilon}) - \rho cv - \lambda_1 c(z+z_0), \\ \frac{\mathrm{d}i}{\mathrm{d}t} = \rho cv - \delta_1 i + \lambda_1 i(z+z_0), \\ \frac{\mathrm{d}v}{\mathrm{d}t} = \alpha i - \rho cv - \delta_2 v, \\ \frac{\mathrm{d}z}{\mathrm{d}t} = \lambda_2 i(z+z_0)(1 - \frac{z}{\zeta}) - \delta_3 z. \end{cases} \tag{1.26}$$

Here, the virus infect the cancer cells at rate ρ. The new generated infected cancer cells i will release new virus particles at rate α. However, taking into account that there is a part of the infected cells would not release any new virus particles, this leads to a virus removal at rate δ_2. The immune response rates are equal for both uninfected cancer cells and infected cancer cells and is taken to be $\lambda_1 > 0$. Moreover, the terms $\lambda_1 c(z+z_0)$ and $\lambda_1 i(z+z_0)$ are the uninfected and infected cancer cells growth rate with respect to cellular immune responses. The term $(1 - \frac{z}{\zeta})$ describes the limitation of immunity responses, while δ_3 is the elimination rate of immunity responses.

1.4.2 PDEs mathematical modelling on tumour virus interaction

An early spatio-temporal model describing the interaction between tumour cells was proposed by Nowak and May (2000). Here both uninfected cancer cells c, infected cancer cells i and virus v were assumed to be diffusing in the presence of logistic growth, and so, its spatio-temporal dynamics was mathematically given as:

$$\begin{cases} \frac{\partial c}{\partial t} = D_c \Delta c + \mu_1 c(1 - \frac{c+i}{k}) - \rho_1 cv, \\ \frac{\partial i}{\partial t} = D_i \Delta i - \delta_1 i + \rho_1 cv, \\ \frac{\partial v}{\partial t} = D_v \Delta v + \delta_1 bi - \delta_2 v. \end{cases} \tag{1.27}$$

where $D_c > 0$, $D_i > 0$, and $D_v > 0$ are the diffusion constants for uninfected cancer cells, infected cancer cells, and virus particle, respectively. μ_1 is the growth rate of cancer cells, k is the carry capacity, ρ_1 is the infection rate of cancer cells, δ_1 is death rate of infected cells, δ_2 is the death rate of free-virus and b is the virus replication number.

Building on Nowak and May (2000) model, Wodarz et al. (2012) adopts the assumptions of homogeneously free virus in steady-state, i.e., $\frac{\partial v}{\partial t} = 0$, and that no spatial transport is assumed for the virus, i.e., $\Delta v = 0$. These assumptions lead to $v = \frac{\delta_1 bi}{\delta_2}$, for the case of $\delta_2 > \delta_1$, and taking $\rho_2 = \frac{\rho_1 \delta_1 b}{\delta_2}$, the following system is obtained:

$$\begin{cases} \frac{\partial c}{\partial t} = D_c \Delta c + ac(1 - \frac{c+i}{k}) - \rho_2 ci, \\ \frac{\partial i}{\partial t} = D_i \Delta i - k_2 i + \rho_2 ci. \end{cases} \tag{1.28}$$

However, as challenges for this model, we note that the death rate of virus δ_2 must

be greater than the death rate of infected cells δ_1, but when choosing δ_2 very close to δ_1 will be unsatisfied. Second, by a comparison with Nowak's model, the decreasing-increasing term $\rho_1 cv$ of virus caused infection is missed. Later on, Rioja et al. (2016) expanded the modelling assumptions considered in Wodarz et al. (2012) while avoiding previous challenges (by having for instance v not proportional to the infected cells i.

In a more recent modelling development, building on experimental study, Wollmann et al. (2005) assume that the tumour is shaped as a circle in which has injected by the virus at the centre. Thus, the mathematical model is represented by partial differential equations to describe the interactions between tumour cells and virus, namely

$$\begin{cases} \frac{\partial c}{\partial t} = D_c \Delta c + \mu_1 c(1 - \frac{c+i}{k}) - \rho cv, \\ \frac{\partial i}{\partial t} = \rho cv - \delta_1 i, \\ \frac{\partial v}{\partial t} = D_v \Delta v - \rho cv + \delta_1 bi - \delta_2 v. \end{cases} \tag{1.29}$$

Virus particles diffuse through the tumour and lead to an infected cells density. On the other hand, in that particular experiment, the infected cells do not exercise a random motility, hence, they are not assumed to diffuse.

An important interaction between aggressively invasive Glioma cancer cells and the free oncolytic virus "ONYX-015" was explored by Camara et al. (2013). In that work the highly migratory Glioma cancer cells lead to highly diffusive behaviour for both uninfected and infected cancer cells as well as for the virus particles into many neural axis. Entry of virus into target cells is based on the Coxsackievirus and Adenovirus Receptor (CAR), which is also playing a central factor for tracing

the cancer cells by viral therapy. Moreover, the mitogen-activated protein kinase, known as "MEK" inhibitors helps (CAR) to increase its ability for tracing cancer cells. In this context, while the uninfected cancer cells are assumed to proliferate logistically at rate μ_1, these are considered to be infected by the virus at a rate ρ and in accordance to the saturation of virus infection "$\frac{rv}{1+\epsilon v}$", where $r > 0$ is the receptors average level. Infected cells could either die naturally at rate δ_2 or undergo lysis by the virus at rate a. Virus particles production at rate μ_2 of all possible ways are increasing in the absence of inhibitor. All these lead to the governing partial differential equations system:

$$\begin{cases} \frac{\partial c}{\partial t} = D_c \Delta c + \mu_1(1-n)c(1-\frac{c}{k}) - \delta_1 c - \frac{\rho r c v}{1+\epsilon v}, \\ \frac{\partial i}{\partial t} = D_i \Delta i + \frac{\rho r c v}{1+\epsilon v} - \delta_2 i - a i(1-n), \\ \frac{\partial v}{\partial t} = D_v \Delta v + \mu_2 i(1-n) - \delta_3 v. \end{cases} \tag{1.30}$$

Finally, using the same biological assumptions as those for the ODE based model(1.23), Malinzi et al. (2015) proposed also a spatio-temporal model to describe the interactions between cells with different types; cytotoxic T-cells $T(t,x)$, uninfected $c(t,x)$ and infected $i(t,x)$ cancer cells and the chemokines $m(t,x)$, namley

$$\begin{cases} \frac{\partial T}{\partial t} = D_t \frac{\partial^2 T}{\partial x^2} - \chi \frac{\partial}{\partial x}(T \frac{\partial h}{\partial x}) + H(x) - \delta_1 T + \frac{\rho_1 T i}{g_1 + i} - l T i, \\ \frac{\partial c}{\partial t} = D_c \frac{\partial^2 c}{\partial x^2} + \mu_1 c(1 - k_1 c) - \frac{bic}{g_2 + i}, \\ \frac{\partial i}{\partial t} = D_i \frac{\partial^2 i}{\partial x^2} + \mu_2 i(1 - k_2 i) + \frac{bic}{g_2 + i} - m T i, \\ \frac{\partial h}{\partial t} = D_h \frac{\partial^2 h}{\partial x^2} + \frac{\rho_2 T i}{g_1 + i} - \delta_2 h. \end{cases} \tag{1.31}$$

where $D_t > 0$ D_c, $D_i > 0$, and $D_h > 0$ are diffusion constants, $\chi > 0$ is chemotaxis constant, $H(\cdot)$ is a Haviside function which describes the immune cells prolifera-

tion and $\delta_2 > 0$ is the death rate of chemokines. The function $\frac{\rho_2 T i}{g_1 + i}$ is the resulting responses of chemokines replication in the tumour site. Numerical simulation of the problem shows that oncolytic viro-therapy minimises the tumour density by removing the infected cancer cells. Long run simulation show that $T(t, x)$ grows exponentially and $c(t, x)$ decreases during time.

Chapter 2

The General Multi-scale Moving Boundary Framework

In contrast to previous studies (Anderson et al., 2000; Byrne and Chaplain, 1996a; Chaplain, 1996; Chaplain and Lolas, 2005, 2006; Gerisch and Chaplain, 2008; Painter and Hillen, 2011; Preziosi and Tosin, 2009), the modelling framework (Trucu et al., 2013) develops a new perspective to study the tumor evolution by two scale spatio-temporal dynamics . The novel two-scale mathematical model describes the cancer cell invasion of tissue which dynamically connects on macroscopic and microscopic tumour activities. In brief, the macroscopic dynamics describing the evolution of the cancer cells and extracellular matrix ECM densities is coupled with microscopic dynamics that explore the spatio-temporal evolution of certain degrading enzymes. This coupling is done via top-down and bottom-up links. The top-down link provides the source for the micro-scale induced by the macro-dynamics. The bottom-up link provides the law for macro-scale tumour boundary relocation which is determined at from the micro-dynamics.

As the modelling in this thesis builds upon this multi-scale modelling framework,

we devote this chapter to explore the main features of the multi-scale modelling framework and the associated computational platform.

2.1 Overview of Multi-scale Modelling Hypothesis and Settings

In this section, we consider the novel multi-scale modelling framework presented first in (Trucu et al., 2013). For simplicity, we start with a short description of the overall methodology of this approach. This novel multi-scale framework aims to explore the dynamics of cancer invasion scenario with taking into consideration multiple interlinked actions at both tissue-scale (macro-scale) and cell-scale (micro-scale).

As cancer invasion is a complex multi-scale phenomenon, occurring on several temporal and spatial scales (Hanahan and Weinberg, 2011), the involvement of multiple dynamic components at critically different spatial scales requires an appropriate multiscale modelling platform, as it is not realistic to count two very different in size components on the same scale (for instance plasmin is a very small substance in a comparison with a cancer cell size). To address this important aspect, Trucu et al. (2013) has developed the multiscale-moving boundary modelling approach, that considers the integrated two-scales tumour dynamics connecting the macro- and through micro- scale dynamics through a double feedback link. In the following, we present the multi-scale technique and also we explain the linking methodology between the macroscopic and the microscopic systems, as introduced in Trucu et al. (2013).

We assume that the tumour evolution occurs on a domain $\Omega(t)$ that grows within a maximal tissue cube $Y \subset \mathbb{R}^n$ $(n = 2, 3)$ over a time interval $[0, T]$, as illustrated

in Fig. 2.1. Further, as the proteolytic activity of tumour that occurs within a cell-scale neighbourhood of the tumour interface is critical for the changes in the tumour boundary morphology and ultimately for the spatial progression of the tumour (Weinberg, 2006), a boundary tracking bundle of small micro-domains has been designed to capture the entire leading edge region where these important cell-scale boundary molecular processes take place.

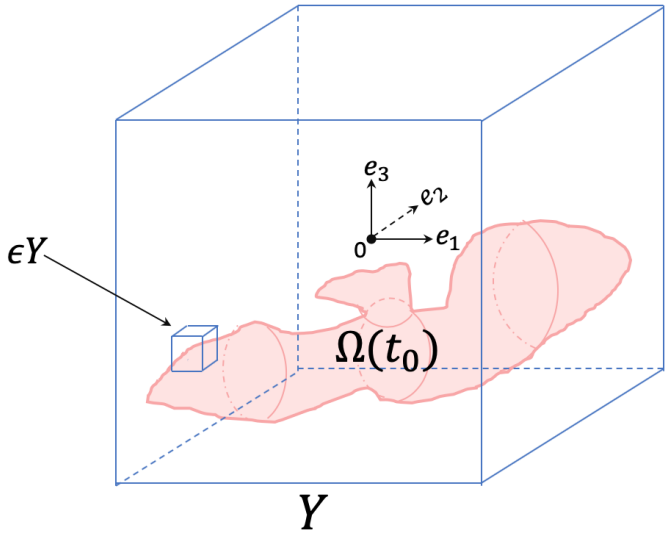

Figure 2.1: Schematic diagram to illustrate a tumour cluster $\Omega(t_0)$ centered at the origin within a three dimensional maximal reference region Y. The dashed lines indicates the Euclidean directions $\{e_1, e_2, e_3\}$. The micro-domain consists all ϵY-cubes located on the tumour boundary edge $\partial\Omega(t_0)$.

2.2 Construction of the covering bundle of boundary micro-domains in 2D

First, for a small scale $\epsilon > 0$ given as a negative power of 2, alongside the uniform decomposition of Y in small cubes of size ϵ, we consider also their associated *"half-way shifted"* copies in every direction, and collect all these in the family:

$$\mathcal{F}_\epsilon := \bigcup_{i,j,k\in\{-1,0,1\}} \left\{ \epsilon Y_{\frac{i}{2},\frac{j}{2},\frac{k}{2}} \middle| \epsilon Y \text{ is in the } \epsilon\text{-resolution of } Y \right\} \tag{2.1}$$

where, for any $(i,j,k) \in \{(i,j,k)|i,j,k \in \{-1,0,1\}\}$, the "half-way shifted" cubes in the direction $i\bar{e}_1 + j\bar{e}_2 + k\bar{e}_3$ are given by:

$$\epsilon Y_{\frac{i}{2},\frac{j}{2},\frac{k}{2}} = \epsilon Y + \frac{\epsilon(i\bar{e}_1 + j\bar{e}_2 + k\bar{e}_3)}{2}, \tag{2.2}$$

with $\{e_1, e_2, e_3\}$ representing the standard Euclidean basis of $\mathbb{R}^3$ and

$$\bar{e}_1 := e_1, \qquad \bar{e}_2 := e_2, \qquad \text{and,} \qquad \bar{e}_3 := \begin{cases} 0 & \text{for} \quad n = 2, \\ e_3 & \text{for} \quad n = 3. \end{cases} \tag{2.3}$$

Then, in a second step, we sub-select all those ϵ-cubes sub-family $\mathcal{F}^\epsilon_{\Omega(t)} \subset \mathcal{F}$ that intersect with the interface of the tumour edge $\partial\Omega(t)$ and has one face inside the tumour, namely:

$$\mathcal{F}^\epsilon_{\Omega(t)} := \{\epsilon Y \in \mathcal{F} | \epsilon Y \cap (Y \backslash \Omega(t)) \neq \emptyset \text{ and has exactly one face included in } int(\Omega(t))\}. \tag{2.4}$$

As illustrated in Fig. 2.2, for each ϵ-cube within the family $\mathcal{F}^\epsilon_{\Omega(t)}$ we can distinguish: the side inside $\Omega(t)$ denoted by $\Gamma^{int}_{\epsilon Y}$; $\Gamma^{j,\perp}_{\epsilon Y}, j = 1,2$ represent the perpendicular sides to the interior side; and lastly, the exterior side of the $\Gamma^{ext}_{\epsilon Y}$. Indeed, the exterior side

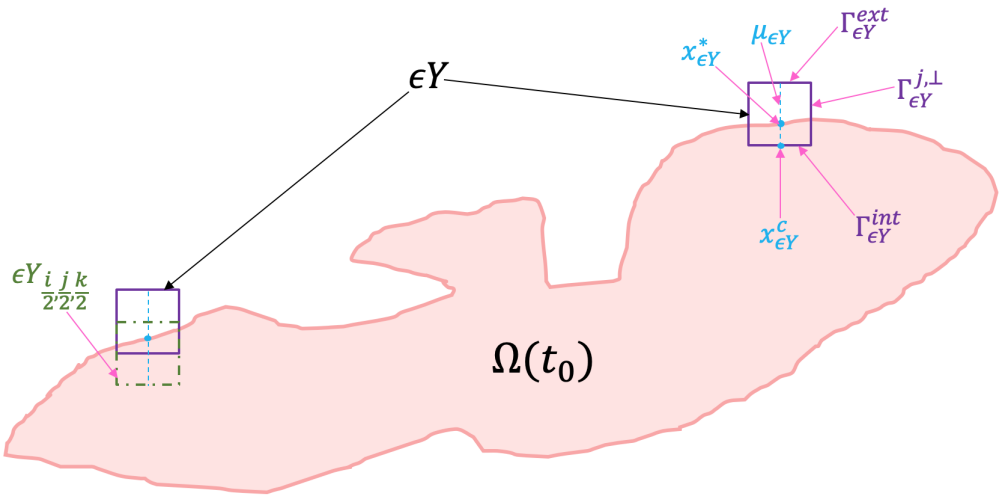

Figure 2.2: Schematic of the multiscale modelling approach.

$\Gamma^{ext}_{\epsilon Y}$ for each squared interface of the sub-family $\mathcal{F}^{\epsilon}_{\Omega(t)}$ would be either completely outside the tumour boundary $\partial\Omega(t)$ or partly intersected with $\partial\Omega(t)$. On the other hand, as $\Gamma^{int}_{\epsilon Y} \subset int(\Omega(t))$, let us denote by:

- $[\partial\Omega(t)]_{\epsilon Y}$ the connected component part $\Omega(t) \cap \epsilon Y$ that intersects $\Gamma^{j,\perp}_{\epsilon Y}$, $j = 1, 2$;
- $[\Omega(t)]_{\epsilon Y}$ the confined area lying between $\Gamma^{int}_{\epsilon Y}$ and the tumour boundary $[\partial\Omega(t)]_{\epsilon Y}$ (this turning out to be the only connected component of $\Omega(t) \cap \epsilon Y$ containing $\Gamma^{int}_{\epsilon Y}$)

(as illustrated in Fig. 2.2). With these notations, we sub-select the following boundary sub-family of $\epsilon-$cubes $\mathcal{P}_{\mathcal{F}^{\epsilon}_{\Omega(t)}}$ given by the following properties:

$$\mathcal{P}_{\mathcal{F}^{\epsilon}_{\Omega(t)}} := \{\epsilon Y \in \mathcal{F}^{\epsilon}_{\Omega(t)} |\ [\Omega(t)]_{\epsilon Y} \subset \epsilon Y \text{ and } [\partial\Omega(t)]_{\epsilon Y} \cap \Gamma^{ext}_{\epsilon Y} = \emptyset\}, \tag{2.5}$$

Finally, using compactness properties of the tumour interface alongside the properties of the dyadic ϵY cubes , we obtain the $\epsilon-$micro-scale as being given by

$$\epsilon_{_{\Omega(t)}} := \sup\left\{ \epsilon \,|\, \exists\, \mathcal{H}_\epsilon \subset \bigcup_{\epsilon\in\{2^{-p}|p\in\mathbb{N}\}} \mathcal{P}_{\mathcal{F}^\epsilon_{\Omega(t)}},\ \text{with } |\mathcal{H}_\epsilon| < \infty,\ \text{such that } \bigcup_{\epsilon Y\in\mathcal{H}_\epsilon} \epsilon Y \supset \partial\Omega(t) \right\}.$$

Finally, the desired $\epsilon-$scale covering bundle for $\partial\Omega(t)$ is given by $\mathcal{P}^*_\epsilon(t) := \mathcal{H}_{\epsilon_{\Omega(t)}}$. For simplicity, in the following, we will drop the index for $\epsilon_{_{\Omega(t)}}$, and we will refer to ϵ as the size of the micro-scale. Furthermore, the $\epsilon-$cubes $\epsilon Y \in \mathcal{P}^*_\epsilon(t)$, will simply be referred to as micro-domains. Finally, this bundle of covering overlapping micro-domains for the tumour interface $\partial\Omega(t)$ enable us to decompose the proteolytic cell-scale dynamics occurring on the cell-scale neighbouring region $\bigcup_{\epsilon Y\in\mathcal{P}^*_\epsilon(t)} \epsilon Y$ into a bundle of micro-dynamics occurring on individual micro-domains $\epsilon Y \in \mathcal{P}^*_\epsilon(t)$.

2.3 The macro-scale dynamics

Adopting the most simplistic perspective, at the macro-scale the invading tumour is a mixture of:

- a cell population, $c(x,t)$, mixed with
- an ECM density, $u(x,t)$,

for which, in the simplest possible case, the spatio-temporal dynamics (exercised on the progressing tumour region $\Omega(t)$) assumes that the rate of change per unit time is given as follows:

- for the cell population, this is at least a combined effect of:
  - cell proliferation;
  - diffusive transport; and

- taxis and haptotaxis (directed movements against ECM gradients);

- for the ECM density, this is the net balance between

  - degradation by the cancer cells (via various proteolytic enzymes); and

  - matrix remodelling.

Thus, the macro-dynamics can be summarised in general form of an operator equation

$$\mathcal{T}(c, u) = 0. \tag{2.6}$$

that is given by a 2D-reaction-diffusion-taxis differential operator of order 2

$$\mathcal{T} : \mathcal{C}^1([0,T]; H^2(\Omega(\cdot))) \times \mathcal{C}^1([0,T]; H^2(\Omega(\cdot))) \longmapsto \mathcal{C}([0,T]; \Omega(\cdot)) \times \mathcal{C}([0,T]; \Omega(\cdot))$$

and is accompanied by appropriate initial conditions as well as zero-flux boundary conditions. As a particular example for (2.6) we have the tissue scale dynamics adopted in Trucu et al. (2013), namely

$$\begin{cases} \frac{\partial c}{\partial t} = D_c \Delta c - \eta_c \nabla \cdot (c \nabla u) + f_{1,1}(c, u), \\ \frac{\partial u}{\partial t} = -\alpha_c c u + f_{2,1}(c, u). \end{cases}$$

where $f_{1,1}$ is a general function representing the cancer cells proliferation and $f_{2,1}$ represents the ECM remodelling.

2.4 The boundary micro-dynamics and the non-local top-down and bottom-up feedback links between macro- and micro- scales

Biological evidence shows that the tumour cells that arrive within the outer proliferation rim region, are able to secrete matrix degrading enzymes (MDEs), such as the MMPs or uPA (Weinberg, 2006), and once secreted, these enzymes exercise a cross-interface spatio-temporal molecular transport within the cell scale region along the tumour invasive edge where they degrade the matrix. Therefore, in the presence of macro-dynamics (2.6), for any $t_0 \in [0,T]$ and any micro-domain $\epsilon Y \in \mathcal{P}^*_\epsilon(t)$, at any spatio-temporal microscale node $(y,\tau) \in \epsilon Y \cap \times[0,\Delta t]$, a source of degrading enzymes gets created as a collective contribution of the tumour cells $c(x,\cdot)$ that arrive within a certain distance $\delta > 0$ from y, and hence this could be formulated mathematically in the following non-local operator terms as:

$$f^{\epsilon Y}_{MDEs}(y,\tau) = \begin{cases} \frac{\int_{\mathbf{B}(y,\delta)\cap\Omega(t_0)} c\,(x,t_0+\tau)\,dx}{\lambda(\mathbf{B}(y,\delta)\cap\Omega(t_0))}, & if \quad y \in \epsilon Y \cap \Omega(t_0) \\ 0, & if \quad y \in \epsilon Y \setminus (\Omega(t_0 + \{y \in Y |\ \parallel z \parallel_2 < \gamma\})) \end{cases} \tag{2.7}$$

where $\lambda(\cdot)$ is the usual Lebesgue measure, while the ball $\mathbf{B}(y,\delta) := \{\xi \in Y |\ \parallel y - \xi \parallel_\infty \leq \delta\}$ has the radius $\delta > 0$ of the size of the thickness of the outer proliferation rim (Weinberg, 2006), and γ is simply a small mollification radius, that enable us to have a smooth decay to 0 beyond the tumour interface $\partial\Omega(t_0)$.

Thus, denoting with $m(y,\tau)$ the amount of proteolytic enzyme distributed at a given micro-scale node $(y,\tau) \in \epsilon Y \cap \times[0,\Delta t]$, in the presence of source (2.7) a cross interface transport is exercised by $m(\cdot,\cdot)$, and under the simplest assumptions, as considered also in Trucu et al. (2013), this transport is simply given by a diffusion

process on ϵY, namely as

$$\frac{\partial m}{\partial \tau} = D_m \Delta m + f^{\epsilon Y}_{MDEs}(y, \tau) \tag{2.8}$$

where $D_m > 0$ is a molecular diffusion coefficients for the MDEs.

2.4.1 Discretisation of top-down link

On the other hand, at the micro-scale, the micro-dynamics is computed with taking into account the following assumptions and numerical approaches. For simplicity, we try to list all required discretization of the spatial micro-domain. As mentioned in section 2.1, the micro-domain consists of the union of ϵY-cubes from $\mathcal{P}^*_\epsilon(t)$ located on the tumour boundary $\partial\Omega(t)$. Now, let us first discretize the micro-domain ϵY with uniformly mesh size $2\Delta x = \epsilon$, where the tissue domain has already discretized with uniformly mesh size Δx (as illustrated in Fig. 2.3). Then based on the finite element approach, we could choose a random micro-domain $\epsilon Y \in \mathcal{P}^*_\epsilon(t)$ involving uniformly triangular elements on a micro-mesh. Hence, in a such spatial discretization, we definitely have common mesh points between the macro and micro domains located on the tumour boundary $\partial\Omega(t)$, specifically on the confined area $\epsilon Y \in \mathcal{P}_{\mathcal{F}_{\partial\Omega(t)}} \cap \Omega(t)$. Accordingly, we can define these contact mesh points by:

$$x_1, x_2, ..., x_{p_{\epsilon Y}} \in \epsilon Y \cap \Omega(t_0). \tag{2.9}$$

So, before presenting the micro-system computation procedures, we should first show the computation process of the integral source function 2.7 (Trucu et al., 2013). In order to do that, let us suppose the region M within $\mathbb{R}^2$ contains finite subdivided elements where these elements domains are denoted by the entire generic element

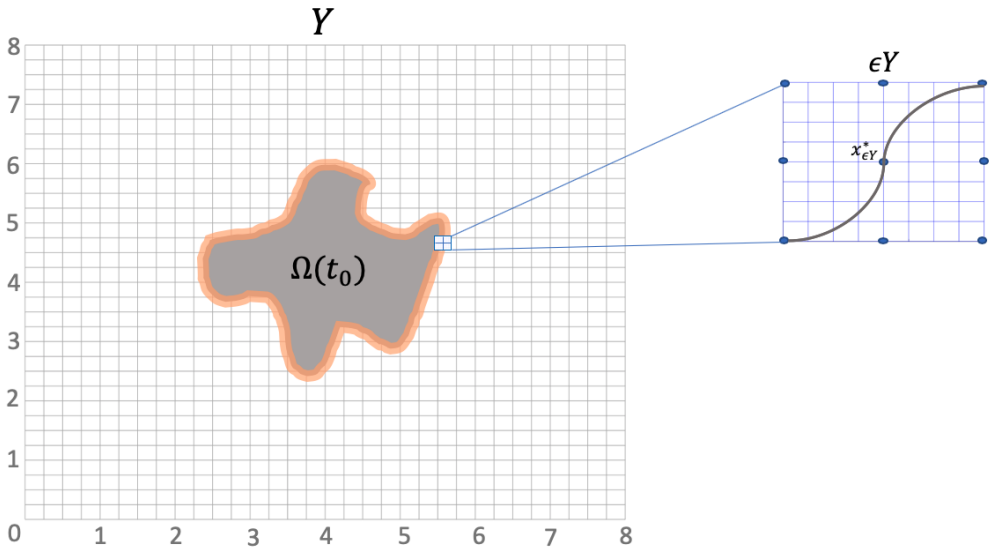

Figure 2.3: Sketch for illustrating the macroscopic domain $\Omega(t_0)$ (left rectangle) and the microscopic domain ϵY (right rectangle) within the tissue domain Y. The orange thick line represents the expanded cancer region $\Omega(t_0 + \Delta t)$ where it is given by the set of points $\widetilde{x}_{\epsilon Y} := x^*_{\epsilon Y} + s(x^*_{\epsilon Y})$ (see details in 2.4).

domain E. Hence, the integral 2.7 on the region M could be approximated by the following midpoint formula (Trucu et al., 2013):

$$\int_M f = \sum f(E_c)\lambda(E), \tag{2.10}$$

where E_c is the central mass of E and $\lambda(E)$ is the Lebesgue measure of E. Moreover, we denote the time of the source funtion 2.7 to be constant within the interval $[0, \Delta t]$. Hence, the source integral 2.7 is computed at each macro-micro contact mesh points 2.9 namely,

$$\hat{f}^{\epsilon Y}_{MDEs}(x^*_c) = \frac{\int_{\mathbf{B}(x^*_c, 2\epsilon)\cap\Omega(t_0)} c\,(x^*_c, t_0 + \Delta t)\,dx}{\lambda(\mathbf{B}(x^*_c, 2\epsilon) \cap \Omega(t_0))}, \tag{2.11}$$

where x^*_c represents the common points of the macro and the micro mesh points i.e. $c = 1, 2, ..., p_{\epsilon Y}$. In additional to calculating the source integral on the contact

mesh points, we still need to compute the source function over the remaining micro-domian namely, for all y belonging to $\epsilon Y \in \mathcal{P}^*_\epsilon(t)$. To this done, they take advantage of the current contact macro-micro nodes, then they denote the basis functions B_f of the set of the entire finite element for these nodes as follows:

$$B_f = \{\phi_{x^*_c} | c = 1, 2, ..., p_{\epsilon Y}\}. \tag{2.12}$$

Consequently, for each single node of the micro-domain who does not contact with any point of the tissue domain nodes, and with taking into account the convex combination principle, we assume that, for any three points $x_{i1}, x_{i2}, x_{i3} \in \{x_1, x_2, ..., x_{p_{\epsilon Y}}\}$ within the closure of $\epsilon Y \subset \mathcal{P}^*_\epsilon(t)$ where $y \in \text{Convex}\{x_{i_1}, x_{i_2}, x_{i_3}\}$, we suppose the source function is given by the following finite element approximated form:

$$\hat{f}^{\epsilon Y}_{MDEs}(y) = \hat{f}^{\epsilon Y}_{MDEs}(x_{i_1})\phi_{x_{i_1}}(y) + \hat{f}^{\epsilon Y}_{MDEs}(x_{i_2})\phi_{x_{i_2}}(y) + \hat{f}^{\epsilon Y}_{MDEs}(x_{i_3})\phi_{x_{i_3}}(y),$$

otherwise, we have

$$\hat{f}^{\epsilon Y}_{MDEs}(y) = 0.$$

Accordingly, the values of the source function 2.7 is obtained on all micro-domain nodes namely, for all $\epsilon Y \in \mathcal{P}^*_\epsilon(t)$. Hence, the microscopic dynamics system through the finite element method to obtain the spatial distribution of MDEs at the final microscopic time. However, for the time integration, this uses trapezoidal predictor corrector method. Furthermore, the moving boundary approach of the tumour is obtained through the following assumption, for every $y \in \epsilon Y$, the midpoint of $[\partial\Omega(t_0)]_{\epsilon Y}$ $(x^*_{\epsilon Y})$ would take a direction $\eta_{\epsilon Y}$ to reach to the closest macro-mesh point if and only if the transitional probability exceeds the threshold $\omega_{\epsilon Y} \in (0, 1)$. Other-

wise, the midpoint $x^*_{\epsilon Y}$ does not move to any other location.

2.4.2 Tissue Thresholds within the bottom-up feedback link

As discussed in Trucu et al. (2013), for each $\epsilon Y \in \mathcal{P}(t_0)$, the tissue thresholds $\omega(\beta, \epsilon Y)$ explore the level of ECM degradation on $\epsilon Y \setminus \Omega(t_0)$, this way assessing the likelihood of movement of the midpoint $x^*_{\epsilon Y}$ to the new location prescribed by $s(x^*_{\epsilon Y})$, namely to its new position $\widetilde{x}_{\epsilon Y} := x^*_{\epsilon Y} + s(x^*_{\epsilon Y})$. We adopt here the same form as in Trucu et al. (2013), and so these tissue thresholds are given by

$$\omega(\beta, \epsilon Y) = \begin{cases} Q_1(\beta, \epsilon Y), & \text{if } \frac{u_{\Omega(t_0)}(\widetilde{x}_{\epsilon Y}, t_0+\Delta t)}{\sup\limits_{z\in\partial\Omega(t_0)} (u_{\Omega(t_0)}(z, t_0+\Delta t))} \leq \beta, \\ \\ Q_2(\beta, \epsilon Y), & \text{if } \frac{u_{\Omega(t_0)}(\widetilde{x}_{\epsilon Y}, t_0+\Delta t)}{\sup\limits_{z\in\partial\Omega(t_0)} u_{\Omega(t_0)}(z, t_0+\Delta t)} > \beta \end{cases} \tag{2.13}$$

where $\beta \in (0, 1)$ represents the most suitable conditions that facilitate invasion, with the expressions $Q_1(\beta, \epsilon Y)$ and $Q_2(\beta, \epsilon Y)$ denoting

$$Q_1(\beta, \epsilon Y) := sin(\tfrac{\pi}{2}(1 - \tfrac{1}{\beta}\frac{u_{\Omega(t_0)}(\widetilde{x}_{\epsilon Y}, t_0+\Delta t)}{\sup\limits_{z\in\partial\Omega(t_0)} u_{\Omega(t_0)}(z, t_0+\Delta t)})),$$

and

$$Q_2(\beta, \epsilon Y) := sin(\tfrac{\pi}{2(1-\beta)}(\frac{u_{\Omega(t_0)}(\widetilde{x}_{\epsilon Y}, t_0+\Delta t)}{\sup\limits_{z\in\partial\Omega(t_0)} u_{\Omega(t_0)}(z, t_0+\Delta t)} - \beta)).$$

2.5 Movement of the tumour boundary triggered by the micro-dynamics

On each micro-domain $\epsilon Y \in \mathcal{P}_\epsilon^*(t_0)$, the MDEs interact with the ECM that they meet once transported in the peritumoural region $\epsilon Y \setminus \Omega(t_0)$, causing degradation that significantly influence the pattern of tumour progression. Indeed, the topological shape and degree of degradation of the ECM is in direct correlation with the pattern of advancing front of MDEs that exercise their cross interface random movement as well as the amount of MDEs being transported by this molecular front. This molecular activity is up-taken at macro-scale, giving rise to direction of choreographic movement, $\eta_{\epsilon Y}$, and displacement magnitude, $\xi_{\epsilon Y}$, for the relocation of the tumour boundary captured by the micro-domain, i.e, $[\partial\Omega(t)]_{\epsilon Y}$, that is represented at tissue level through the movement of the associated boundary midpoint $x^*_{\epsilon Y} \in [\partial\Omega(t)]_{\epsilon Y}$. This will ultimately dictate the relocation of the tumour boundary provided that significant but not complete degradation of the ECM has taken place on the ϵY

In brief, to these two movement characteristics $\eta_{\epsilon Y}$ and $x^*_{\epsilon Y} \in [\partial\Omega(t)]_{\epsilon Y}$, as detailed in Trucu et al. (2013), the regularity property of the Lebesgue measure is used as a selection criterion to identify a suitable dyadic decomposition $\{\mathcal{D}_i\}_{i=1,2^s}$ on $epsilonY$. Then, from collection $\{\mathcal{D}_i\}_{i=1,2^s}$, we sub-select only those furthers away dyadic cubes D_j from the tumour interface where a significant level of enzymes $m(\cdot,\cdot)$ have been transported, i.e, a level of enzymes above the mean-values of the enzymes transported outside the cancer region, namely above $\frac{1}{\lambda(\epsilon Y\setminus\Omega(t_0))}\int\limits_{\epsilon Y\setminus\Omega(t_0))} m(y,\tau)dy$, which corresponds to the level of significant ECM degradation. Collecting all these cubes in a subfamily $\{\mathcal{D}_j\}_{j\in\mathcal{I}^*} \subset \{\mathcal{D}_i\}_{i=1,2^s}$, and considering also their associate barycentral positions $\{y_j\}_{j\in\mathcal{I}^*}$

$$\eta_{\epsilon Y} = x^*_{\epsilon Y} + \nu \sum_{l \in \mathcal{I}^*} \Big(\int_{\mathcal{D}_l} m(y, \tau_f) dy \Big) (y_l - x^*_{\epsilon Y}), \;\; \nu \in [0, \infty]. \tag{2.14}$$

$$\xi_{\epsilon Y} := \sum_{l \in \mathcal{I}^*} \frac{\int_{\mathcal{D}_l} m(y, \tau_f) dy}{\sum\limits_{l \in \mathcal{I}^*} \int_{\mathcal{D}_l} m(y, \tau_f) dy} \big| \overrightarrow{x^*_{\epsilon Y} y_l} \big|. \tag{2.15}$$

Notably, the movement of each unique midpoint ϵY^* through ECM components is depends on a particular transitional measure controlling ECM degradation. This measure explore the strength of peritumoural ECM degradation by the incoming front of MDE within the micro-domain ϵY, and is defined by:

$$q^*(\mathcal{A}) := \frac{1}{\int_{\mathcal{A}} m(y, \tau_f) dy} \int_{\mathcal{A} \setminus \Omega(t_0)} m(y, \tau_f) dy, \quad \forall \; \mathcal{A} \in \sum \big(\bigcup_{\epsilon Y \in \mathcal{P}^*_\epsilon} \epsilon Y \big), \tag{2.16}$$

where $\sum \big(\bigcup\limits_{\epsilon Y \in \mathcal{P}^*_\epsilon} \epsilon Y \big)$ is the usual Borel $\sigma-$algebra on ϵY. Hence associating to each midpoint $x^*_{\epsilon Y^*}$, a discrete transitional measure $\tilde{q}^*(x_{\epsilon Y^*}) := q^*(\epsilon Y)$, if this exceeds a certain tissue threshold threshold $\omega_{\epsilon Y} \in (01,)$ to indicate that enough but not complete ECM degradation occurred, then the movement prescribed earlier will be exercised in the direction $\eta_{\epsilon Y}$ and with a displacement magnitude $\eta_{\epsilon Y}$. Hence, the new tumour edge will be formed as a combination of both unmoved points and the moved points, thus the new tumour boundary will consists the union of both set of points:

$$\{ \widetilde{x^*_{\epsilon Y^*}} | \epsilon Y \in \mathcal{P}^*_{\epsilon Y} \text{ such that } q^*(x_{\epsilon Y^*}) \geq \omega_{\epsilon Y} \} \tag{2.17}$$

and

$$\{ x^*_{\epsilon Y^*} | \epsilon Y \in \mathcal{P}^*_{\epsilon Y} \text{ such that } q^*(x_{\epsilon Y^*}) < \omega_{\epsilon Y} \}. \tag{2.18}$$

Consequently, the new generated initial conditions of the macroscopic system will

be in the following form (Trucu et al., 2013):

$$c_{\Omega(t_0+\Delta t)}(x,t_0) := c(x,t_0+\Delta t)(\chi_{\Omega(t_0)\setminus \bigcup\limits_{\epsilon Y\in\mathcal{P}_\epsilon^*}\epsilon Y} * \psi_\gamma),$$

$$v_{\Omega(t_0+\Delta t)}(x,t_0) := v(x,t_0+\Delta t)\chi_{Y\setminus \bigcup\limits_{\epsilon Y\in\mathcal{P}_\epsilon^*}\epsilon Y} * \psi_\gamma). \tag{2.19}$$

2.5.1 Generating the initial conditions for the next macro-stage on $[t_0+\Delta t, t_0+2\Delta t]$

Based on both computational process on $\Omega(t_0+\Delta t)$ and the interpolation points $\widetilde{x^*_{\epsilon Y}}$, we obtain a new expanded tumour boundary $\partial\Omega(t_0+\Delta t)$. Hence, at the macro-scale, we get a new initial condition as follows (Trucu et al., 2013):

$$c(x_{i,j},t_0+\Delta t) = \begin{cases} c^k_{i,j}, & x_{i,j}\in\overline{\Omega(t_0)}, \\ \frac{1}{4}(c^k_{i-1,j}+c^k_{i+1,j}+c^k_{i,j-1}+c^k_{i,j+1}), & x_{i,j}\in\overline{\mathbf{B}(\overline{\Omega(t_0)},h)}\setminus\overline{\Omega(t_0)}, \\ 0, & x_{i,j}\notin\overline{\mathbf{B}(\overline{\Omega(t_0)},h)}, \end{cases}$$

where $\{x_{i,j}|i,j=1,...,q\}$ represents the macro mesh points in the tissue domain Y. Moreover, the over-line represents the topological closure of the set (see details in (Trucu et al., 2013)).

Chapter 3

Novel Multiscale Modelling of Cancer Response to Oncolytic Viral Therapy

Oncolytic viruses (OV) are viruses that can replicate selectively within cancer cells and destroy them. While the past few decades have seen significant progress related to the use of these viruses in clinical contexts, the success of oncolytic therapies is dampened by the complex spatial tumour-OV interactions. In this work, we present a novel multiscale moving boundary modelling for the tumour-OV interactions, which is based on coupled systems of partial differential equations both at macro-scale (tissue-scale) and at micro-scale (cell-scale) that are connected through a double feedback link. At the macro-scale, we account for the coupled dynamics of uninfected cancer cells, OV-infected cancer cells, extracellular matrix (ECM) and oncolytic viruses. At the same time, at the micro scale, we focus on essential dynamics of urokinase plasminogen activator (uPA) system which is one of the important proteolytic systems responsible for the degradation of the ECM, with notable influence

in cancer invasion. While sourced by the cancer cells that arrive during their macro-dynamics within the outer proliferating rim of the tumour, the uPA micro-dynamics is crucial in determining the movement of the macro-scale tumour boundary (both in terms of direction and displacement magnitude). In this investigation, we consider three scenarios for the macro-scale tumour-OV interactions. While assuming the usual context of reaction-diffusion-taxis coupled PDEs, the three macro-dynamics scenarios gradually explore the influence of the ECM taxis over the tumour - OV interaction, in the form of haptotaxis of both uninfected and infected cells populations as well as the indirect ECM taxis for the oncolytic virus. Finally, the complex tumour-OV interactions is investigated numerically through the development a new multiscale moving boundary computational framework. While further investigation is needed to validate the findings of our modelling, for the parameter regimes that we considered, our numerical simulations indicate that the viral therapy leads to control and decrease of the overall cancer expansion and in certain cases this can result even in the elimination of the tumour.

3.1 Introduction

Oncolytic virotherapy (based on either naturally-occurring or genetically-engineered viruses) is a promising therapeutic approach for cancer treatment Lawler et al. (2017). However, despite the fact that multiple oncolytic viruses are currently under clinical development Lawler et al. (2017), this type of therapy still has some limitations in terms of efficacy (as observed in various clinical trials) Fukuhara et al. (2016). This relatively modest oncolytic efficacy is not only the result of premature virus clearance due to circulating antibodies and various immune cells Alemany (2013), but also the result of physical barriers inside tumours (e.g., interstitial fluid pressure, extracellular matrix (ECM) deposits, or tight inter-cellular junctions) Vähä-koskela

and Hinkkanen (2014); Wong et al. (2010). To improve the intra-tumoural spread of oncolytic viruses, different experimental and clinical approaches are currently being considered: from modifications of the immune response to favour virus replication and tumour lysis Wong et al. (2010), to modifications of the physical barriers (e.g., via ECM degradation) to improve virus spread Dmitrieva et al. (2011).

In this study we consider a mathematical modelling and computational approach to help us improve our understanding of the physical barriers that limit virus spread. The use of mathematical models to understand the temporal and spatio-temporal dynamics of viruses (including oncolytic viruses) has seen great developments over the last three decades Perelson et al. (1993, 1996); Nowak and May (2000); Wodarz and Komarova (2009); Macnamara and Eftimie (2015); Wodarz (2016); Santiago et al. (2017). While the majority of these models focused on the temporal dynamics of oncolytic viruses (mainly due to the availability of temporal data) Wodarz et al. (2014); Laaroussi et al. (2014); Bajzer et al. (2008); Wodarz (2016); Agarwal and Bhadauria (2011); Wodarz and Komarova (2009); Kim et al. (2015); Malinzi et al. (2015); Dingli et al. (2009); Nowak and May (2000), more recent advances in tumour imaging generated data on the spatial spread of tumours and viruses, which then led to the development of different mathematical models investigating the spatial spread of these viruses Malinzi et al. (2015); Nowak and May (2000); Wodarz et al. (2012); Wollmann et al. (2005); Camara et al. (2013); Malinzi et al. (2017).

All these temporal and spatio-temporal models for oncolytic virus therapies usually focus on one single spatial or temporal scale. In this context potential insights from the wide range of singe-scale spatio-temporal modelling approaches for cancer invasion (such as those proposed in Adam (1986); Anderson et al. (2000); Byrne and Chaplain (1996b); Gatenby and Gawlinski (1996); Greenspan (1976); Perumpanani et al. (1996, 1998); Webb et al. (1999); Andasari et al. (2011); Anderson (2005);

Byrne et al. (2001); Chaplain and Lolas (2005); Deakin and Chaplain (2013) and, in particular, those involving the theory of mixtures proposed in Chaplain et al. (2006); Preziosi and Tosin (2009); Psiuk-Maksymowicz (2013)) become increasingly relevant to this area, as highlighted and explored by a number of recent works Jacobsen et al. (2015); Friedman and Lai (2018); Kim et al. (2014); Ratajczyk et al. (2017). Nevertheless, since the process of cancer development is a complex phenomenon that involves interlinked phenomena that occur at different scales, it is important to capture these multiscale aspects also during the tumour-oncolytic virus interactions. To that end, the multiscale modelling of cancer invasion introduced over the past decade in the mathematical literature Martins et al. (2007); Stolarska et al. (2009); Alemani et al. (2012); Trucu et al. (2013); Peng et al. (2017) paved the way for exploring the tumour-OV interaction in a multiscale fashion. However, to our knowledge, there are not many multi-scale mathematical models for the oncolytic viral therapies and tumour-viral interactions, with Paiva et al. (2009) being the only reference that we could find in the literature. In that study (Paiva et al., 2009), the mathematical model is assumed to be given at two scales, namely, the tissue scale (macroscopic scale) and the cellular (mesoscopic scale). At the macroscopic scale, the distribution of nutrients and free viruses is represented by reaction-diffusion equations, while the cell division, death, infection, and lysis are computed within the mesoscopic scale by basic probabilistic rules.

In this paper we will introduce a novel multiscale modelling framework for the tumour-OV interaction in which the macroscopic (tissue-scale) dynamics of the cancer and oncolytic virus densities will be connected via a double feedback loop to the microscopic (cell-scale) proteolytic dynamics of the urokinase plasminogen activator system (uPA) that takes place at the invasive edge of the tumour.

3.2 Multiscale Hypothesis and Settings: the Novel Two-Scale Moving Boundary Modelling Approach for Tumour-OV Interactions

Building on the two-scale moving boundary framework introduced first by Trucu et al. in (Trucu et al., 2013) and later explored in (Peng et al., 2017) in the context of the uPA System, in this work we address the genuinely multiscale nature of tumour-OV interaction through a new multiscale modelling approach. Specifically, the tissue-scale (macro-scale) in tumour-OV interaction is here coupled with the cell-scale (micro-scale) tumour invasive edge molecular dynamics of the uPA System. Therefore, before exploring further their crucial cross-talk, we distinguish here the two levels of dynamics, namely *macro-scale* and *micro-scale*, which at this stage can be generally described mathematically as follows.

On one hand, at macro-scale, at any spatio-temporal macro-node (x,t), a part of the cancer cells population $c(x,t)$ becomes dynamically infected by an incoming oncolytic virus $v(x,t)$, giving rise to an infected cancer cells population $i(x,t)$, causing these to die, and this way to be eliminated from the total tumour mass $(c+i)(x,t)$. As this interaction does occur in the presence of the surrounding ECM density $u(x,t)$ and, per unit time, this is governed by both random motility and by various forms of taxis of both uninfected and infected as well as of the oncolyotic virus towards ECM gradients. Thus, denoting for the moment with $\mathcal{T}$ the resulting *4D-reaction-diffusion-taxis* differential operator of order 2, we obtain that the macro-dynamics can be written as

$$\mathcal{T}(c,i,u,v)^T = \mathbf{0} \tag{3.1}$$

were $\mathcal{T}$ will be specified in detail in the next section.

On the other hand, at micro-scale, the proteolytic activity of the uPA System occurring at the invasive edge of the tumour exercises a cross-tumour boundary local enzymatic transport within a cell-scale neighborhood of the interface of the expanding tumour $\Omega(t)$, crucially contributing towards its dynamics changes in morphology with respect to time. Therefore, at any spatio-temporal micro-node (y, τ), considering the three components of the uPA System, namely the urokinase plasminogen activator (uPA) $a(y, \tau)$, plasminogen activator inhibitor (PAI-1) $p(y, \tau)$ and plasmin $m(y, \tau)$, per unit time their dynamics is driven by random molecular motility as well as their production and natural decay. Therefore, we can express this in the form of a coupled system of reaction diffusion equations. Hence, similar to the macro-scale, denoting here the resulting *3D-reaction-diffusion* operator by $\mathcal{Z}$, the micro-dynamics can therefore be expressed as

$$\mathcal{Z}(a, p, m)^T = \mathbf{0} \tag{3.2}$$

where the form of the differential operator Z will be made explicit in the next section. Following a similar two scale approach as in (Trucu et al., 2013; Peng et al., 2017), within a maximal tissue-scale region Y, the macro-scale tumour-OV dynamics (3.1) occurring on the growing tumour support $\Omega(t) \subset Y$ is directly linked through a *"macro-micro cross-talk"* to the uPA micro-dynamics (3.2) that takes place on a cell-scale neighbourhood of the tumour boundary $\partial\Omega(t)$, as illustrated in schematic Fig. 3.1. To that end, the cell-scale neighbourhood of $\partial\Omega(t)$ that was introduced in (Trucu et al., 2013) and is given by a covering bundle of overlapping (*half-way*) micro-domains $\{\epsilon Y\}_{\epsilon Y \in \mathcal{P}(t)}$ enables the decoupling of the micro-dynamics in a bundle of micro-processes taking place on each $\epsilon Y \in \mathcal{P}(t)$, and as a consequence, this *macro-micro cross-talk* is realised through a double-feedback loop consisting of both *top-*

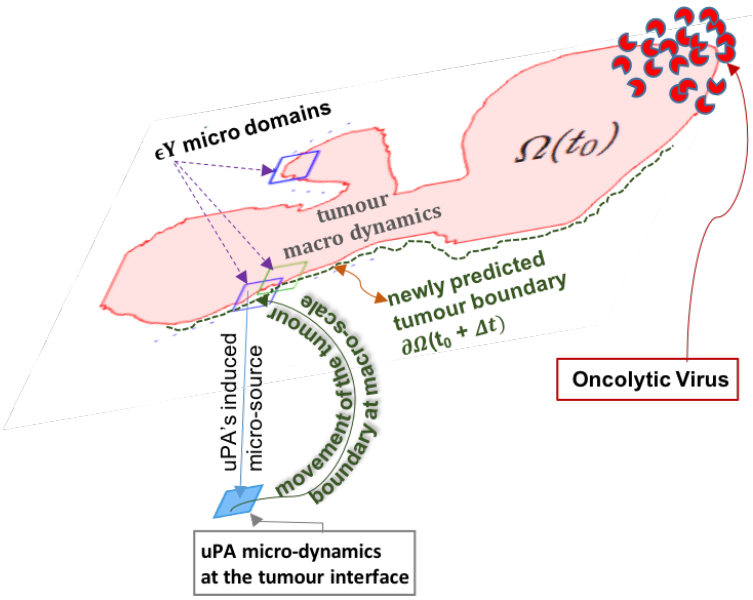

Figure 3.1: Schematic of the multiscale modelling approach to tumour-virus interaction

down and *bottom-up* links between the macro-dynamics on $\Omega(t)$ and the uPA micro-dynamics occuring on each $\epsilon Y \in \mathcal{P}(t)$. While we postpone the detailed description of the double feedback loop until the next section, briefly, this is structured as follows.

On one hand, the *top-down* link between macro-scale and micro-scale explores the naturally arising source for the uPA and the non-local behaviour of PAI-1 removal, which are enabled by the cancer cells and ECM micro-environment within the neighbourhood of the tumour outer proliferating rim that secrets them. Thus, on a time perspective $[t_0, t_0 + \Delta t]$ this arises as the direct contribution of the macroscopic densities of cancer cells c and i as well as of the ECM u, and in brief, at any spatio-temporal microscopic node $(\tau, y) \in [0, \Delta t] \times \epsilon Y$, these can be mathematically expressed via non-local terms of the form

$$f^{\epsilon Y}_{uPA}(\tau, y) = \frac{\int_{\mathbf{B}(y,\delta)\cap supp\{c+i\}} K_1(c(s, t_0+\tau), i(s, t_0+\tau), s-y)ds}{\lambda(\mathbf{B}(y, \delta) \cap supp\{c+i\})} \tag{3.3}$$

and

$$f^{\epsilon Y}_{PAI-1}(\tau, y) = \frac{\int\limits_{\mathbf{B}(y,\delta)} K_2(u(s, t_0+\tau), s-y)ds}{\lambda(\mathbf{B}(y, \delta))}, \tag{3.4}$$

where λ is the Lebesgue measure on $\mathbb{R}^2$ and the mappings $\mathbb{R} \ni z \longmapsto K_1(\cdot, \cdot, z) \in \mathbb{R}$ and $\mathbb{R} \ni z \longmapsto K_2(\cdot, z) \in \mathbb{R}$ are compactly supported radially symmetric kernels that quantify the contribution of the involved macroscopic densities with respect to their spatial distribution and whose choice will be discussed in Section 3.4. In the presence of these non-local behaviours induce from the macro-scale, the uPA System exercise its spatio-temporal micro-dynamics briefly outlined above and detailed in Section 3.4.

Finally, the *bottom up* link is conveyed by the key contribution that the micro-dynamics has in determining the characteristics of macro-scale tumour boundary movement. The tumour boundary relocation is caused by the local invasion of the peritumoural region whose extent and orientation are dictated by the pattern of degradation of the ECM by the uPA System acting at micro-scale within the outer part of the cell-scale neighbourhood of the tumour boundary (which is given here by the union of all the micro-domains $\epsilon Y \in \mathcal{P}(t)$). In its turn, the pattern of ECM degradation is dictated by the regions of significant transport of proteolytic enzymes within each micro-domain ϵY. Proceeding as in (Trucu et al., 2013), these regions are determined here by the furthest away part of the level sets of significant proteolytic enzymes within each ϵY with respect to the tumour boundary $\partial\Omega(t) \cap \epsilon Y$, whose cumulative revolving orientation leads to the establishment of the characteristics of the tumour boundary movement

$$\begin{aligned} &s : \partial\Omega(t) \to \mathbf{S^1} \times (0, \infty), \\ &\text{given by} \\ &s(z) := (\nu(z), \xi(z)), \qquad \forall z \in \partial\Omega(t), \end{aligned} \tag{3.5}$$

with $\mathbf{S^1}$ being the usual unit sphere in $\mathbb{R}^2$, and $\nu(\cdot)$ and $\xi(\cdot)$ representing the direction of movement and displacement magnitude, respectively. Provided that sufficient degradation but not complete destruction of the ECM has been exercised by the micro-scale uPA processes, the boundary will be relocated in the direction dictated by the boundary movement law $s(\cdot)$ introduced above, and the macro-dynamics is continued on the newly obtained domain.

3.3 Macroscopic Modelling Scenarios for the Virus-Tumour Interaction

In the following we describe in detail the various macro-scale components and their dynamics relations, which were compactly represented by the macroscopic operator equation (3.1) introduced in the previous section. These components are: the density of uninfected cancer cells $c(x,t)$, the density of infected cancer cells $i(x,t)$, the density of the extracellular matrix $u(x,t)$, and the density of the oncolytic virus particles $v(x,t)$.

Uninfected Cancer Cells: $c(x,t)$ Following biological evidence from several experimental studies (Stroock and Varadhan, 1997), we assume that the cancer cells density changes due to random cell movement (with D_c the random motility coefficient) and to directed haptotactic movement towards higher ECM gradients (with η_c the haptotactic coefficient). Moreover, cancer cells can proliferate logistically at a rate μ_1 Laird (1964); Guiot et al. (2003), and can decay due to virus infection at a rate ρ. These assumptions can be translated into the following equation:

$$\frac{\partial c}{\partial t} = D_c \Delta c - \eta_c \nabla \cdot (c \nabla u) + \mu_1 c(1-c) - \rho c v. \tag{3.6}$$

Infected Cancer Cells: $i(x,t)$ We assume that also the infected cancer cells can move randomly (with D_i the random motility coefficient) (Petrie et al., 2009; Weiger et al., 2013; Huda et al., 2018; Wu et al., 2014; Stroock and Varadhan, 1997). As discussed above, these cells are infected at a rate ρ by the oncolytic virus. Finally, these infected cells die at a rate δ_i. These assumptions are described by the following equation:

$$\frac{\partial i}{\partial t} = D_i \Delta i + \rho c v - \delta_i i. \tag{3.7}$$

Extracellular Matrix (ECM): $u(x,t)$ We assume that the ECM (and its components) does not move, and thus we ignore any migration and diffusion terms. However, since ECM is continuously remodelled by cells in the environment (Cox and Erler, 2011), we describe this remodelling process as the difference between a logistic growth term (describing the deposition of ECM components – in the presence of cancer – at a rate μ_2) and a degradation term (with α_c the rate of ECM degradation by uninfected cancer cells, and α_i the rate of ECM degradation by infected cancer cells.) These assumptions are described by the following equation:

$$\frac{\partial u}{\partial t} = -u(\alpha_c c + \alpha_i i) + \mu_2 u(1 - u - c - i). \tag{3.8}$$

The growth in equation (3.8) describes the logistic remodelling of the ECM, which depends on the presence of all variables in the system. Similar terms have been considered in Andasari et al. (2011); Chaplain and Lolas (2005); Deakin and Chaplain (2013); Trucu et al. (2013); Peng et al. (2017). In contrast, the growth in equation (3.6) models cancer proliferation in the presence of nutrients and its slow down when nutrients are consumed, as justified by the shape of the logistic term Laird (1964); Guiot et al. (2003).

Oncolytic Virus: $v(x,t)$ Based on previous studies (Nowak and May, 2000; Wollmann et al., 2005; Wodarz et al., 2012), we assume that the oncolytic virus can move randomly through the environment, with D_v the random motility coefficient. The level of virus particles increases due to the burst (at a rate b) of the infected tumour cells, which release the new virions in the environment. The reduction in the number of free virus particles is the result of the natural virions' death rate δ_v, and the trapping of these virus particles into the cancer cells at a rate ρ. Therefore, the evolution of the density of virus particles is described by the equation:

$$\frac{\partial v}{\partial t} = D_v \Delta v + bi - \rho cv - \delta_v v. \tag{3.9}$$

Remark: Note that for simplicity, in the above equations (3.6)-(3.8), all variables have been rescaled by their maximum values (i.e., the carrying capacities of the tumour cells and the extracellular matrix).

Therefore, accounting for at the above macro-scale modelling considerations, the macro-dynamics that we have obtained so far is as follows:

Macro-dynamics scenario 1 The new macro-scale scenario of the multiscale modelling approach for the tumour-OV interaction is given by the following system:

$$\begin{cases} \frac{\partial c}{\partial t} = D_c \Delta c - \eta_c \nabla \cdot (c \nabla u) + \mu_1 c(1-c) - \rho cv, \\ \frac{\partial i}{\partial t} = D_i \Delta i + \rho cv - \delta_i i, \\ \frac{\partial u}{\partial t} = -u(\alpha_c c + \alpha_i i) + \mu_2 u(1-u-c-i), \\ \frac{\partial v}{\partial t} = D_v \Delta v + bi - \rho cv - \delta_v v. \end{cases} \tag{3.10}$$

However, expanding now the modelling perspective by accounting within the macro-scale spatial dynamics of the infected cell population not only on its random

movement (approximated here by diffusion) but also on its haptotactic migration against ECM gradients, equation (3.7) is therefore evolved into:

$$\frac{\partial i}{\partial t} = D_i \Delta i - \eta_i \nabla \cdot (i \nabla u) + \rho c v - \delta_i i. \tag{3.11}$$

This leads us to a second scenario for the macro-dynamics which is summarised as follows:

Macro-dynamics scenario 2 In the presence of haptotactic behaviour for the infected cell population, the macro-scale modelling scenario for tumour-OV interaction is therefore extended and is given now by the system:

$$\begin{cases} \frac{\partial c}{\partial t} = D_c \Delta c - \eta_c \nabla \cdot (c \nabla u) + \mu_1 c(1-c) - \rho c v, \\ \frac{\partial i}{\partial t} = D_i \Delta i - \eta_i \nabla \cdot (i \nabla u) + \rho c v - \delta_i i, \\ \frac{\partial u}{\partial t} = -u(\alpha_c c + \alpha_i i) + \mu_2 u(1-u-c-i), \\ \frac{\partial v}{\partial t} = D_v \Delta v + b i - \rho c v - \delta_v v. \end{cases} \tag{3.12}$$

Finally, we note that a major obstacle that creates difficulties in having a successful viral therapy is virus motility blockage exercised by ECM components. Recent efforts to minimising virus size makes it possible for the virus particles to move through ECM components (Vähä-koskela and Hinkkanen, 2014). While knowing that though viruses do not have an autonomous motility, the penetration of the ECM is done via other factors, such as matrix degrading enzymes as detailed in Choi et al. (2013). Therefore, for the dynamics of the virus population, in addition to the usual consideration of virus diffusion, assumed by other authors Nowak and May (2000); Wollmann et al. (2005); Camara et al. (2013); Malinzi et al. (2015); Vähä-koskela and Hinkkanen (2014), we will also consider here the ECM-OV interac-

tions. To that end, as discussed in Vähä-koskela and Hinkkanen (2014), while ECM acts usually as a barrier agains OV motility, its regions of lower levels of **density** provide opportunities for OV to penetrate through its components and potentially interact with a larger cancer cell-surface cumulated areas, this way gaining further opportunities to infect the nearby cancer cells. This leads to an ECM-OV taxis behaviour that affects the random motility of the virus, which mathematically can be incorporated into equation (3.9) leading to the following reaction-advection-diffusion equation:

$$\frac{\partial v}{\partial t} = D_v \Delta v - \eta_v \nabla \cdot (v \nabla u) + bi - \rho c v - \delta_v v, \tag{3.13}$$

where η_v is the ECM-OV-taxis rate. This brings us to the last and most extended macro-dynamics scenario that we consider in this paper, namely:

Macro-dynamics scenario 3 Accounting also upon the presence of ECM-OV taxis behaviour included in (3.13), the macro-dynamics component of our multiscale approach to tumour-OV interaction is therefore given by:

$$\begin{cases} \frac{\partial c}{\partial t} = D_c \Delta c - \eta_c \nabla \cdot (c \nabla u) + \mu_1 c(1-c) - \rho c v, \\ \frac{\partial i}{\partial t} = D_i \Delta i - \eta_i \nabla \cdot (i \nabla u) + \rho c v - \delta_i i, \\ \frac{\partial u}{\partial t} = -u(\alpha_c c + \alpha_i i) + \mu_2 u(1-u-c-i), \\ \frac{\partial v}{\partial t} = D_v \Delta v - \eta_v \nabla \cdot (v \nabla u) + bi - \rho c v - \delta_v v. \end{cases} \tag{3.14}$$

Remark: Note that since the focus of the model is the interaction between virus and cancer cells in a multi-scale moving boundary context, for simplicity we assume that the outside environment is represented only by the ECM. Therefore, we ignore any other types of cells in the environment: healthy cells, immune cells, etc.

3.4 The Microscopic Proteolytic Dynamics and the Macro-Micro Double Feedback Loop

As established biologically (Hanahan and Weinberg, 2000; Weinberg, 2006; Hanahan and Weinberg, 2011), the cell-scale molecular dynamics of the matrix degrading enzymes at the tumour invasive edge plays a critical role within the cancer cells invasion process. Several important families of matrix degrading enzymes are collectively secreted by the cancer cells within the outer proliferating rim of the tumour exercise a spatial transport in a cell-scale neighbourhood of the the tumour interface and this way cause a degradation of the peritumoural ECM, leading to continuous morphological changes in the macro-scale tumour boundary and ultimately resulting in further progression of the cancer in the surrounding tissue. Among these proteolytic enzymes, alongside the notable contribution of the family of matrix metalloproteinases (MMPs), a pivotal role within cancer invasion is played by the urokinase plasminogen activator (uPA) system, which not only that decomposes the ECM but also has implications in activating some of the MMPs as well as interfering with the activity of cytokines and growth factors (see Venkatraman et al. (2012)).

As briefly outlined in Section 3.2, both uninfected and infected tumour cells arriving during their dynamics within the outer proliferating rim of the tumour are able to secrete uPA. Thus, at any time instance t_0, within any micro-domain $\epsilon Y \in \mathcal{P}(t_0)$, a source of uPA arises this way at any micro-point $y \in \epsilon Y \cap \Omega(t_0)$ as a collective contribution of both infected and uninfected cells from the outer proliferating rim that arrive within a $\delta > 0$ distance from y. Therefore, assuming, no spatial discrimination between the cells secreting the uPA within $\mathbf{B}(y, \delta) \cap \Omega(t_0)$, we obtain that the spatially radial symmetric diffusion kernel K_1 appearing in (3.3)

is constant with respect to the spatial variable, this being given by

$$K_1(c(\cdot,\cdot), i(\cdot,\cdot), z) = [\lambda_c c(\cdot,\cdot) + \lambda_i i(\cdot,\cdot)]\chi_{\mathbf{B}(y,\delta)\cap\Omega(t_0)}(\cdot). \tag{3.15}$$

where $\chi_{\mathbf{B}(y,\delta)\cap\Omega(t_0)}(\cdot)$ is the usual characteristic function for the set $\mathbf{B}(y,\delta)\cap\Omega(t_0)$. Thus, we have that the micro-scale uPA source at a spatio-temporal micro-node $(y,\tau) \in (\epsilon Y \cap \Omega(t_0)) \times [0, \Delta t]$ is given by

$$f_{uPA}^{\epsilon Y}(y,\tau) = \frac{\int_{\mathbf{B}(y,\delta)\cap supp\{c+i\}} (\lambda_c c(s, t_0+\tau) + \lambda_i i(s, t_0+\tau))ds}{\lambda(\mathbf{B}(y,\delta)\cap supp\{c+i\})} \tag{3.16}$$

and is zero at any other micro location $y \in \epsilon Y \setminus \Omega(t_0)$. Once secreted, the uPA exercises a local cross-interface transport process, activating plasmin from its inactive state, plasminogen, which is freely available within the ECM. In turn, once activated, plasmin degrades various ECM components.

However, the plasminogen activation process is accompanied also by inhibitors, a notably important one being PAI-1, who binds to the activated uPA and manage to inhibit this. Produced through the activation of plasmin, besides natural decay and binding to uPA, PAI-1 is removed also through binding to the surrounding ECM. Thus, proceeding similar to the case of uPA source, at each spatio-temporal micro-node $(y,\tau) \in \epsilon Y \times [0, \Delta t]$ this loss of PAI-1 through indiscriminate ECM binding can be quantified through (3.4), for the following projection kernel K_2 that is constant with respect to space, namely

$$K_2(u(\cdot,\cdot), z) = u(\cdot,\cdot). \tag{3.17}$$

which gives

$$f^{\epsilon Y}_{PAI-1}(y,\tau) = \frac{\int_{\mathbf{B}(y,\delta)} u(s, t_0+\tau)ds}{\lambda(\mathbf{B}(y,\delta))}. \tag{3.18}$$

Thus, denoting the micro-scale densities of uPA by $a(y,\tau)$, PAI-1 by $p(y,\tau)$, and plasmin by $m(y,t)$, and proceeding as in Trucu et al. (2016), in brief, the dynamics of the tumour invasive edge proteolytic micro-processes can be is described as follows. Per unit time, the uPA molecular population $a(\cdot,\cdot)$ changes through diffusion (with a random motility coefficient D_a) while being produced (at a rate ψ_{12}) and bound by cancer cells' uPA receptors (uPAR) (at a rate ψ_{13}), as well as being inhibited by PAI-1 density $p(\cdot,\cdot)$ (at a rate ψ_{11}). Therefore, its dynamics is given by

$$\frac{\partial a}{\partial \tau} = \underbrace{D_a \Delta a}_{\text{diffusion}} - \underbrace{\psi_{11} a p}_{\text{uPA/PAI-1}} + (\underbrace{\psi_{12}}_{\text{production}} - \underbrace{\psi_{13} a}_{\text{uPA/uPAR}}) f^{\epsilon Y}_{uPA}(y,\tau) \tag{3.19}$$

Further, the inhibitor PAI-1 density change per unit time is triggered by local diffusion (with a diffusion coefficient D_p), production through plasmin activation (at a rate ψ_{23}) as well as removal from the system through binding to uPA (at a rate ψ_{21}) and to surrounding ECM (at a rate ψ_{22}). Thus, PAI-1 micro-dynamics is given by

$$\frac{\partial p}{\partial \tau} = \underbrace{D_p \Delta p}_{\text{diffusion}} - \underbrace{\psi_{21} a p}_{\text{uPA/PAI-1}} - \underbrace{\psi_{22} p\, f^{\epsilon Y}_{PAI-1}(y,\tau)}_{\text{PAI-1/ECM}} + \underbrace{\psi_{23} m}_{\text{production}} . \tag{3.20}$$

Finally, the change in plasmin density per unit time is due to local diffusion (with a diffusion coefficient D_m), natural degradation (at a rate ψ_{33}) and production due to both direct plasminogen activation (through uPA binding to uPAR at a rate ψ_{31}) and as well as binding of PAI-1 to neighbouring ECM (at a rate ψ_{32}) that indirectly enable further opportunities for plasmin activation. Thus, plasmin's micro-dynamics

is given by

$$\frac{\partial m}{\partial \tau} = \underbrace{D_m \Delta m}_{\text{diffusion}} + \underbrace{\psi_{31} a f^{\epsilon Y}_{uPA}(y,\tau)}_{\text{uPA/uPAR}} + \underbrace{\psi_{32} p f^{\epsilon Y}_{PAI-1}(y,\tau)}_{\text{PAI-1/ECM}} - \underbrace{\psi_{33} m}_{\text{decay}}. \tag{3.21}$$

Therefore, the microscopic proteolytic dynamics is given by the following 3D-reaction-diffusion-taxis system:

$$\begin{cases} \frac{\partial a}{\partial \tau} = D_a \Delta a - \psi_{11} a p + (\psi_{12} - \psi_{13} u) f^{\epsilon Y}_{uPA}(y,\tau), \\ \frac{\partial p}{\partial \tau} = D_p \Delta p - \psi_{21} a p - \psi_{22} p \, f^{\epsilon Y}_{PAI-1}(y,\tau) + \psi_{23} m, \\ \frac{\partial m}{\partial \tau} = D_m \Delta m + \psi_{31} a f^{\epsilon Y}_{uPA}(y,\tau) + \psi_{32} p f^{\epsilon Y}_{PAI-1}(y,\tau) - \psi_{33} m, \end{cases} \tag{3.22}$$

as we assume *"no molecular memory"* from any previous macro-micro stages, the micro-dynamics system (3.22) is accompanied by zero initial conditions, i.e.,

$$a(y,0) = 0, \quad p(y,0) = 0, \quad m(y,0) = 0, \quad \forall y \in \epsilon Y.$$

Furthermore, as we there is no molecular transport across the interface of the micro-domains ϵY, we assume also zero Neumann boundary conditions, i.e.,

$$\left.\frac{\partial a}{\partial n}\right|_{\epsilon Y} = 0; \quad \left.\frac{\partial p}{\partial n}\right|_{\epsilon Y} = 0; \quad \left.\frac{\partial m}{\partial n}\right|_{\epsilon Y} = 0.$$

As introduced and detailed in Trucu et al. (2013), on each boundary micro-domain ϵY, it is the pattern of significant ECM degradation (caused by the advancing distribution of plasmin) that will dictate the relocation of the tumour boundary within the peritumoural region. Indeed, the micro-scale proteolytic dynamics determines directly the direction of movement and displacement magnitude that is

briefly summarised in (3.5) and is represented back at the macro-scale through the movement of the *micro-domains mid points* $\{x^*_{\epsilon Y}\}_{\epsilon Y \in \mathcal{P}(t_0)}$, as detailed in Trucu et al. (2013); Peng et al. (2017). However, the boundary point $x^*_{\epsilon Y} \in \epsilon Y$ will exercise the movement prescribed by $s(x^*_{\epsilon Y})$ provided that the extent of degradation of ECM, which is explored here through the *outer degradation measure* outlined in Trucu et al. (2013); Peng et al. (2017),

$$q^* : \Sigma(\bigcup_{\epsilon Y \in \mathcal{P}(t_0)}) \to [0, \infty]$$

given by

$$q^*(G) := \begin{cases} \frac{\int_{G \setminus \Omega(t_0)} m(y, \Delta t) dy}{\int_G m(y, \Delta t) dy}, & \lambda(G) > 0, \\ 0, & otherwise, \end{cases} \tag{3.23}$$

is significant but not complete. Therefore, the representative mid point will exercise the movement prescribed by $s(x^*_{\epsilon Y})$ provided that

$$q^*(\epsilon Y) > \omega(\epsilon Y, \beta) \tag{3.24}$$

where $\omega(\epsilon Y, \beta)$ is a local tissue threshold and the parameter $\beta \in (0, 1)$ explore the optimal conditions for movement, see 2.4.2. Once the movement has been exercised, the macro-scale tumour domain $\Omega(t_0)$ progresses to its new shape $\Omega(t_0 + \Delta t)$, where the multiscale dynamics is continued with the next macro-micro stage.

In other words, the cross-interface transport exercised by the uPA system within each micro-domain ϵY (captured in (3.22)) leads to a pattern of degradation of the peritumoural ECM within $\epsilon Y \setminus \Omega(t_0)$ resulting into an important *bottom-up* feedback to the tissue-scale that ultimately dictates the way the macro-scale tumour boundary is relocated, as illustrated in Figure 3.1. Thus, to capture this feedback

link, we follow the multiscale approach introduced in Trucu et al. (2013) and further discussed in Peng et al. (2017), which enables us to explore the regions of significant ECM degradation within $\epsilon Y \setminus \Omega_{t_0}$ and ultimately to determine a unique direction of movement $\eta_{\epsilon Y}$ and a displacement magnitude $\xi_{\epsilon Y}$ that indicates the way the boundary captured by ϵY, namely $\epsilon Y \cap \partial\Omega(t_0)$ is progressed further in the domain (please see Trucu et al. (2013); Peng et al. (2017) for full details). This enables us to capture the choreographic movement of the portion of the boundary $\epsilon Y \cap \partial\Omega(t_0)$ and to represented this at macro-scale through the movement of the *central boundary point of* $\epsilon Y \cap \partial\Omega(t_0)$ to a new position in the direction $\epsilon Y \cap \partial\Omega(t_0)$ by a displacement magnitude $\xi_{\epsilon Y}$. Finally, under the incidence of this bottom-up feedback induced by the tumour invasive edge micro-dynamics over each time interval $[t_0, t_0 + \Delta t]$, the boundary of the tumour $\Omega(t_0)$ is eventually progressed into a newly relocated and eventually expanded shape $\Omega(t_0+\Delta t)$ where the full multiscale dynamics is continued on the subsequent macro-micro stage $[t_0 + \Delta t, t_0 + 2\Delta t]$, as schematically illustrated in Figure 3.1.

3.5 Multiscale Numerical Simulation and Results

The computational approach developed in this work extends the multiscale numerical framework first introduced in Trucu et al. (2013) and later applied in Peng et al. (2017). The novel computational part of this study is the incorporation of the viral component into the macroscale part of the multiscale framework presented in Trucu et al. (2013). This combines a finite difference approach at macro-scale with a finite element method at micro-scale. While the finite difference approach at macro-scale involves central differences and midpoint approximations (as detailed in A.1), the finite element at micro-scale involves bilinear shape functions on a square mesh on each ϵY.

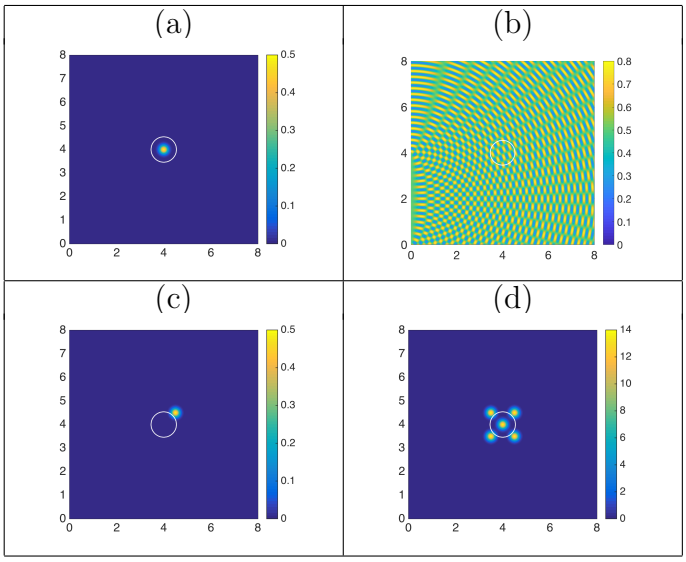

Figure 3.2: Initial Conditions: (a) uninfected cancer cells density; (b) ECM density; (c) OV density (one initial dose) and (d) OV density (five initial doses). The white line indicates the boundary of the total tumour cells (uninfected & infected densities).

In brief, we consider that the macro-scale dynamics of the progressing tumour $\Omega(t)$ takes place within a maximal tissue domain $Y = [0, 8] \times [0, 8]$, which we discretise by uniformly spatial mesh of a size $\Delta x = \Delta y = h = 0.03125$. We used a second order midpoint rule for approximating the diffusion and haptotactic terms (for both cancer cells) in all macro-dynamics modelling scenarios (3.10),(3.12),(3.14), as well as for the ECM-OV taxis term in (3.14), and we proceed with a trapezoidal predictor-corrector for time marching at macro-scale in all cases. The implicit trapezoidal corrector ensures the stability of the macroscopic discretisation. Further, the integral terms $f^{\epsilon Y}_{uPA}(\tau, y)$ and $f^{\epsilon Y}_{PAI-1}(\tau, y)$ (appearing within the *top-down macro-micro* link) contributing towards the sources and removal terms within the uPA System micro-dynamics (3.19)-(3.21) are calculated using direct formulas at overlapping macro-micro spatial nodes and via interpolation involving barycentric coordinates at all other off-*macro grid* micro-spatial points $y \in \epsilon Y$. Finally, in the presence of these terms induced from the macroscale, the micro-dynamics is solved via finite el-

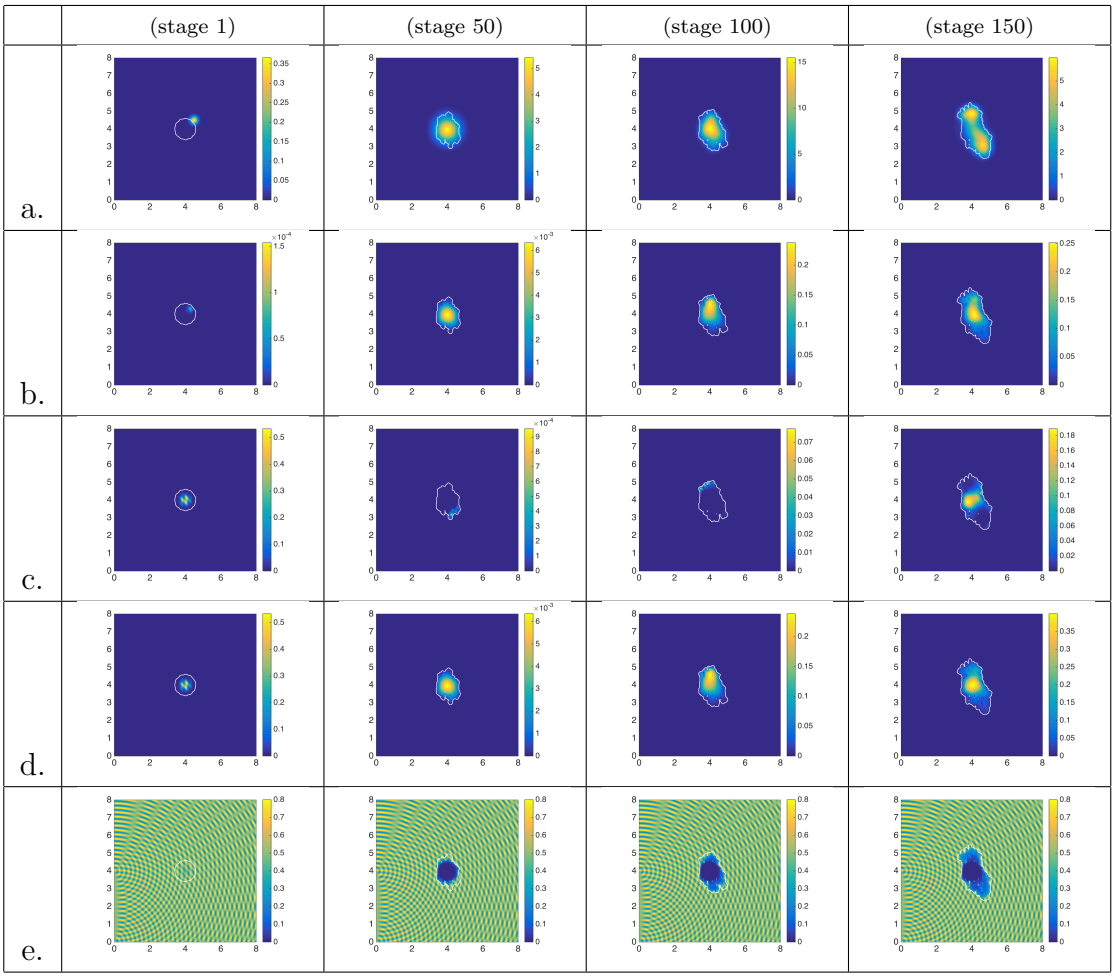

Figure 3.3: Multi-scale simulation results for macro-dynamics scenario (3.10) at four macro-micro stages (1,50,100, and 150) for the baseline parameter values from Table 3.1, showing: a. virus density; b. infected cancer cells density; c. uninfected cancer cells density; (d) total cancer cells density; and e. ECM density.

ement with bilinear shape functions on a square mesh with trapezoidal corrector for time marching. The direction and displacement magnitude obtained in each boundary micro-domain $\epsilon Y \in \mathcal{P}(t_0)$ in conjunction with the extent of ECM degradation determine the movement of the tumour boundary at macro-scale, which is recorded on the macro-scale uniform grid where the dynamics is then continued for the next time interval $[t_0 + \Delta t, t_0 + 2\Delta t]$ with the next macro-micro stage. This numerical approach was implemented by ourselves, as detailed in Trucu et al. (2013).

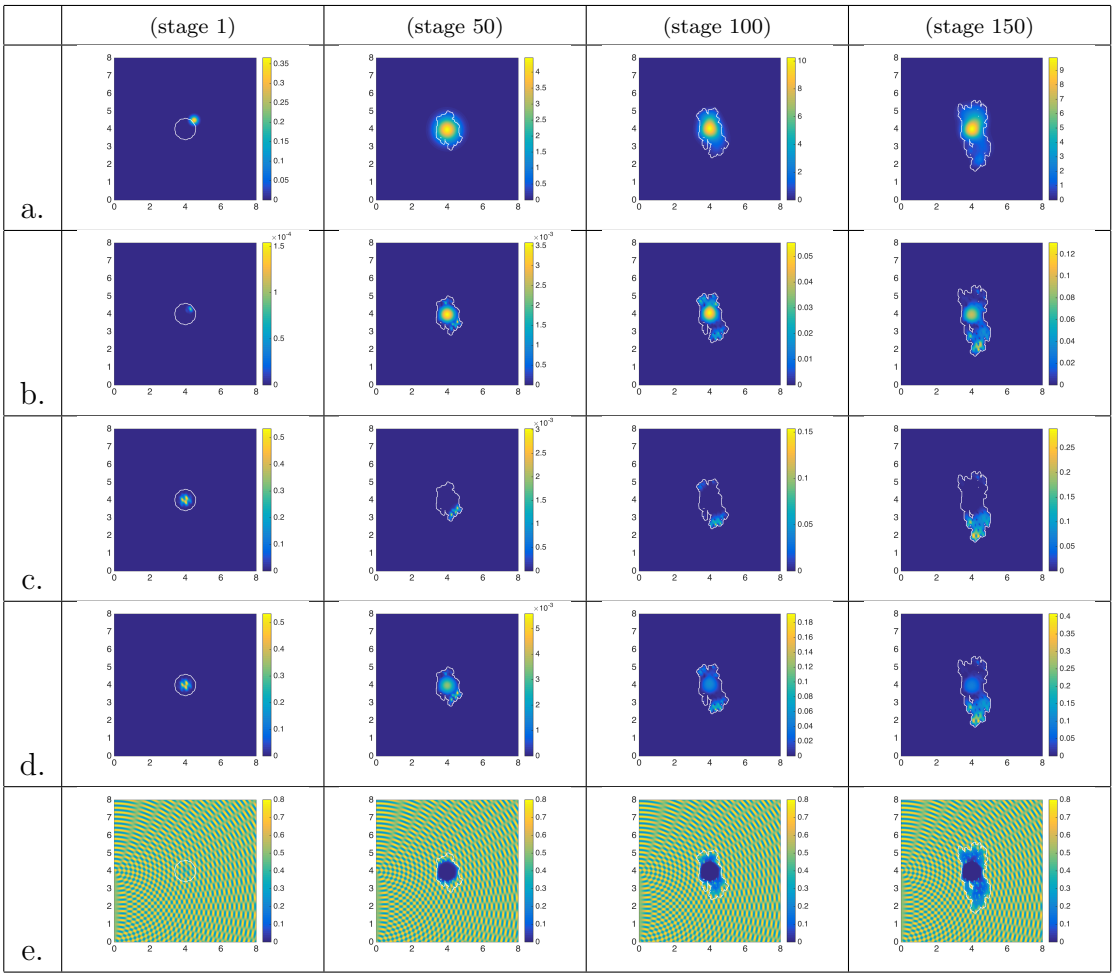

Figure 3.4: Multi-scale simulation results for macro-dynamics scenario (3.12) at four macro-micro stages (1,50,100, and 150) for the baseline parameter values from Table 3.1, showing: a. virus density; b. infected cancer cells density; c. uninfected cancer cells density; d. total cancer cells density; and e. ECM density.

3.5.1 Macro-dynamics initial conditions.

The multiscale dynamics is started with the following initial conditions on Y for each of the three macro-scale scenarios, namely:

- *uninfected cancer initial conditions:*

$$c(x,0) = \frac{\left(exp(-\frac{\|x-(4,4)\|_2^2}{\sqrt{\Delta x \Delta y}}) - exp(-28.125)\right)\theta_1(x)}{2},$$

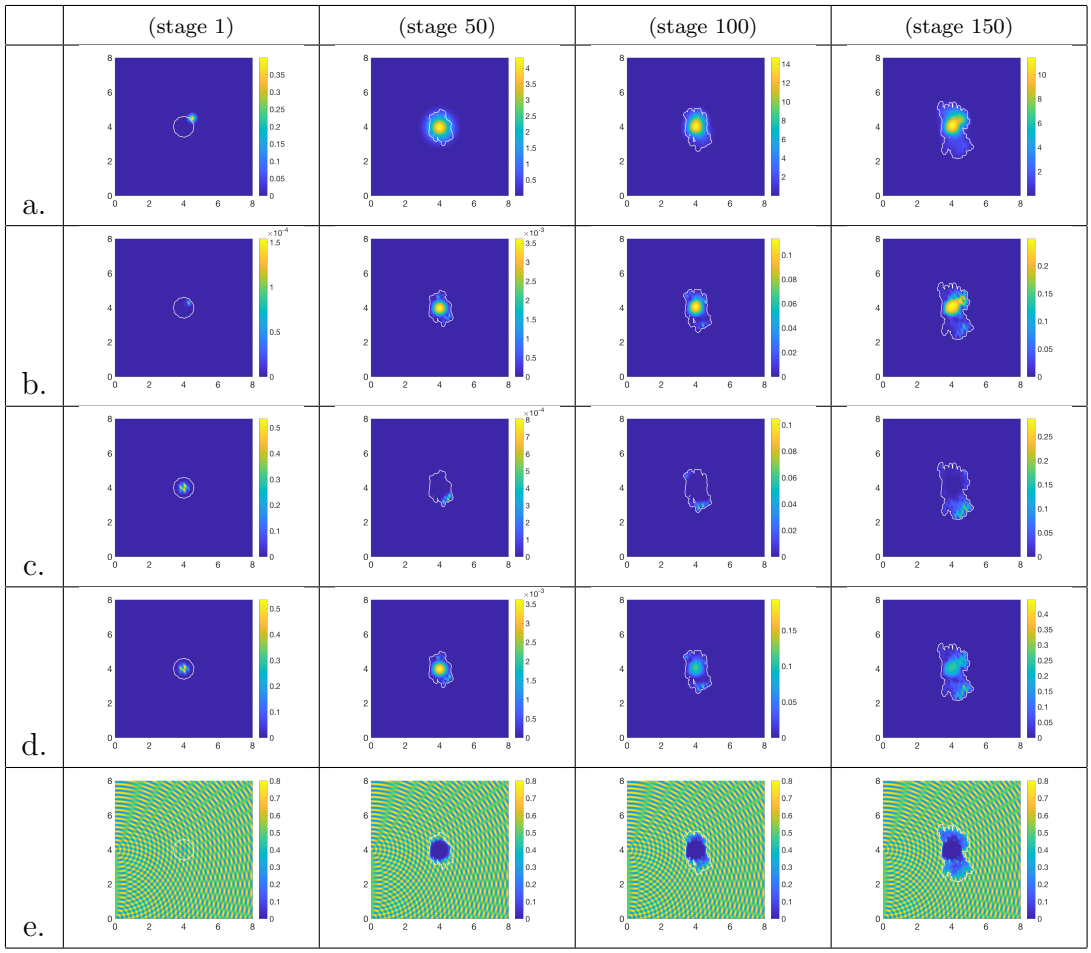

Figure 3.5: Multi-scale simulation results for macro-dynamics scenario (3.14) at four macro-micro stages (1,50,100, and 150) for the baseline parameter values from Table 3.1, showing: a. virus density; b. infected cancer cells density; c. uninfected cancer cells density; d. total cancer cells density; and e. ECM density.

where $\theta_1(x) := \chi_{B((4,4),0.5-\gamma)} * \psi_\gamma$, with the molifiler ψ_γ enabling a smooth transition to zero after 0.5 radius, as shown Fig. 3.2(a).

- *infected cancer initial conditions:*

$$i(x,0) = 0.$$

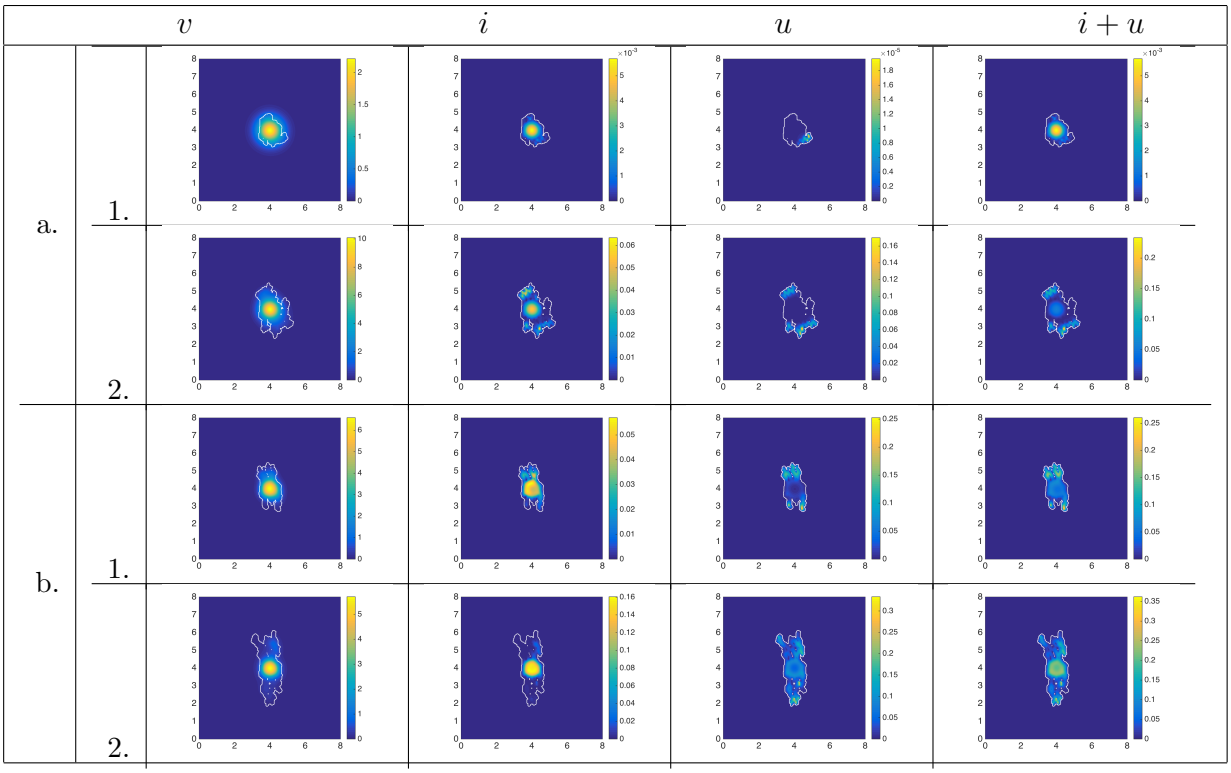

Figure 3.6: Multi-scale simulation results for macro-dynamics scenario (3.12), showing two variations of the baseline infected cancer cells death rate δ_i (namely: a. $\frac{\delta_i}{4}$; and b. $4\delta_i$) at macro-micro stages: 1. stage 75; and 2. stage 150.

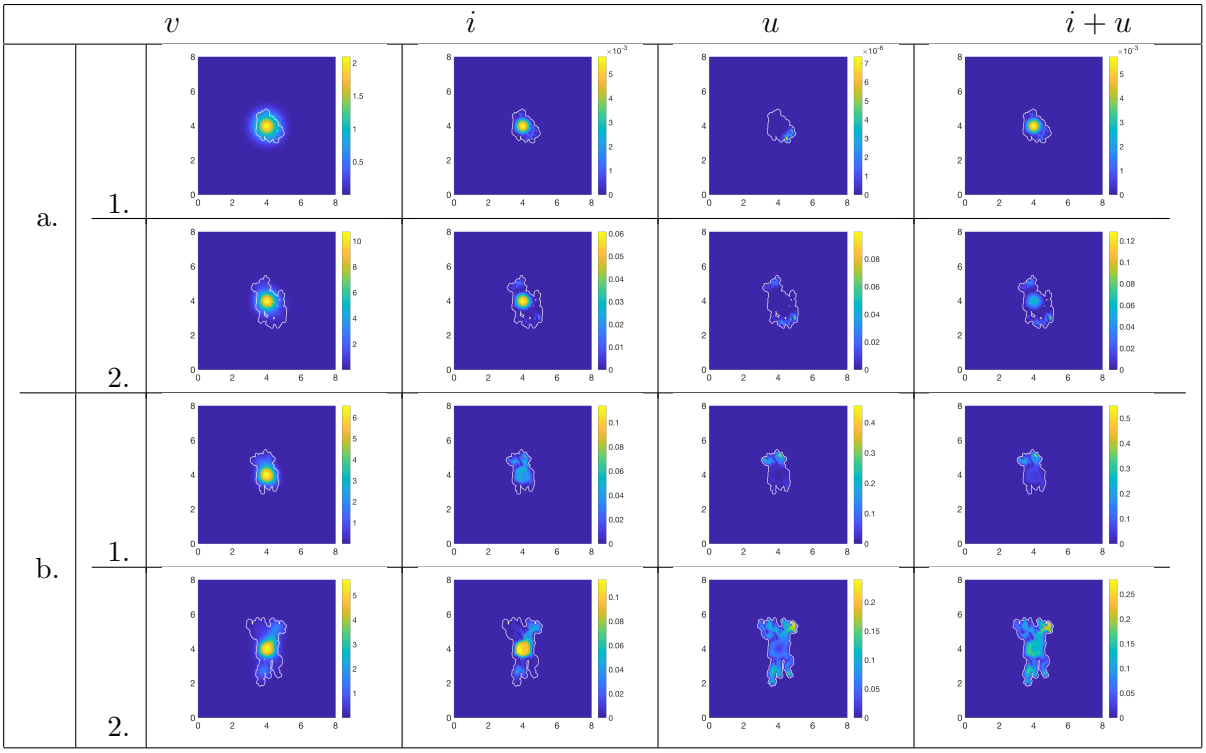

Figure 3.7: Multi-scale simulation results for macro-dynamics scenario (3.14), showing two variations of the baseline infected cancer cells death rate δ_i (namely: a. $\frac{\delta_i}{4}$; and b. $4\delta_i$) at macro-micro stages: 1. stage 75; and 2. stage 150.

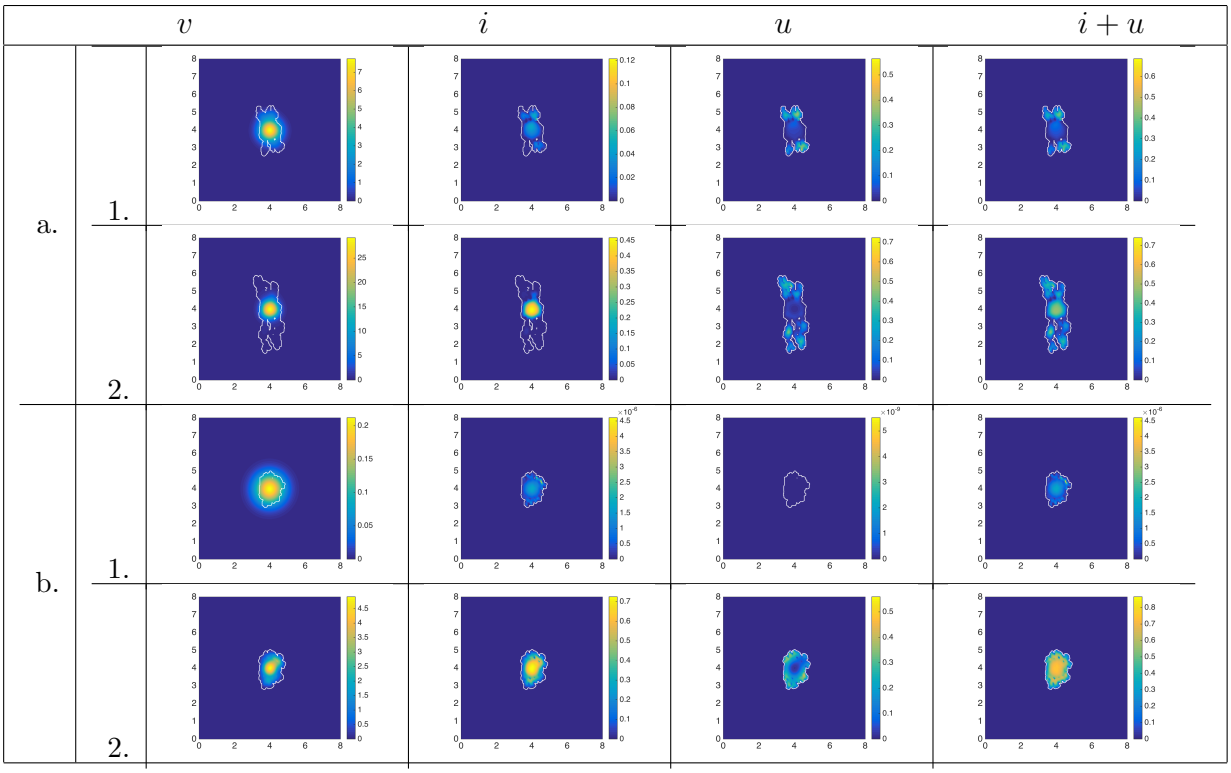

Figure 3.8: Multi-scale simulation results for macro-dynamics scenario (3.12), showing two variations of the baseline viral infection rate ρ (namely: a. $\frac{\rho}{5}$; and b. 5ρ) at macro-micro stages: 1. stage 75; and 2. stage 150.

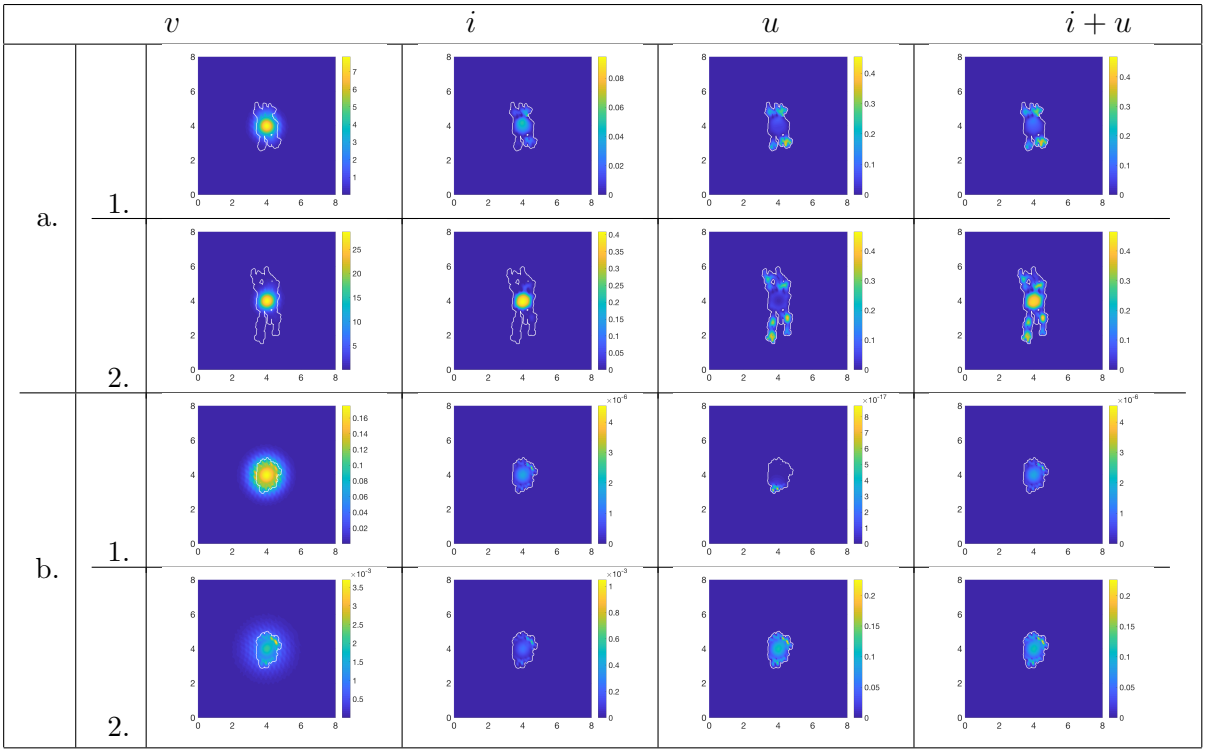

Figure 3.9: Multi-scale simulation results for macro-dynamics scenario (3.14), showing two variations of the baseline viral infection rate ρ (namely: a. $\frac{\rho}{5}$; and b. 5ρ) at macro-micro stages: 1. stage 75; and 2. stage 150.

- *extracellular matrix initial conditions:*

$$u(x,0) = \frac{1 + 0.3sin(4\pi \left\|x\right\|_2) + sin(4\pi \left\|(4,0) - x\right\|_2)}{2}$$

  as shown in Fig. 3.2(b);

- *oncolytic virus initial conditions:*

$$v(x,0) = \frac{\left(exp(-\frac{\|x-(4.5,4.5)\|_2^2}{\sqrt{\Delta x \Delta y}}) - exp(-28.125)\right)\theta_2(x)}{2}$$

  where $\theta_2(x) := \chi_{B((4.5,4.5),0.5-\gamma)} * \psi_\gamma$, as shown in Fig. 3.2(c).

However, to explore the impact of multiple virus doses, for the results in Figure 3.13, we use the *initial condition with five doses of oncolytic virus* that is shown in Figure 3.2(d) and is give by

$$\begin{aligned} v(x,0) = & \\ & \sum_{i,j\in\{-1,1\}} 0.5\Big(exp(-\tfrac{\|x-(4+0.5i,4+0.5j)\|_2^2}{\sqrt{\Delta x \Delta y}}) - exp(-28.125)\Big)\theta_{i,j}(x) \\ & + 0.5\Big(exp(-\tfrac{\|x-(4,4)\|_2^2}{\sqrt{\Delta x \Delta y}}) - exp(-28.125)\Big)\,\theta_1(x), \end{aligned}$$

where we have that $\theta_{i,j}(x) := \chi_{B((4+0.5i,4+0.5j),0.5-\gamma)} * \psi_\gamma$, $\forall i,j \in \{-1,1\}$.

Remark: The specific initial conditions for the oncolytic virus were chosen to simulate the effect of injecting the virus particles inside the tumour or at tumour boundary. Such approaches are often considered in experimental settings Nagano et al. (2008); Lu et al. (2004).

3.5.2 Summary of model parameters

In Table 3.1, we summarise the baseline parameter values for the most complex macro-dynamics model (3.14) (these parameters appear also in models (3.10) and (3.12)). The majority of these parameter values are taken from two references, Camara et al. (2013) and Peng et al. (2017). The parameter estimation in Camara et al. (2013) is based on the dynamics of glioma cancer cells in the presence of OV where it is mainly estimated from the available pre-treatment MRIs data (magnetic resonance images) as given in Harpold et al. (2007), while the modelling approach in Peng et al. (2017) describes the cancer invasion process in the presence of ECM degradation enzymes. Hence, our baseline parameter regime is built on the parameters validation and limitation as discussed in these two studies.

Parameter	Value	References
D_c	0.00675	Camara et al. (2013)
D_i	0.0054	Camara et al. (2013)
D_v	0.0036	Camara et al. (2013)
η_c	2.85×10^{-2}	Peng et al. (2017)
η_i	2.85×10^{-2}	Peng et al. (2017)
η_v	2.85×10^{-3}	Estimated
μ_1	0.25	Peng et al. (2017)
ρ	79×10^{-3}	Camara et al. (2013)
δ_i	0.05	Camara et al. (2013)
α_c	0.15	Estimated
α_i	0.075	$\frac{\alpha_c}{2}$
μ_2	0.015	Estimated
b	2	Estimated
δ_v	0.025	Camara et al. (2013)
β	0.775	Peng et al. (2017)
λ_c	0.8	Estimated
λ_i	0.4	Estimated

Table 3.1: Baseline parameters values for the macroscopic models (3.10), (3.12) and (3.14). The last three parameters, β, λ_c and λ_i are involved in the macro-micro connection; see also equations (3.16) and (3.24).

In Table 3.2, we summarise the values of parameters ρ, δ_i, α_c, α_i and b (for

the macro-dynamics scenarios,(3.12) and (3.14)), that have shown to lead to best tumour suppression results.

Parameter	Value
D_c	0.00675
D_i	0.0054
D_v	0.0036
η_c	2.85×10^{-2}
η_i	2.85×10^{-2}
η_v	2.85×10^{-3}
μ_1	0.25
ρ	395×10^{-3}
δ_i	0.0125
α_c	0.3
α_i	0.15
μ_2	0.015
b	3
δ_v	0.025
β	0.775
λ_c	0.8
λ_i	0.4

Table 3.2: Summary of parameter values that have shown improved tumour suppression results, as summarised in Figures 3.14 and 3.15.

In Table 3.3, we summarise the parameters values for the micro-dynamics (3.19)-(3.21).

3.5.3 Multi-scale numerical results for the three macro-scale scenarios

In this section, we investigate numerically the three macroscale scenarios introduced previously. We aim to observe the cancer response to oncolytic viral therapy via tracking the macro-micro model behaviour on the maximal tissue domain Y with respect to several aspects such as: cancer cells density, cancer boundary expansion, or cancer suppression.

Parameter	Value
D_a	2.5×10^{-3}
D_p	3.5×10^{-3}
D_m	4.91×10^{-3}
ψ_{11}	0.75
ψ_{12}	0.215
ψ_{13}	0.3
ψ_{21}	0.75
ψ_{22}	0.55
ψ_{23}	0.5
ψ_{31}	0.11
ψ_{32}	0.75
ψ_{33}	0.5

Table 3.3: Summary of parameter values for the microscopic modelling component. All parameters for this system are taken from the reference Peng et al. (2017).

For the numerical investigation of these three macroscale scenarios (3.10), (3.12), and (3.14), we first choose a list of baseline parameters (mainly based on the published studies in Camara et al. (2013); Peng et al. (2017)), and investigate the outcome of the assumptions incorporated in these three cases. Second, we investigate the effect of changing some of the parameters involved in virus dynamics and spread: the death rate of infected cancer cells (δ_i), the viral infection rate (ρ), the ECM degradation rates by uninfected cancer cells (α_c) and infected cancer cells (α_i), the virus replication rate (b), and the initial administered virus dose. Finally, based on the outcome of these results with different parameter values, we discuss the conditions that lead to improved tumour suppression.

Baseline Results The following simulation results are obtained with the baseline parameter values listed in Tables 3.1 (for the macroscopic component) and 3.3 (for the microscopic component). In all figures shown below, the white curve represents the boundary of the total tumour (i.e., uninfected and infected cells) within the maximal tissue domain Y.

In Figures 3.3, 3.4 and 3.5 we present the multiscale simulations for the coupled dynamics of uninfected cancer cells (sub-panels *c.*), OV-infected cancer cells (row *b.*), extracellular matrix (ECM) (row *e.*) and oncolytic viruses (row *a.*), for the three macro-dynamics scenarios described by (3.10), (3.12) and (3.14), respectively. We also show (row *d.*) the total cancer cell density (i.e., uninfected plus infected cells). For all simulations, we start with the uninfected cancer cells density as shown in Figure3.2(a), and the virus density as shown in Figure 3.2(c) (where the virus is initially located on the tumour edge $\partial\Omega(t)$, namely at $(x, y) = (4.5, 4.5)$). The columns show the macroscopic evolution of the tumour-ECM-virus system at four different stages of the macro-micro interactions: stages 1, 50, 100 and 150.

We observe that in the absence of haptotatic migration against ECM gradients for both infected cells and viruses (as described by macro-dynamics scenario (3.10)), the virus infects mainly the areas of the tumour with lower cell densities (see stage 150 in Figures 3.3a. and 3.3c.)

If we consider haptotactic migration of virus-infected tumour cells against the ECM gradients (as described by macro-dynamics scenario (3.12)), we observe a large reduction in tumour size where the virus is located (see stage 150 in Figures 3.4a. and 3.4c.).

Finally, if we consider the haptotactic migration of both virus-infected cells and virus particles towards ECM gradients (as described by macro-dynamics scenario (3.14)), we observe an even better reduction in tumour size which is the result of a better virus spread throughout the tumour (see stage 150 in Figures 3.5a. and 3.5c.).

The baseline tumour mass evolution across all macro-micro stages (1–150) for macro-dynamics scenarios (3.12) and (3.14) are shown in Figure 3.15 with blue dotted lines and compared agains five relevant cases of parameter variation, as detailed

in the next paragraphs.

In the following, we focus on the last two macro-dynamics scenarios, (3.12) and (3.14), and investigate the effect of changes in various model parameters related to virus dynamics and spread (parameters which can be varied experimentally to impact virus kinetics Maroun et al. (2017)). For conciseness, Figures 3.6-3.13 below will show the results obtained only at macro-micro stages 75 and 150 of the multiscale dynamics.

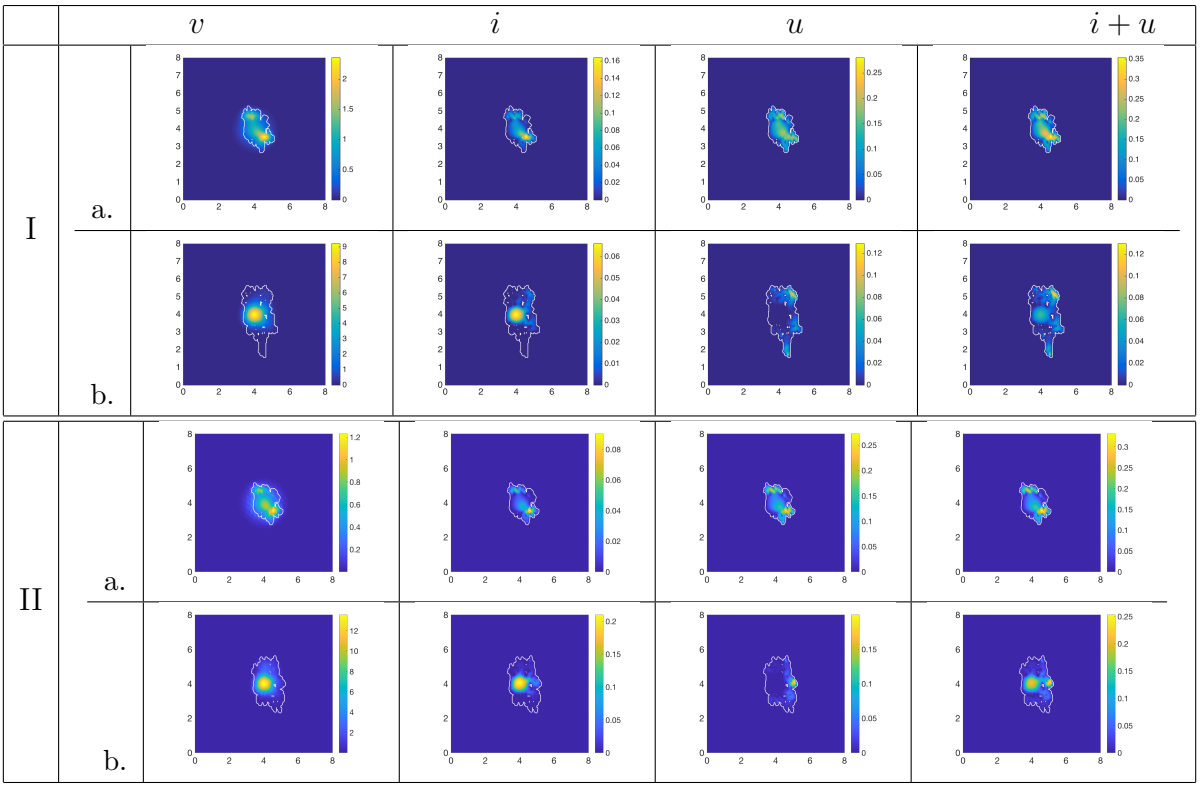

Figure 3.10: Multi-scale simulation results for ECM degradation rates $\alpha_c = 0.3$ and $\alpha_i = 0.15$ for macro-dynamics scenarios(3.12) (in panel I) and (3.14) (in panel II) at two macro-micro stages: a. stage 75; and b. stage 150.

Infected Cells' Death Rate We start our investigation into the effects of different model parameters on treatment outcomes, by focusing first on the rate δ_i at which the infected cells are eliminated from the system (by the anti-viral immune

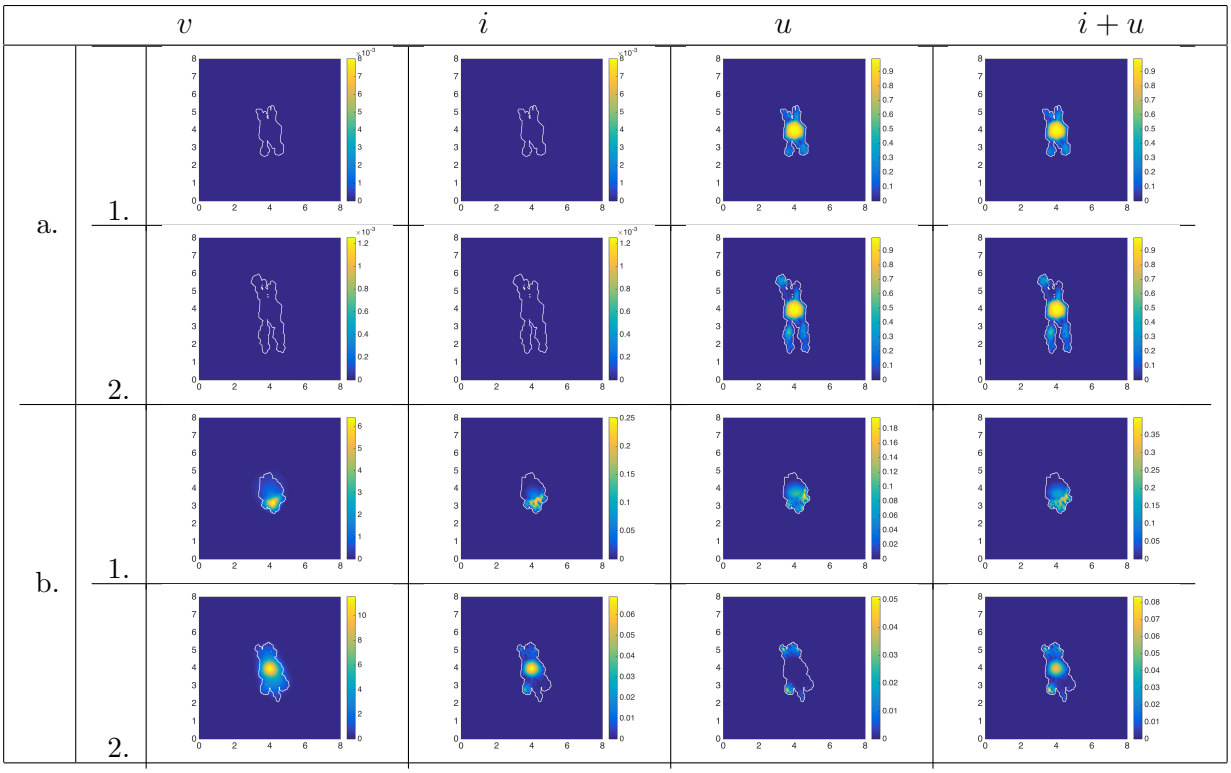

Figure 3.11: Multi-scale simulation results for macro-dynamics scenario (3.12), showing two variations of baseline OV replication rate b (namely: a. $b = 0$; and b. $b = 3$) at macro-micro stages: 1. stage 75; and 2. stage 150.

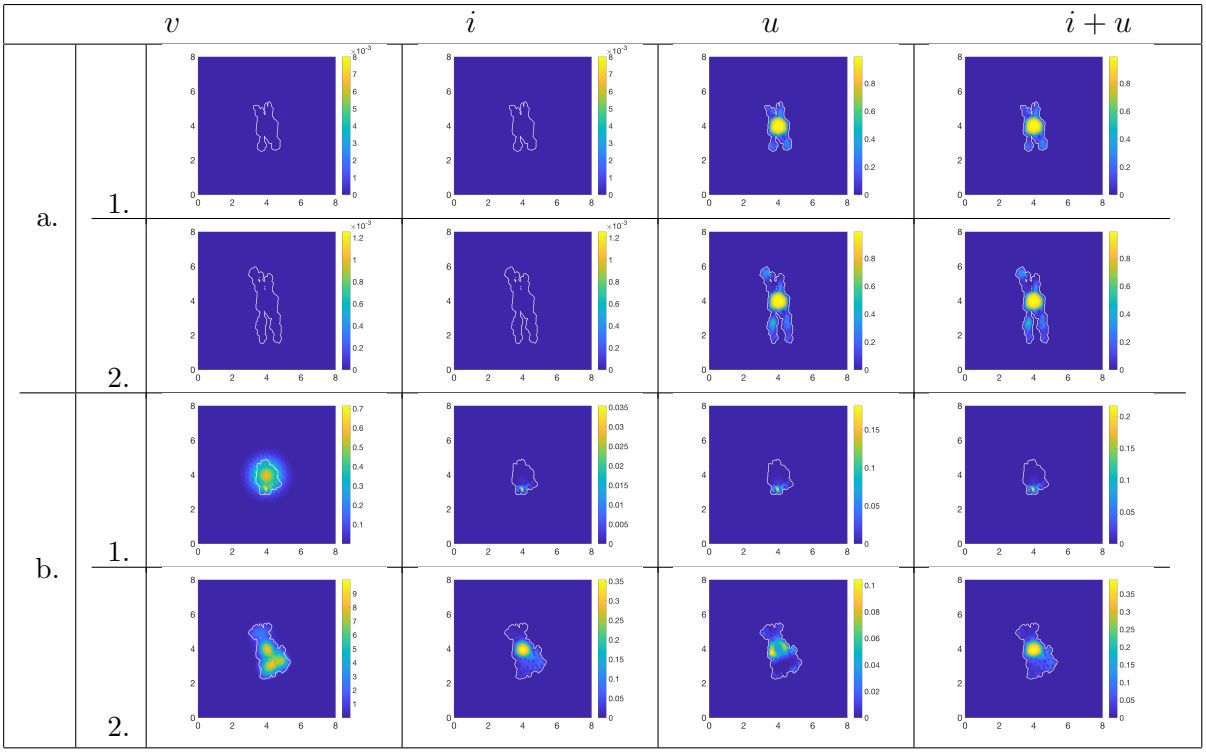

Figure 3.12: Multi-scale simulation results for macro-dynamics scenario (3.14), showing two variations of baseline OV replication rate b (namely: a. $b = 0$; and b. $b = 3$) at macro-micro stages: 1. stage 75; and 2. stage 150.

response Filley and Dey (2017)). As mentioned before, we discuss the impact of this rate on macro-dynamics scenarios (3.12) and (3.14). In Figures 3.6 and 3.7 we reduce δ_i by a factor of four (i.e., to $\delta_i/4$), and we observe that the uninfected tumour cells are reduced dramatically in those areas occupied also by the oncolytic virus. This result makes sense, since the persistence of infected tumour cells gives rise to more virus particles replicating inside these cells. On the other hand, increasing δ_i by a factor of four (i.e., to $4\delta_i$) leads to a poorer elimination of tumour cells, as observed in panel (b) of Figures 3.6 and 3.7. However, as shown in Figure 3.15(1), beyond the overall tumour mass being kept under control, δ_i alone does not bring a clear influence towards suppressing the tumour, as tumour relapses to levels above the baseline occur both when we lower and when we increase the cell death rate.

Infection Rate of Tumour Cells In the following, we examine the effect of viral infection rate (ρ) on tumour dynamics. Experimental studies have shown that increasing the rate at which the oncolytic virus infects the tumour cells (e.g., by engineering the virus particles to encode specific proteins that could temporarily suppress anti-viral immune responses) plays a key role in the development of new anti-cancer therapies Maroun et al. (2017). To investigate this aspect, we performed various simulation tests for the macroscopic models (3.12) and (3.14), as we decreased and increased the baseline value $\rho = 79 \times 10^{-3}$ by a factor of five (to $\frac{\rho}{5}$ and 5ρ, respectively). From panel (a.) of Figures 3.8 and 3.9, we observe that a five-fold decrease in the infection rate ρ leads to a much faster spread of the tumour cells (as described by the expanding tumour boundary), compared to the case where the infection rate is increased five fold - as shown in panel (b.) of Figures 3.8 and 3.9. As shown in Figure 3.15(2)(II) with green dotted line, the five fold increase in ρ leads to significantly better global tumour suppression with respect to the baseline or five fold decreased cases within the macro-dynamics scenario (3.14). A similar

although weaker tumour suppression effect observed for macro-dynamics scenario (3.12), where a relapse occurs over the final stages of the time interval, as shown by Figure 3.15(2)(I).

ECM Degradation Rates Known to be crucial within the process of cancer cells' invasion of the surrounding tissue Hanahan and Weinberg (2000, 2011), the ECM is expected to play also an important role in viral therapy. Indeed, the ECM distribution within the growing tumour $\Omega(t)$ interfere with the oncolytic virus dynamics, having impeding effects upon its spread, restricting the viral duplication, and lowering the effectiveness of cytolytic. However, the degradation for the ECM provides opportunities for potentially raising the effectiveness of OV treatments by facilitating a less demanding virus passage within the tumour tissue, gaining an easier access to uninfected cancer cells sites (Kim et al., 2014). Thus, the success or failure of the oncolytic virus distribution will depend on the ECM degradation, and this is confirmed also by our results obtained by doubling the degradation rate (with respect to the baseline) and shown in panels Ia.–b. and IIa.–b. of Figure 3.10 for the macro-dynamics (3.12) and (3.14), respectively.

As illustrated in Figure 3.10 an increase in degradation rate causes not only changes in the morphology of the growing tumour, but also a decay in the tumour mass, as reflected in Figure 3.15(3). This decay in the total tumour mass for the macro-dynamics scenario (3.12) is the effect of the following interacting dynamics. The increased ECM degradation causes both infected cancer and uninfected cancer cells to bias their migration haptotacticly towards the emerging regions of elevated ECM levels, enabling this way a local congregation of the two cancer cell subpopulations (infected and uninfected), which mediates in its turn a higher degree of infection spread among the uninfected cancer cells, resulting this way in a decrease in tumour mass. However, as by comparing panels Ia.–b. with IIa.–b. in Figure 3.10,

the total cell population exhibits slightly limited spread with no pronounced fingering in the macro-dynamics scenario (3.14) as opposed to macro-dynamics scenario (3.12) where the tumour develops large fingering growth. This particular behaviour within macro-dynamics (3.14) is due to the biased migration of both the infected and uninfected cancer cells as well as of the oncolytic virus against ECM gradients, this enabling them to congregate within the same regions, leading this way to increased levels of local tumour decay.

Viruses Replication Rate Another factor that impacts virus kinetics is its replication rate (i.e., the number of virus particles release by an infected tumour cell) Maroun et al. (2017). It is expected that an increase in the virus replication rate will lead to a decrease in the tumour size. We confirm this through the results shown in panel (b.) of Figures 3.11 and 3.12 for macro-dynamics scenarios (3.12) and (3.14), respectively, where we considered a higher virus replication rate (namely $b = 3$) than the corresponding baseline value (from Table 3.1) used in Figures 3.4 and 3.5 (namely $b = 2$). This overall tumour decrease is also confirmed by the tumour mass estimate, represented in Figure 3.15 (4) through the green dotted line, which shows that, at all macro-micro stages (1-150), the tumour mass for the increased virus replication rate b is below the corresponding baseline scenario.

Finally, the absence of viral replication (i.e., $b = 0$), explored here through our multiscale approach in panel (a.) of Figures 3.11 and 3.12 for macro-dynamics scenarios (3.12) and (3.14), leads to an increase in spatial spread of the tumour, giving rise to pronounced fingering and elongated tumour infiltrations in the surrounding tissue. Moreover, Figure 3.15 (4) shows that the tumour mass in the absence of virus replication (in red dotted line) stays above the baseline results and continues to increase at all macro-micro stages (1-150).

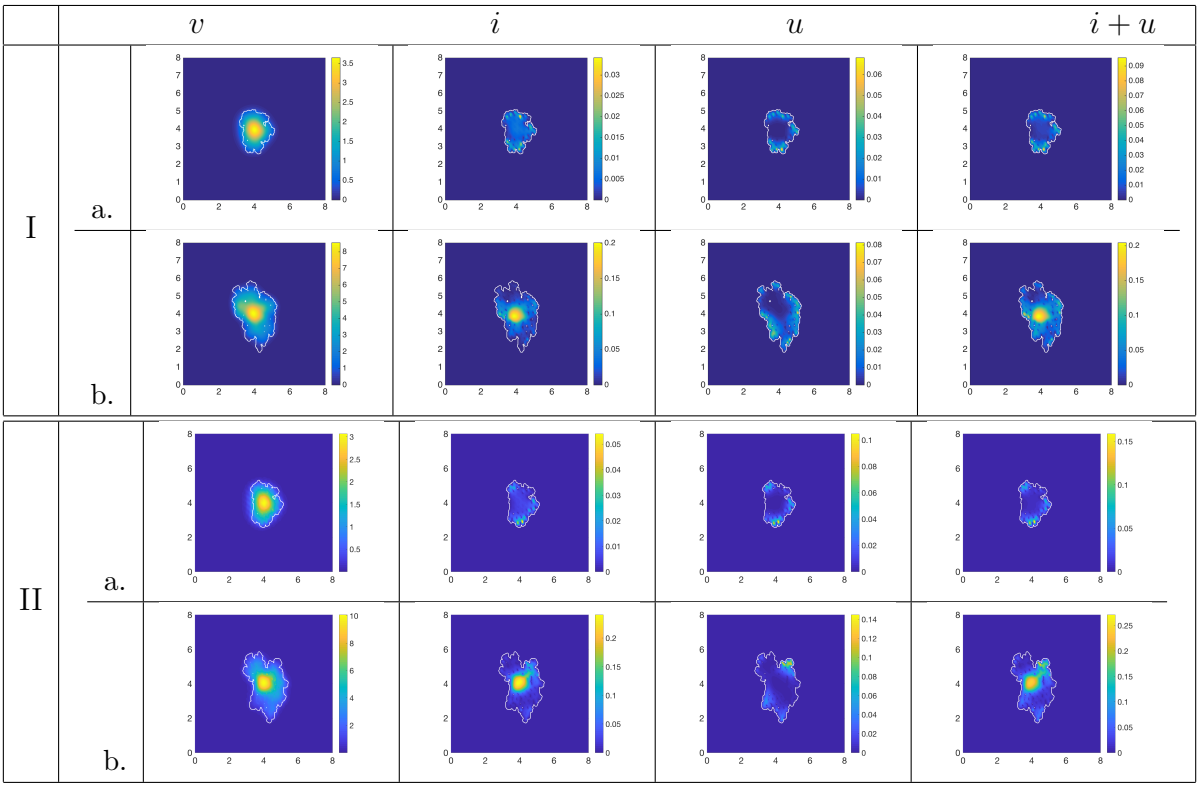

Figure 3.13: Multi-scale simulation results for five virus initial doses for macro-dynamics scenarios (3.12) (in panel I) and (3.14) (in panel II) at two macro-micro stages: a. stage 75; and b. stage 150.

Viruses Doses Acknowledging the therapeutic importance of virus dosage Rommelfanger et al. (2011) and accounting in this regard on a series of biological constraints reviewed in Vähä-koskela and Hinkkanen (2014), the virus doses should be balanced in size and, for a more efficient viral therapy, these need to be higher than the initial tumour size Bajzer et al. (2008). Moreover, the location of the virus doses is important for the spatio-temporal viral dynamics within the growing tumour $\Omega(t)$ Rioja et al. (2016), as their distribution in the immediate proximity of high density tumour regions have the potential of a faster viral infection and spread within $\Omega(t)$. These biological observations are explored also by our results in Figure 3.13, where we investigate the effect of spatial distribution of initial viral dosage by increasing their number to 5 identical doses that were spatially applied as shown by Figure

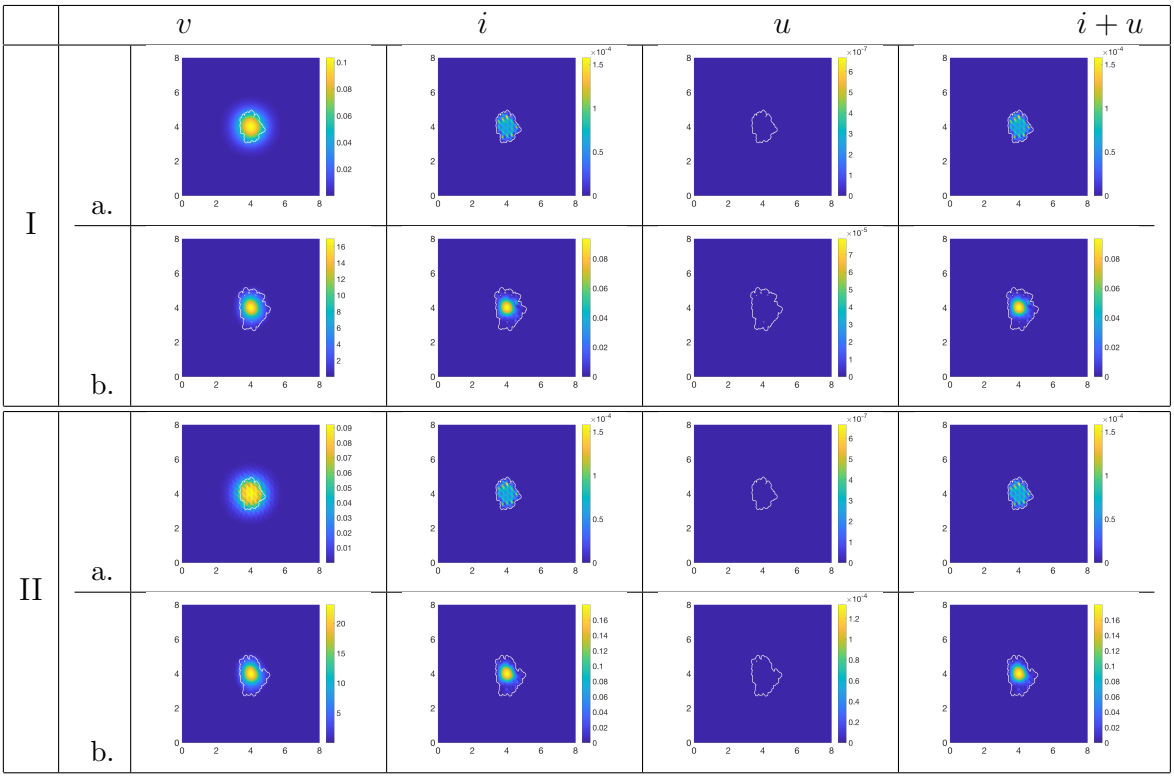

Figure 3.14: Multi-scale simulation results for the improved outline for tumour suppression for macro-dynamics scenarios (3.12) (in panel I) and (3.14) (in panel II) at two macro-micro stages: a. stage 75; and b. stage 150.

3.2(d). As indicated also in Figure 3.15(5), after an initial rapid decrease over the first 30 stages (not shown also in Figure 3.13), the tumour distribution recovers and exhibits a more compact growth. This leaves the virus dosage question open and raise the challenging problem of designing a more comprehensive strategy where new virus doses need to be applied in appropriate locations at later stages so that tumour control and elimination could be achieved.

Improved Viral Therapy Outline for Tumour Suppression Building on the tumour–OV interraction scenarios and their associated numerical results explored in Figures 3.4 – 3.13, an improved therapy is obtained by cumulating and using the parameter values identified there to give better tumour control and suppression

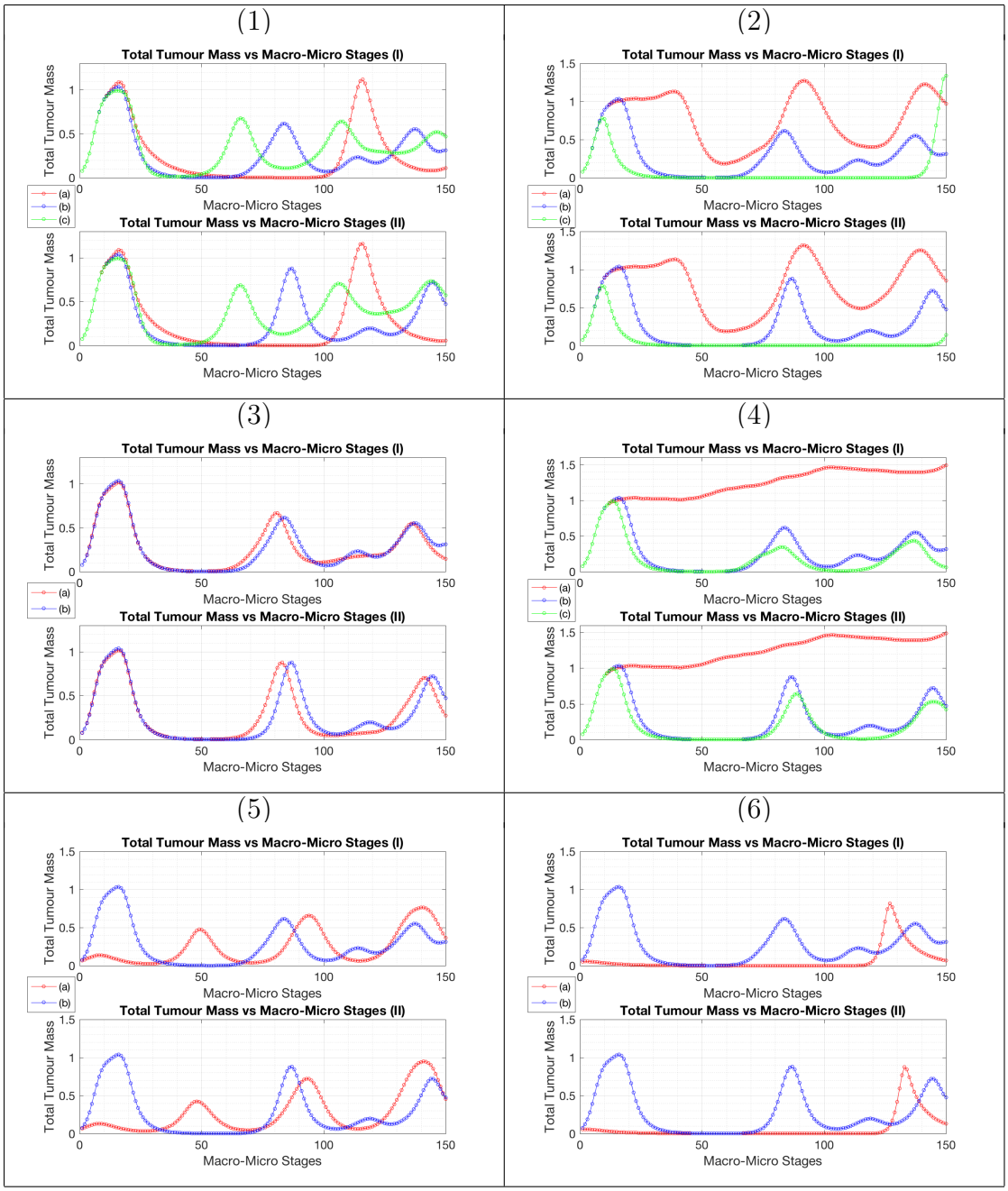

Figure 3.15: Comparison of total tumour masses evolution over macro-micro stages 1 – 150 between the macro-dynamics scenarios (3.12) (in subfigures (I)) and (3.14) (in subfigures (II)) for the following cases of parameter variations with respect to their baseline values given in Table 3.1, namely: (1) (a) $\frac{\delta_i}{4}$, (b) baseline value for δ_i, and (c) $4\delta_i$; (2) (a) $\frac{\rho}{5}$, (b) baseline value for ρ, and (c) 5ρ; (3) (a) $2\alpha_c$,$2\alpha_i$, and (b) baseline values for α_c and α_i; (4) (a) no OV replication, $b = 0$, (b) baseline value for b, and (c) b=3; (5) (a) five OV initial doses and (b) one OV initial dose; (6) (a) parameter for improved viral therapy outline for tumour suppression given in Table 3.3, and (b) baseline parameter values given in Table 3.1.

response. Summarised in Table 3.2, the changes in the parameters (with respect to their baseline values) considered in this improved therapy outline include: a four time decrease of the virus replication rate, a five fold increase in the infection rate of tumour cells, doubled ECM degradation rate, 50% increase in virus replication rate. Thus, in the presence of the five initial virus doses given in Figure 3.2(d), the results obtained via these outlined parameter changes, shown in Figure 3.14, present significant improvements in the tumour suppression results for macro-dynamics scenarios (3.12) and (3.14), both in terms of tumour levels and in spatial spread. The level of uninfected cells drops dramatically and the overall tumour remain fairly compact, presenting only a limited growth over the spatial domain, throughout the entire observation period. The tumour mass evolution plotted there with red dotted line in Figure 3.15(6) shows a complete control of the tumour which, besides a local-in-time relapse, is brought to residual total mass levels in both macro-dynamics scenarios (3.12) and (3.14), over the 150 macro-micro stages. Furthermore, by exploring this improved outline for the tumour – OV interaction on a longer time perspective of 350 macro-micro stages, as shown in Figure 3.16(I) we obtain the a good long term control of the tumour, this presenting a limited spatial growth (figure not shown here) and its overall mass being brought to residual levels in both macro-dynamics scenarios (3.12) and (3.14).

3.6 Conclusions and Discussions

In this paper we proposed a novel multi-scale moving boundary framework to describe the complex interactions between the tissue-scale (macro-scale) cancer cells (uninfected and infected) populations, ECM, oncolytic virus, in the presence of the cell-scale tumour invasive edge uPA microdynamics. The macro-dynamic of tumour–oncolytic virus interaction give rise to the source for the leading uPA micro-dynamics

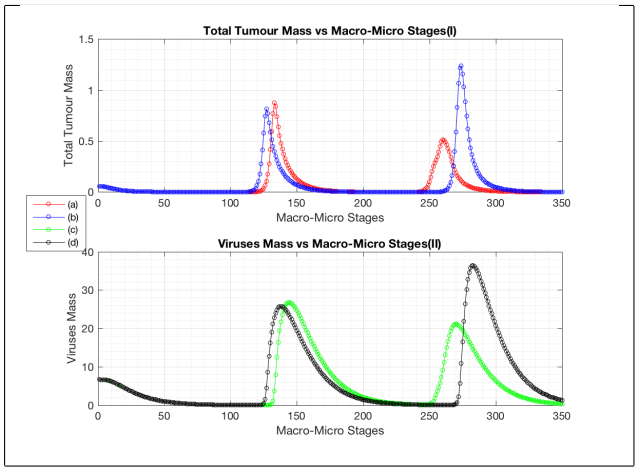

Figure 3.16: A long run (350 macro-micro stages) of the improved outline for tumour suppression case . (I) A comparison of total tumour masses between macro-dynamics modelling scenarios: (a) (3.14) and (b) (3.12). (II) A comparison of viruses masses between macro-dynamics modelling scenarios: (c) (3.14) and (d) (3.12).

via a nonlocal operator, this way establishing a top-down link between tissue- and cell- scale levels of activity of this naturally multiscale process.

In the presence of the source induced from the macro-scale, the uPA exercises a cross-interface micro-transport on a cell-scale neighbourhood of the tumour boundary $\partial\Omega(t)$ that is given by the union of a bundle of *"half-way" overlapping* micro-domains $\{\epsilon Y\}_{\epsilon Y\in\mathcal{P}(t)}$. This bundle of *"half-way" overlapping* micro-domains enabled the decoupling of the micro-dynamics in terms of the dynamics on each micro-domain $\epsilon Y \in \mathcal{P}(t)$. On each micro-domain ϵY, the significant levels of proteolytic transport in the peritumoural regions enabled us the determine the patterns of significant degradation of the ECM that the uPA meets and interacts with on $\epsilon Y \setminus \Omega(t)$. The spatial distribution of this significant level of proteolytic enzymes enable us to characterise the choreographic direction of movement and displacement magnitude of the interface $\partial\Omega(t) \cap \epsilon Y$ and to represented this back at macro-scale in the form of a macro-scale tumour boundary velocity. This macro-scale tumour boundary velocity determined at micro-scale establishes a *bottom-up* feedback that is crucial in

deciphering the morphological evolution of the macro-scale tumour.

At macro-scale we considered a cascade of three scenarios for tumour–OV interaction, summarised in (3.10),(3.12) and (3.14), in which taxis towards ECM gradients is gradually introduced for uninfected cancer cells, infected cancer cells, and oncolytic virus, respectively.

Indeed, per unit time, the first macro-scale scenario given in (3.10) accounts for the random motility of the uninfected cells, uninfected cells and virus particle within the surrounding ECM in the presence of the usual processes of virus infection, virus replication, ECM degradation, uninfected cell-proliferation and infected cell death, while considering taxis against ECM gradients (haptotaxis) only for the uninfected cell population. The modelling context is then extended to the macro-dynamics scenario (3.12) when haptotaxis is also considered for the infected cell population, and finally this is completed with macro-scale scenario (3.14) when also the implicit ECM taxis movement of the virus is accounted for in the form of an ECM-OV taxis term.

As an initially considered baseline parameter values set (given in Table 3.1) for all three macro-dynamics scenarios ((3.10), (3.12) and (3.14)) did not ensure an effective tumour suppression (as seen in Figures 3.3–3.5), we explored further the tumour–OV interaction conditions for the macro-dynamics scenarios (3.12) and (3.14) by varying the infected cancer cells death rate, the viral infection speed, the ECM degradation rates, viral replication rate, as well as the spatial distribution of initial virus doses. In doing so, we identified not only successful therapeutical cases, but also situations where the oncolytic viral therapy failed to lead to tumour suppression. As reflected by Figure 3.15, the failure of viral threatment could be clearly identified in two cases, namely: (1) slowing down viral infection speed (as shown in panel (a.) of Figures (3.8) and (3.9) and Figure 3.15(2)); and (2) the absence of viral replication

induced by infected cancer cells (as shown in panel (a.) of Figures 3.11 and 3.12 and Figure 3.15(4)). Whether facing a slowdown of the infection rate or being in the absence of viral replication, the uninfected tumour cells gain momentum and become the dominant player, proliferating and driving the spatial invasion, enhancing the overall tumour mass and giving rise to pronounced fingering patterns.

However, improved tumour suppression scenarios were found for the following parameter changes with respect to their baseline vales, namely for: (a) reducing the infected cell death rate (shown in Figures 3.6 and 3.7); (b) increased viral infection rate (shown in Figures 3.8 and (3.9)); (c) increased ECM degradation rate (shown in Figure 3.10); (d) increased viral replication rate (shown in Figures 3.11 and 3.12). Alongside these parameter changes, a spatial redistribution of initial virus dosage in the proximity of tumour was found to have benefic impact upon tumour mass control and spatial spread.

Finally, a combination of best parameters that we found for tumour suppression led to an even better control of the tumour mass and tumour spatial spread as shown in Figures 3.14 and 3.15(6). Here the distribution of uninfected cancer cells is kept for most time observed at very low levels and the spatial spread is compact and very limited for both macro-dynamics scenarios considered, (3.12) and (3.14). An even longer observation of time, showed here in Figure 3.16 revealed that despite two instances of tumour relapses (captured by the only two peaks in tumour masses Figure 3.16) the tumour growth is suppressed and the tumour itself is kept under control. Note that Fig. 3.15 and 3.16 show quite similar overall tumour mass dynamics, which is expected since the difference between scenarios (3.12) and (3.14) is in the advection of virus and does not affect the total tumour mass (because the rates at which the virus kills the tumour are the same for the two scenarios). Thus, while tumour control could be in principle achieved, a complete tumour elimination

that would not present relapses opens the challenging question of designing a optimal strategy for iterative delivery of new tumour doses at appropriate spatial locations, this being the topic of a future work. Furthermore, the baseline estimation of the parameter values ensures an appropriate fit in a comparison with some biological and mathematical observations (Bajzer et al., 2008; Vähä-koskela and Hinkkanen, 2014; Maroun et al., 2017; Kim et al., 2014), hence, our numerical results give a general guidance for increasing the level of parameters validation in terms of getting better predictions in a comparison with *in vitro* or *in vivo* experiments for oncolytic viral therapy for cancer treatment (see, for instance, the spatial data from Kemler et al. (2019) on oncolytic virus spread).

Chapter 4

Multi-scale Moving Boundary Modelling of Cancer Interactions with a Fusogenic Oncolytic Virus: the Impact of Syncytia Dynamics

Oncolytic viral therapies is one of the new promising strategies against cancer, due to the ability of oncolytic viruses to specifically replicate inside cancer cells and kill them. There is increasing evidence that a sub-class of viruses that contain fusion proteins (triggering the formation of syncytia) can lead to better oncolytic results. Since the details of the tumour dynamics following syncytia formation are not fully understood, in this study we consider a modelling and computational approach to describe the effect of a fusogenic oncolytic virus on the multiscale dynamics of a spreading tumour. We show that for the baseline parameter values considered here, small syncytia diffusion coefficient leads to tumour reduction. Further tumour reduction can be obtained when we increase the probability of syncytia formation,

in the context of different viral burst rates and death rates for individually-infected tumour cells and syncytia structures. Finally, we show that the type of syncytia diffusion coefficient (i.e., constant or density dependent) also impacts the outcome of the oncolytic viral therapy.

4.1 Introduction

Oncolytic viral therapy has become a promising anti-cancer treatment approach due to the ability of these viruses to preferentially replicate inside cancer cells and eliminate them Seymour and Fisher (2016). While there are some clinical successes Zeh et al. (2015), there are still significant challenges that impede a wider and more common use of this type of therapy: from challenges associated with the systemic delivery of the viruses (and their elimination by various immune responses), to the physical barriers caused by the extracellular matrix (ECM) Vähä-koskela and Hinkkanen (2014). Regarding the systemic delivery of oncolytic viruses, the intravenous administration would be the preferable option, since viruses could thus reach both the primary tumours and the metastases. However, due to the immune system and other physiological filters which eliminate these viruses, the current approaches focus mostly on intra-tumoural injection of the oncolytic viruses Marchini et al. (2016). Regarding the challenge caused by the physical barriers, namely the high interstitial fluid pressure and the physical presence of ECM, this can be tackled with the help of matrix-degrading enzymes that degrade various types of fibrillar matrix deposits and make space between cells, which might eventually increase the possibility of oncolytic viral infection Vähä-koskela and Hinkkanen (2014).

While there are many types of oncolytic viruses used in experiments and in clinical trials Meerani and Yao (2010); Kauman et al. (2015); Krabbe and Altomonte (2018), some lead to better anti-tumour results than others. For example, there is

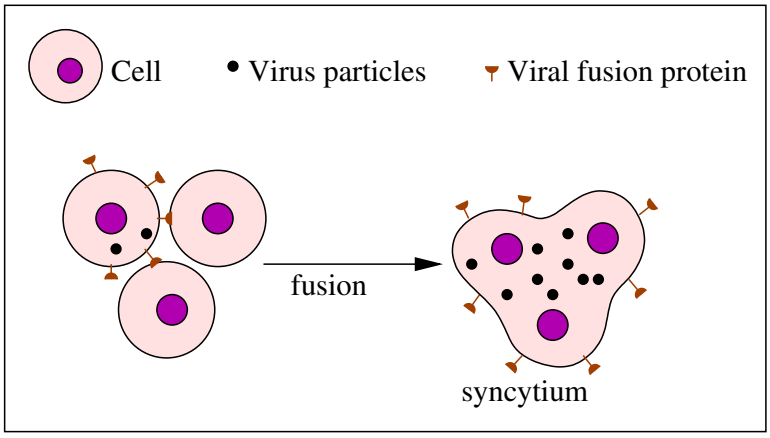

Figure 4.1: *Graphical description of a viral-induced syncytium.*

increasing evidence suggesting that a sub-class of oncolytic viruses which encode for fusion proteins (and thus lead to the formation of syncytia structures; see also Fig. 4.1) might lead to better anti-tumour effects compared to the non-fusogenic viruses Krabbe and Altomonte (2018); Ebert et al. (2004). During infection with fusogenic viruses, viral fusion proteins that are used by these viruses to enter the cells, are transported to the surface of the infected cell where they mediate the fusion of this cell to the neighbouring uninfected cells Krabbe and Altomonte (2018); Ebert et al. (2004). The syncytia structures are motile, as they extend large pseudopods to move (and their average instantaneous velocity could be slightly larger than the velocity of single cells Sylwester et al. (1993)). This movement, together with the movement of single cells, was shown to play a role in the recruitment of more cells in the syncytia Sylwester et al. (1993). While these syncytia seem to contribute to the faster spread of the oncolytic virus through the uninfected tumour via their higher viral yield and faster replication kinetics Ebert et al. (2004); Krabbe and Altomonte (2018); Ayala-Breton et al. (2014), the structures are usually viable for a short time (usually 2 days Higuchi et al. (2000)) before they undergo immunogenic cell death. We should also mention here that there are still many unknown aspects

surrounding the role of syncytium formation on the spread of an infection, such as whether this syncytium could also "sink" an infection Compton and Schwartz (2017). The authers used the term "Fusion sinks" to indicate an infection area at which syncytia cells lose thier ability of viral replication or spread.

Therefore, to further enhance the therapeutic potential of the fusogenic viruses, one needs to understand better the interactions between these motile structures and the multiscale aspects of cancer invasion (e.g., the movement of cancer cells versus the movement of syncytia, the degradation of ECM by cancer cells and its impact on the formation and spread of syncytia). Mathematical models can test and propose new hypotheses regarding these multiscale interactions.

The majority of the mathematical models that focus on fusogenic oncolytic viruses consider only the implicit (temporal) dynamics of syncytia cancer cells Biesecker et al. (2009); Bajzer et al. (2008); Laaroussi et al. (2014). There are also a few mathematical models that consider the explicit dynamics of the syncytia; see for example Dingli et al. (2009) for a temporal (ODE) model, and Jacobsen and Pilyugin (2015); Berg et al. (2019) for spatio-temporal models. Moreover, the large majority of these models focus on a single-scale dynamics of viruses spread among cancer cells. Nevertheless, there are also a very few multiscale models for oncolytic virus infections Paiva et al. (2009); Alzahrani et al. (2019).

In this study we revisit the novel multi-scale mathematical modelling framework introduced in Alzahrani et al. (2019) for cancer cells interactions with oncolytic viruses, and extend it to incorporate also the dynamics of the syncytia generated by fusogenic viruses. At the macroscopic scale, we investigate the dynamical interactions between three types of cancer cells (uninfected, viral-infected and syncytia-forming cells) and oncolytic viruses, in parallel with their movement through the extracellular matrix (ECM). At the microscopic scale, we focus on the proteolytic

dynamics of the urokinase plasminogen activator system (uPA) that locates at the invasive edge of the tumour site and is responsible for the degradation of the ECM. The macro-scale (tissue-scale) dynamics connects with the micro-scale (cell-scale) dynamics through a double feedback link that will be explained in more detail in the next section.

Using this new multiscale moving-boundary mathematical model, we investigate numerically a few hypotheses regarding syncytia movement (Anderson et al., 2000; Petrie et al., 2009; Huda et al., 2018; Wu et al., 2014; Weiger et al., 2013): via pure diffusion (faster/slower than the diffusion of single infected cancer cells), or via diffusion combined with haptotactic movement towards ECM components. We also investigate the effect of density-dependent diffusion coefficient for the syncytium structure (since it is unknown whether there is any relationship between the speed of syncytium and the density of virus particles that created it, and/or the density of ECM that acts as a barrier for virus/cells movement). Finally, we investigate the impact of different probabilities of syncytium formation on the outcome of oncolytic therapy.

4.2 Modelling Hypotheses and Setting

In this study, we focus on the naturally multiscale nature of the cancer-virus interaction, and explore key parts of this process (which includes for the first time (to our knowledge) the formation of virus-induced syncytia) structures through the two-scale modelling platform introduced in Trucu et al. (2013). Specifically, while the direct interaction between the cancer cell population and the virus (which can lead to the formation of syncytia depicted in Figure 4.1) is observed at macroscale, this has implications within cell-scale matrix-degarding enzymes proteolytic dynamics that takes place along the invasive edge of the tumour. As this micro-dynamics is linked

to the macroscale through a non-local double feedback link (see Figure 4.2), this crucially determines the changes in spatial tumour morphology during its evolution.

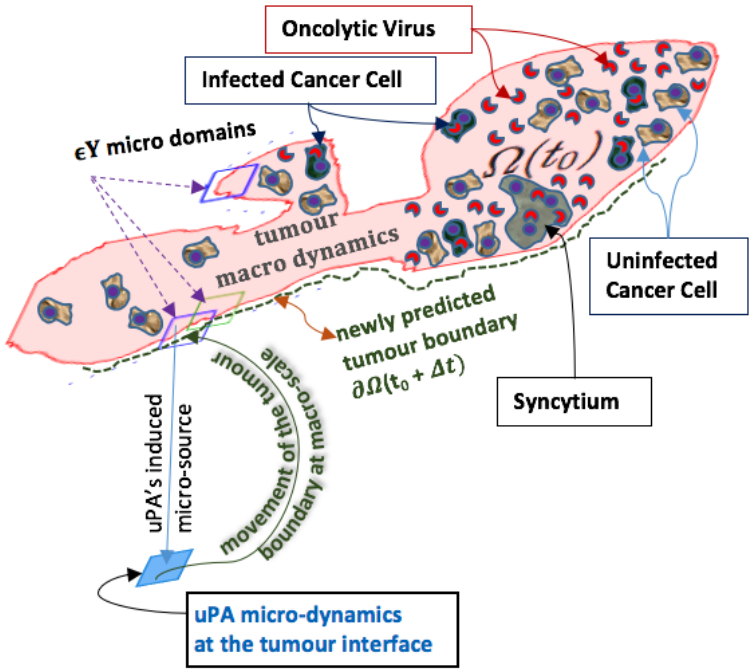

Figure 4.2: *Schematics of the multiscale moving boundary approach.*

4.2.1 Macroscopic model for virus-tumour interactions via syncytium formation

Starting with the multi-scale moving boundary mathematical framework concepts introduced in Trucu et al. (2013); Peng et al. (2017) and the syncytium assumptions introduced in Dingli et al. (2009), we describe a new multi-scale spatio-temporal mathematical model for the interactions between cancer cells and a fusogenic oncolytic virus (which leads to the formation of syncytia structures). Maintaining here the terminology of the multiscale framework introduced in Trucu et al. (2013), we denote the tissue-scale (macro-scale) growing solid tumour by $\Omega(t)$ and we assume that this evolves within a maximal cube of tissue $Y \in \mathbb{R}^N$, $N = 2, 3$, and so

$\Omega(t) \subset Y$, $\forall t > 0$. As illustrated in Figure 4.2, at the macroscopic-scale, we focus on the dynamic interactions between spatially distributed uninfected cancer cells $c(x, \cdot)$, infected cancer cells $i(x, \cdot)$ and syncytia cancer cells $s(x, \cdot)$ with the oncolytic virus (OV) particles $v(x, \cdot)$, while taking into account the surrounding extracellular matrix (ECM) density $u(x, \cdot)$, $\forall x \in \Omega(\cdot)$. (The dynamics occurring at the microscopic scale and its *top-down* and *bottom-up* links to the macroscale will be detailed in Section 4.2.2).

Before we describe the model equations, let us denote by T the total cancer cells density, which is composed of uninfected (c), viral-infected (i) and syncytia (s) cells, i.e. $T = c + i + s$. The total density of viral-infected cells is denoted by $i_{tot} = i + s$.

Following biological evidence from several experimental studies Petrie et al. (2009); Weiger et al. (2013); Huda et al. (2018); Wu et al. (2014), we assume that the uninfected cancer cells exhibit both random and directed movements. The random movement is represented here via a diffusion process (see Stroock and Varadhan (1997)). The cell directed movement that we address here is the one towards ECM gradients, and so adopting a similar approach as in Anderson et al. (2000), this is explored here via a haptotactic process. At the same time, based on further biological evidence Laird (1964, 1965); Tjorve and Tjorve (2017), we assume here that the cell proliferation process is govern by logistic growth. Finally, the cell population can decay due to infection caused by oncolytic viruses at a rate ρ and to fusion with neighbouring infected cancer cells i at a rate κ. Hence, all these considerations lead to the following governing equation for the cell uninfected population, namely:

$$\frac{\partial c}{\partial t} = D_c \Delta c - \eta_c \nabla \cdot (c \nabla u) + \mu_1 c(1 - c) - \rho c v - \kappa c i. \tag{4.1}$$

where $D_c > 0$ is a constant diffusion coefficient, $\eta_c >$ represents a constant haptotactic rate, μ_1 is the logistic proliferation rate.

For the viral-infected cancer cells, drawing upon the same biological consideration as for the uninfected cancer cells Petrie et al. (2009); Weiger et al. (2013); Huda et al. (2018); Wu et al. (2014), we assume that also this population move randomly with diffusion coefficient D_i and can move in a haptotactic manner towards higher ECM gradients with rate η_i. The proliferation of viral-infected cancer cells is the result of infection with the oncolytic virus at a rate ρ, as well as the failure to form a syncytium structure that leads to individual infected cells. We denote by p_0 the probability that a syncytium structure will fail to form following the interactions between uninfected and infected cancer cells ($p_0\kappa cci$). Thus, $(1-p_0)$ will denote the probability that a syncytium will form (and $(1-p_0)\kappa cci$ will describe the formation of syncytia structures). Finally, the infected cancer cells die at rate δ_i. These assumptions are described by the following equation:

$$\frac{\partial i}{\partial t} = D_i \Delta i - \eta_i \nabla \cdot (i \nabla u) + \rho c v + p_0 \kappa c i - \delta_i i \tag{4.2}$$

For syncytia dynamics, we consider three distinct assumptions (Nowak and May, 2000; Dingli et al., 2009; Wodarz et al., 2012; Rioja et al., 2016), namely:

(a) no diffusion (so their dynamics is the result of the formation of syncytia structure as described above, combined with death at a rate δ_s) :

$$\frac{\partial s}{\partial t} = (1-p_0)\kappa c i - \delta_s s. \tag{4.3}$$

(b) diffusion (with coefficient D_s) without haptotactic movement towards the nearby ECM components:

$$\frac{\partial s}{\partial t} = D_s \Delta s + (1-p_0)\kappa c i - \delta_s s. \tag{4.4}$$

(c) diffusion (with coefficient D_s) and haptotactic movement (at rate η_s) towards higher ECM gradients:

$$\frac{\partial s}{\partial t} = D_s \Delta s - \eta_s \nabla \cdot (s \nabla u) + (1 - p_0)\kappa c i - \delta_s s. \tag{4.5}$$

For the extracellular matrix (ECM) we assume that it does not migrate nor diffuse, but can be remodelled. To describe this remodelling process, we assume that ECM components grow logistically at rate μ_2 (while competing for space with the cancer cells: uninfected, infected and syncytia). In addition, ECM is degraded by all three type of cancer cells: by uninfected cells at rate α_c, by viral-infected cells at rate α_i, and by syncytia at rate α_s. Therefore the evolution of the density of ECM components is described by the following equation:

$$\frac{\partial u}{\partial t} = -u(\alpha_c c + \alpha_i i + \alpha_s s) + \mu_2 u(1 - u - c - i - s) \tag{4.6}$$

Finally, we assume that the oncolytic virus particles proliferate when they are released by the infected and syncytia cancer cells at rates b_i and b_s, respectively. These virus particles have the ability to diffuse at rate D_v, and to move haptotacticaly towards higher ECM gradients at rate η_v. Moreover, the free virus particles are eliminated (i.e., die) at a rate δ_v. Their numbers are also reduced when they infect at a rate ρ (and thus become trapped inside) the uninfected cancer cells. The previous assumptions are described mathematically by the following equation:

$$\frac{\partial v}{\partial t} = D_v \Delta v - \eta_v \nabla \cdot (v \nabla u) + b_i i + b_s s - \rho c v - \delta_v v. \tag{4.7}$$

The above equations describe the non-dimensional macroscopic scale dynamics in three different cases of gradual increasing complexity, which we summarise below

as follows:

First case: syncytia cancer structures do not diffuse on the spatial domain, but they still have interactions with the ECM components whenever they meet on the micro spatial domain (i.e. they still play a central role on ECM remodelling and degradation). The full macroscopic model is given by:

$$\begin{cases} \frac{\partial c}{\partial t} = D_c \Delta c - \eta_c \nabla \cdot (c \nabla u) + \mu_1 c(1-c) - \rho c v - \kappa c i, \\ \frac{\partial i}{\partial t} = D_i \Delta i - \eta_i \nabla \cdot (i \nabla u) + \rho c v + p_0 \kappa c i - \delta_i i, \\ \frac{\partial s}{\partial t} = (1-p_0)\kappa c i - \delta_s s, \\ \frac{\partial u}{\partial t} = -u(\alpha_c c + \alpha_i i + \alpha_s s) + \mu_2 u(1-u-c-i-s), \\ \frac{\partial v}{\partial t} = D_v \Delta v - \eta_v \nabla \cdot (v \nabla u) + b_i i + b_s s - \rho c v - \delta_v v. \end{cases} \tag{4.8}$$

Second case: syncytia cancer structures have diffusion abilities, but they do not interact haptotactically with the nearby ECM's components. The full macroscopic model is therefore given by:

$$\begin{cases} \frac{\partial c}{\partial t} = D_c \Delta c - \eta_c \nabla \cdot (c \nabla u) + \mu_1 c(1-c) - \rho c v - \kappa c i, \\ \frac{\partial i}{\partial t} = D_i \Delta i - \eta_i \nabla \cdot (i \nabla u) + \rho c v + p_0 \kappa c i - \delta_i i, \\ \frac{\partial s}{\partial t} = D_s \Delta s + (1-p_0)\kappa c i - \delta_s s, \\ \frac{\partial u}{\partial t} = -u(\alpha_c c + \alpha_i i + \alpha_s s) + \mu_2 u(1-u-c-i-s), \\ \frac{\partial v}{\partial t} = D_v \Delta v - \eta_v \nabla \cdot (v \nabla u) + b_i i + b_s s - \rho c v - \delta_v v. \end{cases} \tag{4.9}$$

Third case: syncytia cancer structures diffuse randomly in the spatial domain and also move haptotactically towards higher ECM gradients. Thus the full

macroscopic model is given by:

$$\begin{cases} \frac{\partial c}{\partial t} = D_c \Delta c - \eta_c \nabla \cdot (c \nabla u) + \mu_1 c(1-c) - \rho c v - \kappa c i, \\ \frac{\partial i}{\partial t} = D_i \Delta i - \eta_i \nabla \cdot (i \nabla u) + \rho c v + p_0 \kappa c i - \delta_i i, \\ \frac{\partial s}{\partial t} = D_s \Delta s - \eta_s \nabla \cdot (s \nabla u) + (1-p_0) \kappa c i - \delta_s s, \\ \frac{\partial u}{\partial t} = -u(\alpha_c c + \alpha_i i + \alpha_s s) + \mu_2 u(1-u-c-i-s), \\ \frac{\partial v}{\partial t} = D_v \Delta v - \eta_v \nabla \cdot (v \nabla u) + b_i i + b_s s - \rho c v - \delta_v v. \end{cases} \tag{4.10}$$

Furthermore, each of these coupled dynamics are accompanied by initial conditions

$$c(x,0) = c_0(x), \quad i(x,0) = i_0(x), \quad s(x,0) = s_0(x), \quad x \in \Omega(0),$$

$$u(x,0) = c_0(x), \quad v(x,0) = i_0(x), \quad x \in Y,$$

which will be specified explicitly with particular forms for numerical simulations in Section 4.3.

Finally, since we do not assume any transport across the boundary of the activity domains, each of these coupled dynamics are accompanied by Neumann zero boundary conditions, namely:

$$\left.\frac{\partial c}{\partial n}\right|_{\partial\Omega(t)} = 0; \quad \left.\frac{\partial i}{\partial n}\right|_{\partial\Omega(t)} = 0; \quad \left.\frac{\partial s}{\partial n}\right|_{\partial\Omega(t)} = 0;$$

$$\left.\frac{\partial u}{\partial n}\right|_{\partial Y} = 0; \quad \left.\frac{\partial v}{\partial n}\right|_{\partial Y} = 0;$$

were n represents simply the normal direction across the interface of the corresponding activity domain.

4.2.2 The microscopic proteolytic dynamics and its double feedback to link to macro-scale

In this chapter, the microscopic proteolytic dynamics is given by the 3D-reaction-diffusion-taxis as previously presented in (3.22). However, for convenience, we give a short discription of the model assumptions in the following text. The uPA enzymatic system includes the coupled dynamics of three main molecular species (see Andreasen et al. (2000, 1997)), namely: (1) the inactive urokinase plasminogen activator (uPA); (2) uPA inhibitor (PAI-1); and (3) plasmin. In order to become active, the inactive uPA needs first to bind to the uPA receptors (uPAR). Once activated, the active uPA can activate the plasmin molecules (which are freely available in ECM) turning these into plasmin. However, at the same time, the active uPA molecules can also become inactive if these are bound by inhibitor molecules PAI-1, leaving this way the dynamics of the uPA system. Mathematically, we denote here the spatio-temporal distribution for each of these molecular species in the uPA system as follows:

- $a(y,\tau)$ represents the urokinase plasminogen activator (uPA), without distinguishing here between its active and inactive forms;
- $p(y,\tau)$ stands for the inhibitor PAI-1; and
- $m(y,\tau)$ is the plasmin;

where $(y,\tau) \in \mathbf{B}_{\|\cdot\|_\infty}(\partial\Omega(t_0),\epsilon)$, with $\mathbf{B}_{\|\cdot\|_\infty}(\partial\Omega(t_0),\epsilon)$ representing a cell-scale neighbourhood of radius $\epsilon > 0$ for the tumour interface $\partial\Omega(t_0)$.

To address the multiscale dynamics of the cancer invasion process while accounting for the important role of the cell-scale (micro-scale) dynamics of the uPA system at the invasive edge of the tumour, the authors in Peng et al. (2017) have applied the

two-scale moving boundary framework initially introduced in Trucu et al. (2013) to explore the impact the uPA has upon the changes in the tissue-scale (macro-scale) tumour morphology of the growing cancer. Therefore, since here we build upon these two previous works and expand these by accounting also for the presence of an oncolytic virus with syncytia formation at macro-scale, to describe the micro-dynamics and its non-local feedback links with the tumour macro-dynamics that, let us briefly revisit in the following the key notations of the framework introduced and discussed in Trucu et al. (2013); Peng et al. (2017). Thus, to capture the micro-scale dynamics occurring at the invasive edge of the tumour, following a series of topological considerations, as described in Trucu et al. (2013), a covering family $\mathcal{P}$ consisting of overlapping cubes $\mathcal{P}(t) := \{\epsilon Y\}_{\epsilon Y \in \mathcal{P}(t)}$ is constructed from a section of *half-way shifted small cubes of* an appropriately chosen dyadic decomposition of the maximal tissue macro-cube Y (where the tumour $\Omega(t)$ invades) that cover the tumour interface $\partial\Omega(t)$, which, in brief, exhibits and is completely determined by the following properties:

- each ϵY, also referred to as a *micro-domain*, provides a cell-scale neighbourhood of $\epsilon Y \cap \partial\Omega(t)$ of micro-scale size $\epsilon > 0$ with the particular properties that the regions captured inside and outside of the boundary, namely $\epsilon Y \cap \Omega(t)$ and $\epsilon Y \setminus \Omega(t)$, have topologically connected interiors;

- the family $\mathcal{P}(t) := \{\epsilon Y\}_{\epsilon Y \in \mathcal{P}(t)}$ covers completely the boundary $\partial\Omega(t)$.

Thus, at any given time $t_0 > 0$, the covering bundle $\mathcal{P}(t_0)$ enables the exploration of the uPA system dynamics on the cell-scale neighbourhood $\mathbf{B}_{\|\cdot\|_\infty}(\partial\Omega(t_0), \epsilon)$ by decomposing this in a bundle of uPA micro-processes on each of the micro-domains ϵY. In this context, during any macroscopic time range $[t_0, t_0 + \Delta t]$ that is correspondingly matched by an equal length micro-scale time span $[0, \Delta t]$ for the microdynamics, on any micro-domain ϵY, a source of uPA arises naturally at any

micro-scale point $y \in \epsilon Y$ as a collective contribution not only of the uninfected cancer cells but also of the infected cancer cells and syncytia population that arrive within a given distance $\delta > 0$ with respect to y, see Figure 4.2. Thus, the microscale source of uPA is induced non-locally by the macro-dynamics through a *top-down link*, and this can be mathematically expressed as

$$f^{\epsilon Y}_{uPA}(y,\tau) = \frac{\int_{\mathbf{B}(y,\delta)\cap\Omega(t_0} (\lambda_c c + \lambda_i i + \lambda_s s)(\sigma, t_0+\tau)d\sigma}{\lambda(\mathbf{B}(y,\delta)\cap\Omega(t_0)} \tag{4.11}$$

where $\tau \in [0, \Delta t]$ and λ_c, λ_i and λ_s are the rates at which the uninfected cancer cells, the infected cancer cells and syncytia population secrete uPA, respectively. At the same time, the inhibitor PAI-1, which is produced through the activation of plasmin, is eliminated from the system dynamics after binding to uPA and, notably, through non-local binding to the surrounding ECM (more specifically, to its constituent vitronectin). This binding of PAI-1 to constituents of the surrounding tissue-scale ECM density acts therefore as an absorption term for the PAI-1 micro-dynamics, whose absorption coefficient is again mediated and induced by the macro-dynamics (enhancing this way the *top-down feedback link*) and can be formalised mathematically through the non-local expression

$$f^{\epsilon Y}_{PAI-1}(y,\tau) = \frac{\int_{\mathbf{B}(y,\delta)} u(\sigma, t_0+\tau)d\sigma}{\lambda(\mathbf{B}(y,\delta))}. \tag{4.12}$$

where $(y,\tau) \in (\epsilon Y \cap \Omega(t_0)) \times [0, \Delta t]$.

4.3 Multiscale Numerical Simulations for Macro-Dynamics Cases (4.8)-(4.10)

Starting from the two-scale computational framework that was previously developed in Alzahrani et al. (2019) for the case that was not considering syncytia structures formation (which was based on the initial two-scale framework proposed in Trucu et al. (2013)), we developed that framework further to cope with the new context of multiscale dynamics of cancer-virus interactions in the presence of syncytia structures formation. Similar to the initial framework (introduced in Trucu et al. (2013)), the extended multiscale numerical scheme that we developed and use here combines predictor-corrector finite differences for the macro-dynamics with quadrilateral finite element approach for micro-dynamics. Further, as detailed in Trucu et al. (2013), the internal macro-mesh is extended with additional mesh points when the boundary is relocated (which are activated from a silent background mesh on the maximal tissue cube Y). Finally, since the development of this extended numerical scheme required a discretisation strategy similar to that used in the non-syncytia case (considered in Alzahrani et al. (2019)), we did not include that here and instead, for details of the main implementation steps, we refer the reader to Alzahrani et al. (2019); Trucu et al. (2013).

4.3.1 Initial conditions for the macro-micro model

The initial distribution of the uninfected cancer cells (which form a tumour localised in the middle a computational domain $Y = [0, 8] \times [0, 8]$) is given by:

$$c(x, 0) = \frac{\left(exp(-\frac{\|x-(4,4)\|_2^2}{\sqrt{\Delta x \Delta y}}) - exp(-28.125)\right)\theta_1(x)}{2},$$

where $\theta_1(x) := \chi_{\mathbf{B}((4,4),0.5-\gamma)} * \psi_\gamma$, with ψ_γ a Gaussian mollifier that enables a smooth transition to zero outside a radius of 0.5 of the ball $\mathbf{B}((4,4),0.5)$, as shown Figure 3.2-(a).

Since the oncolytic virus is introduced into the system at the start of the simulations, it makes sense to assume that at this time (i.e., $t = 0$) there are no virus-infected and syncytia cancer cells:

$$i(x,0) = 0, \quad \text{and} \quad s(x,0) = 0.$$

Regarding the virus, we assume that this is injected at tumour site (at the start of the simulations), via a single or multiple insertion points Bai et al. (2019); Hoffner et al. (2016); Seery (2017). For the baseline simulations, we choose a single insertion point, as described in Figure (3.2)(c) and given by the expression

$$v(x,0) = \frac{\left(exp(-\frac{\|x-(4.5,4.5)\|_2^2}{\sqrt{\Delta x \Delta y}}) - exp(-28.125)\right)\theta_2(x)}{2},$$

where $\theta_2(x) := \chi_{B((4.5,4.5),0.5-\gamma)} * \psi_\gamma$. However, for an improved viral therapy outcome scenario (given that the initial tumour lesion is quite spread over space – see Figure (3.2)(a)), we inject five virus doses at different positions inside the tumour, as shown in Figure (3.2)(d):

$$\begin{aligned} v(x,0) = & \\ & \sum_{i,j\in\{-1,1\}} 0.5\Big(exp(-\tfrac{\|x-(4+0.5i,4+0.5j)\|_2^2}{\sqrt{\Delta x \Delta y}}) - exp(-28.125)\Big)\theta_{i,j}(x) \\ & +0.5\left(exp(-\tfrac{\|x-(4,4)\|_2^2}{\sqrt{\Delta x \Delta y}}) - exp(-28.125)\right)\theta_1(x), \end{aligned}$$

where $\theta_{i,j}(x) := \chi_{B((4+0.5i,4+0.5j),0.5-\gamma)} * \psi_\gamma$, $\forall i,j \in \{-1,1\}$.

Finally, since the ECM is naturally heterogeneous, we considered here the fol-

lowing ECM initial condition :

$$u(x,0) = \frac{1 + 0.3sin(4\pi \left\|x\right\|_2) + sin(4\pi \left\|(4,0) - x\right\|_2)}{2}.$$

Further insights upon the impact that the choice of the ECM initial conditions has on the overall tumour evolution are discussed in A.2, where we explore the sensitivity of the viral treatment of the tumour with respect to the level of heterogeneities within the ECM.

Parameter	Value	References
D_c	0.00675	Camara et al. (2013)
D_i	0.0054	Camara et al. (2013)
D_s	0.0027	$\frac{D_i}{2}$
D_v	0.0036	Camara et al. (2013)
η_c	2.85×10^{-2}	Peng et al. (2017)
η_i	2.85×10^{-2}	Peng et al. (2017)
η_s	2.85×10^{-3}	Estimated
η_v	2.85×10^{-3}	Alzahrani et al. (2019)
μ_1	0.25	Peng et al. (2017)
ρ	79×10^{-3}	Camara et al. (2013)
κ	158×10^{-3}	$\kappa > \rho$, Biesecker et al. (2009), Peng et al. (2002)
δ_i	0.05	Camara et al. (2013)
δ_s	0.05	$(\delta_s = \delta_i)$ Estimated
δ_v	0.025	Camara et al. (2013)
α_c	0.15	Peng et al. (2017)
α_i	0.075	Alzahrani et al. (2019)
α_s	0.0375	$(\frac{\alpha_c}{4})$ Estimated
μ_2	0.015	Alzahrani et al. (2019)
b_i	2	Alzahrani et al. (2019)
b_s	2	$(b_s = b_i)$ Estimated
p_0	0.5	50% Probability
λ_c	0.8	Alzahrani et al. (2019)
λ_i	0.4	Alzahrani et al. (2019)
λ_s	0.4	$(\lambda_s = \lambda_i)$ Estimated

Table 4.1: Baseline parameters values for the macroscopic models.

Regarding the initial conditions at the microscale: we assume that the enzymes

are produced only by the cancer cells at macroscale level (and passed nonlocally to the microscale), and there are no other pre-existing enzymes in the peritumoural interface. Thus, we always consider zero initial conditions for enzymes at the microscale.

4.3.2 Parameters

To simplify the presentation of the numerical results, in the following we summarise the parameter values used in the simulations. In order to measure the performance of our multi-scale model assumptions, we first estimate the baseline parameter regime at both scales, namely, macroscopic and microscopic scales (summarised in Tables 4.1, 4.2), building on a combination of the possible values for the parameters according to the previous results discussed in Harpold et al. (2007); Camara et al. (2013); Peng et al. (2017); Biesecker et al. (2009); Alzahrani et al. (2019). Then, we develop this estimation to include few restrictions and values limitation according to some mathematical and biological observations in terms of tumour-OV interactions, for instance, a reasonable increase of the fusion rate κ (in a comparison with the value of viral infection rate ρ) mostly leads to a controlled cancer invasion scenario (Biesecker et al., 2009).

Parameter	Value
D_a	2.5×10^{-3}
D_p	3.5×10^{-3}
D_m	4.91×10^{-3}
ψ_{11}	0.75
ψ_{12}	0.215
ψ_{13}	0.3
ψ_{21}	0.75
ψ_{22}	0.55
ψ_{23}	0.5
ψ_{31}	0.11
ψ_{32}	0.75
ψ_{33}	0.5

Table 4.2: Summary of parameter values for the microscopic model component. All parameters for this system are taken from the reference Peng et al. (2017).

4.3.3 Results

To investigate the different scenarios discussed in the previous section (regarding the tumour-OV interactions in the presence of cells syncytium) we start our numerical simulations with the baseline parameters summarised in Tables 4.1, 4.2.

We start our numerical investigation of the multiscale moving-boundary model proposed in this study by focusing on the three cases of syncytia movement/lack-of-movement. For the first case, described mathematically by the macro-dynamics (4.8), we assume that syncytia structures do not have any movement ability (i.e., neither diffusive nor haptotactic movement), but they can still play a role in the remodelling and degradation of ECM components on the tumour region $\Omega(t)$. The dynamics of the various macroscale model components is presented in Figure 4.3, where we show (for three different micro-macro stages, 1, 50 and 100): the virus density (row a.), the density of uninfected cancer cells (row b.), the density of infected cancer cells (row c.), the density of syncytia cancer cells (row d.), total cancer cells density (row e.), and ECM density (row f.). We note that in this case,

Parameter	Value	References
D_c	0.00675	Camara et al. (2013)
D_i	0.0054	Camara et al. (2013)
D_s	0.000675	Estimated
D_v	0.0036	Camara et al. (2013)
η_c	2.85×10^{-2}	Peng et al. (2017)
η_i	2.85×10^{-2}	Peng et al. (2017)
η_s	2.85×10^{-3}	Estimated
η_v	2.85×10^{-3}	Alzahrani et al. (2019)
μ_1	0.25	Peng et al. (2017)
ρ	395×10^{-3}	Alzahrani et al. (2019)
κ	2ρ	$\kappa > \rho$, Biesecker et al. (2009), Peng et al. (2002)
δ_i	0.0125	Alzahrani et al. (2019)
δ_s	0.0125	$(\delta_s = \delta_i)$ Estimated
α_c	0.3	Alzahrani et al. (2019)
α_i	0.15	Alzahrani et al. (2019)
α_s	0.075	$(\frac{\alpha_c}{4})$ Estimated
μ_2	0.015	Alzahrani et al. (2019)
b_i	3	Alzahrani et al. (2019)
b_s	3	$(b_s = b_i)$ Estimated
p_0	0.75	Estimated
δ_v	0.025	Camara et al. (2013)
λ_c	0.8	Alzahrani et al. (2019)
λ_i	0.4	Alzahrani et al. (2019)
λ_s	0.4	$(\lambda_s = \lambda_i)$ Estimated

Table 4.3: Parameter values list for the improved tumour suppression results, as summarised in Figure (4.13).

the syncytia structures form mainly in those tumour regions characterised by lower tumour cell densities, while the single infected cells are mainly in those regions characterised by higher tumour cell densities.

For the second case, described mathematically by the macro-dynamics (4.9), we assume that syncytia cells can move randomly inside the macroscopic domain, but they do not show haptotactic migration towards regions of higher ECM levels. To investigate the effect of this random motility of syncytia structures, we perform simulations with different syncytia diffusion coefficients D_s (with respect to D_i - the

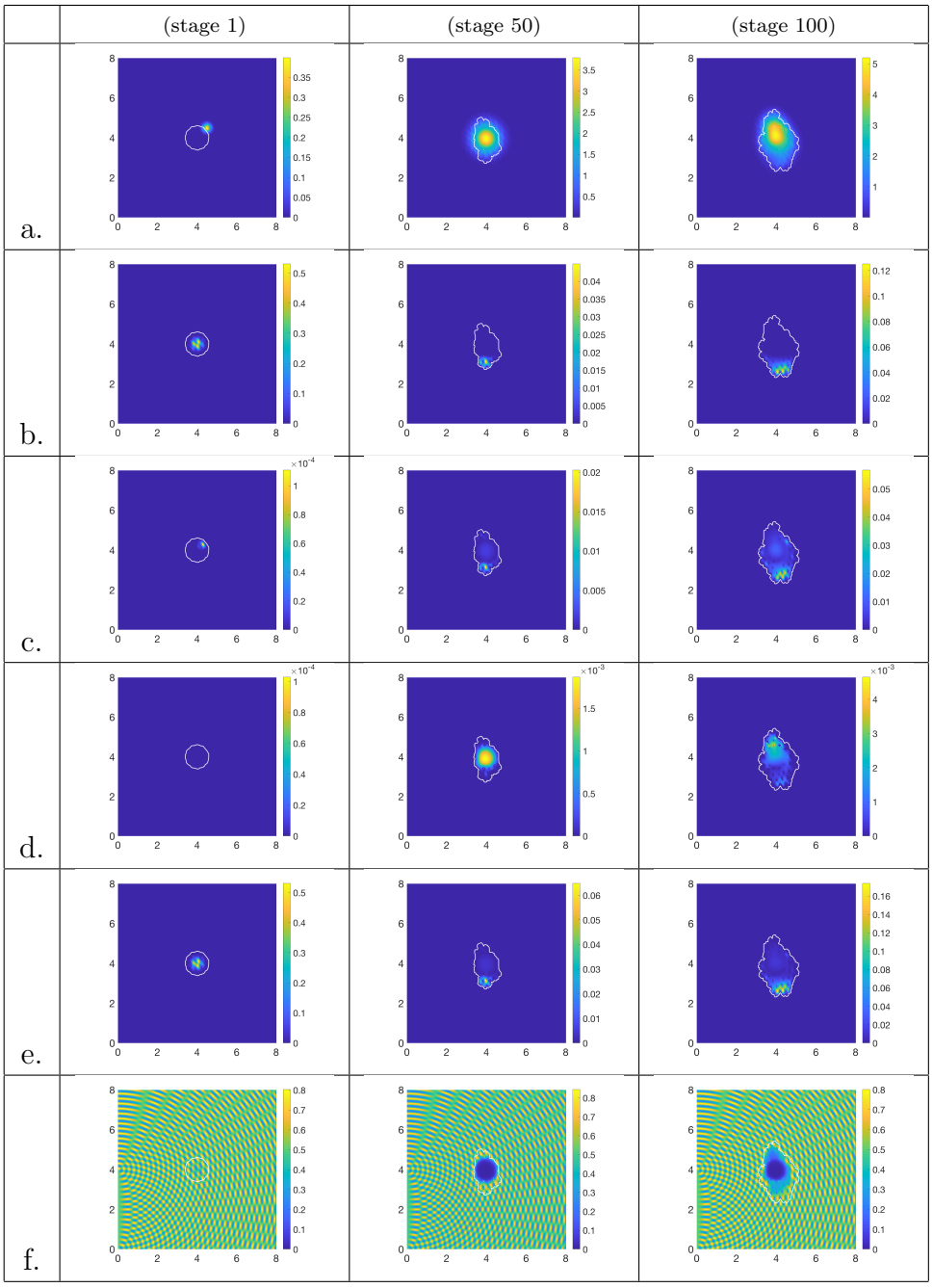

Figure 4.3: Multi-scale simulation results for macro-dynamics syncytia system (4.8) at three macro-micro stages (1,50 and 100) for the baseline parameter values from Table 4.1, showing: a. virus density; b. uninfected cancer cells density; c. infected cancer cells density; d. syncytia cancer cells density; e. total cancer cells density and f. ECM density.

diffusion coefficient of single infected cells). Thus, in Figure 4.4-(I) we investigate the situation $D_s = D_i$; in Figure 4.4-(II) we investigate the situation $D_s = D_i/4$; and in Figure 4.4-(III) we investigate the situation $D_s = 4D_i$. We observe here that lower D_s compared to D_i (i.e., $D_s = D_i/4$) leads to syncytia structures localised also in the non-infected part of the tumour, which causes an overall reduction in tumour size and tumour spread (as the invasion boundary is shrinking). In contrast, increasing D_s compared to D_i (i.e., $D_s = 4D_i$) leads to an increase in tumour size and tumour spread. It is possible that lower syncytia motility leads to more localised tumour killing and localised release of virus particles, while larger syncytia motility leads to a wider spread of the virus particles, which also increases their probability of elimination. In Figure 4.5 we summarise all these results by showing the effect of syncytia random motility on: (a) total tumour mass (i.e., uninfected+infected+syncytia); (b) tumour invasion area; (c) and the evolution of the ration between the total tumour mass and the tumour invasion area.

Next, we return to the case $b_s = b_i$ and $\delta_s = \delta_i$, and show an example of significant tumour reduction when we decrease the parameters associated with the proteolytic enzymes (see Table 4.3), which are expected to lead to smaller enzymatic transport across the tumour interface, ultimately resulting in peritumoural ECM degradation. This results in slower tumour invasion, which enables the syncytia and infected cells to be more effective at cancer cell elimination on tumour domain $\Omega(t)$. This behaviour is depicted in Figure 4.12. In Figure 4.13 we compare – in terms of total tumour mass and tumour invasion area – this improved therapy scenario versus the baseline scenario described by the parameter values listed in Table 4.1.

Finally, we investigate the third case, described mathematically by the macrodynamics (4.10), where we assume that syncytia cancer cells not only diffuse randomly but also move haptotactically towards higher ECM gradients. As before,

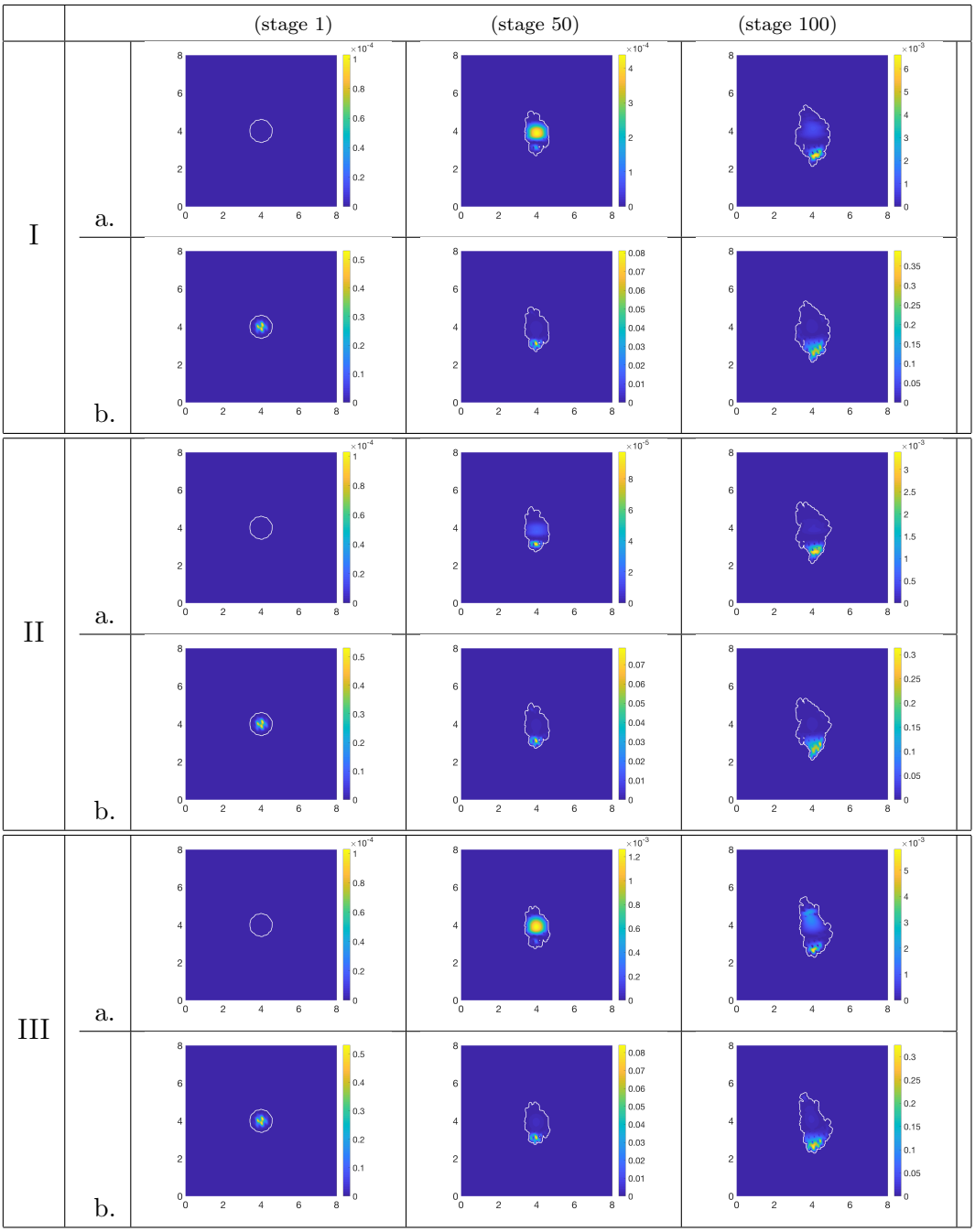

Figure 4.4: Multi-scale simulation results for macro-dynamics syncytia system (4.9) in the case of $D_s = D_i$ (in panel I), $D_s = D_i/4$ (in panel II) and $D_s = 4D_i$ (in panel III) at three macro-micro stages (1,50 and 100) for the baseline parameter values from Table 4.1, showing: a. syncytia cancer cells density and b. total cancer cells density.

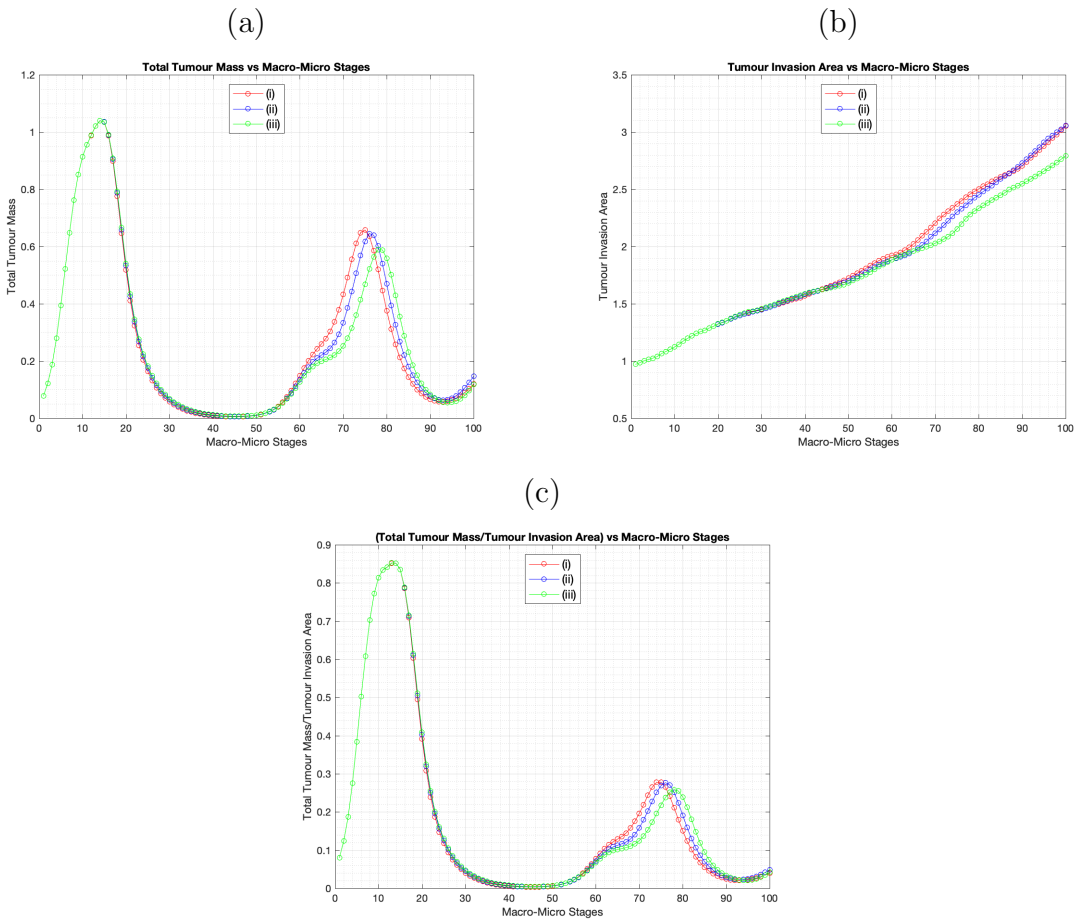

Figure 4.5: Comparison of: (a) total tumour masses evolution versus macro-micro stages 1 – 100 for the macro-dynamics case (4.9) for various random diffusion scenarios of syncytia cancer cells; (b) tumour invasion area versus macro-micro stages 1 – 100 for the macro-dynamics case (4.9) for various random diffusion scenarios of syncytia cancer cells; and (c) the evolution of the ratio of total tumour masses to tumour invasion area over macro-micro stages 1 – 100 for the macro-dynamics case (4.9) for various random diffusion scenarios of syncytia cancer cells. (i) $D_s = 4D_i$; (ii) $D_s = D_i$; (iii) $D_s = D_i/4$.

we investigate numerically the effects of various syncytia haptotactic velocities η_s (as compared with the haptotactic velocities of single infected cancer cells η_i, and the velocities of virus particles η_v). Figure 4.6 summarises these effects on: (a) total tumour size; (b) tumour invasion area for the following two sub-cases: (i) $\eta_s = \eta_i = 2.85 \times 10^{-2}$ and (ii) $\eta_s = \eta_v = 2.85 \times 10^{-3}$; and the evolution of the ration between the total tumour mass and the tumour invasion area. Note that case (ii),

where $\eta_s = \eta_v < \eta_i$, leads to a slightly better tumour outcome in terms of both tumour mass and invasion area.

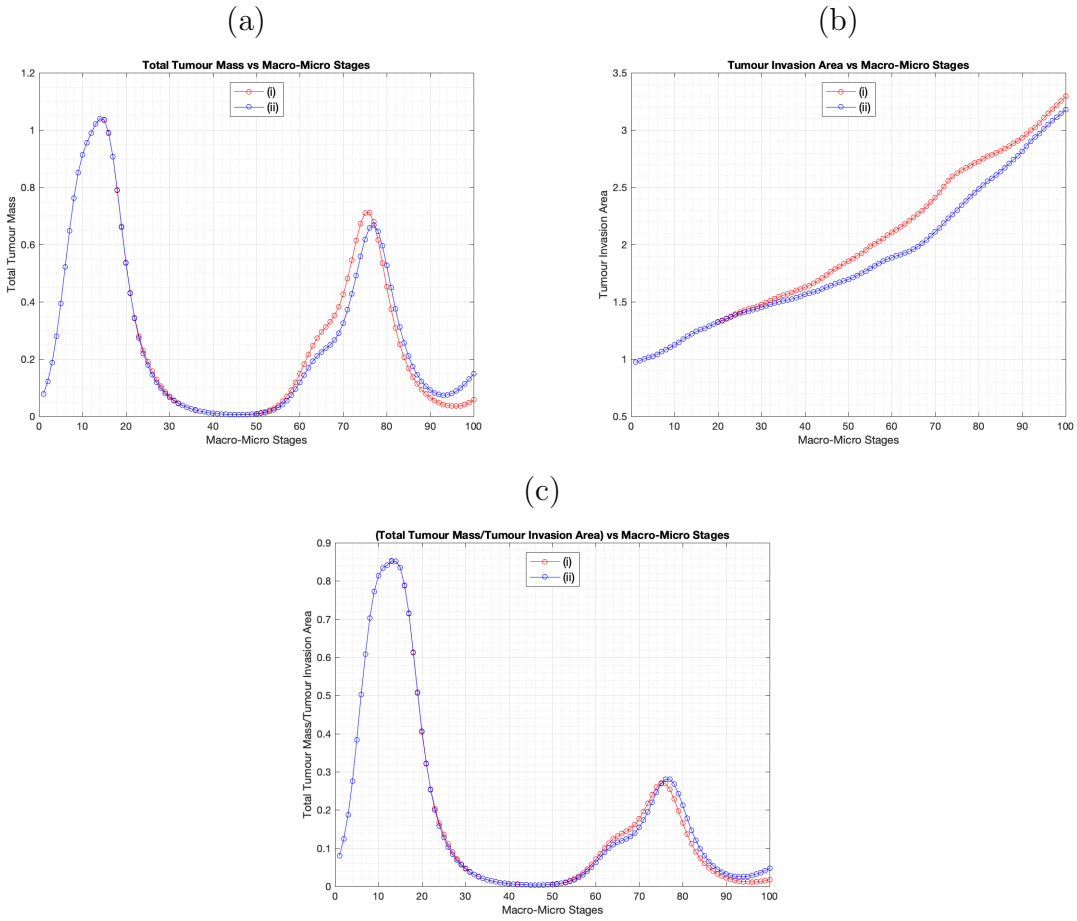

Figure 4.6: (a) Comparison of total tumour masses evolution over macro-micro stages 1 – 100 for the macro-dynamics case (4.10) for various haptotactic rates of syncytia cancer cells ECM gradients. (b) Comparison of tumour invasion area over macro-micro stages 1 – 100 for the macro-dynamics case (4.10) for various haptotactic rates of syncytia cancer cells towards ECM gradients. (c) Comparison of the evolution of the ratio of total tumour masses to tumour invasion area over macro-micro stages 1 – 100 for the macro-dynamics case (4.10) for various haptotactic rates of syncytia cancer cells ECM gradients. (i) $\eta_s = \eta_i$; (ii) $\eta_s = \eta_v$.

Having investigated the role of syncytia's diffusive/haptoctatic speeds on tumour growth and spread, we next focus on the impact of the fusion failure probability p_0 on the overall oncolytic therapy. (Note that higher p_0 means higher numbers of

individual OV-infected cancer cells i, and lower numbers of syncytia structures s). In Figures 4.7, 4.8 and 4.9 we investigate the effect of three failure levels of syncytia fusion probability: $p_0 = 50\%$, $p_0 = 25\%$ and $p_0 = 75\%$, respectively. By comparing the results in these three figures we can conclude that higher p_0 values are associated with lower syncytia densities and lower tumour sizes. The anti-tumour effect of higher p_0 probabilities can be seen more clearly in Figure 4.10, where we show the evolution of total tumour mass and tumour invasion area as well as the evolution of the ratio of total tumour masses to tumour invasion area over macro-micro stages 1 – 100.

This unexpected outcome might be caused by the assumption that $b_s = b_i$ (i.e., both individually-infected tumour cells and syncytia structure burst at the same rates to release new virus particles), and $\delta_s = \delta_i$ (i.e., both individually-infected tumour cells and syncytia structures die at the same rates). However, it makes sense to assume that syncytia live longer than the individually-infected cells Herschke et al. (2007), and that each syncytium has a higher viral yield compared to the yield of a single infected cell. Thus, in Figure 4.11 we investigate the anti-tumour/pro-tumour effects of higher syncytia burst rates ($b_s = 1.5b_i$) and lower syncytia death rates ($\delta_s = \frac{\delta_i}{5}$), and compare the results with the ones for the above case (i.e., $b_s = b_i$, $\delta_s = \delta_i$). It is clear that higher probabilities of syncytium formation (i.e., lower p_0) lead to faster tumour death when $b_s > b_i$ and $\delta_s < \delta_i$.

4.4 Extension of Macro-Dynamics Case (4.10) to Include Density-Dependent Syncytia Diffusion

The previously-discussed cases assumed that syncytia diffusion is constant. However, given the size of this giant multi-nucleated structure, it is likely that its motility

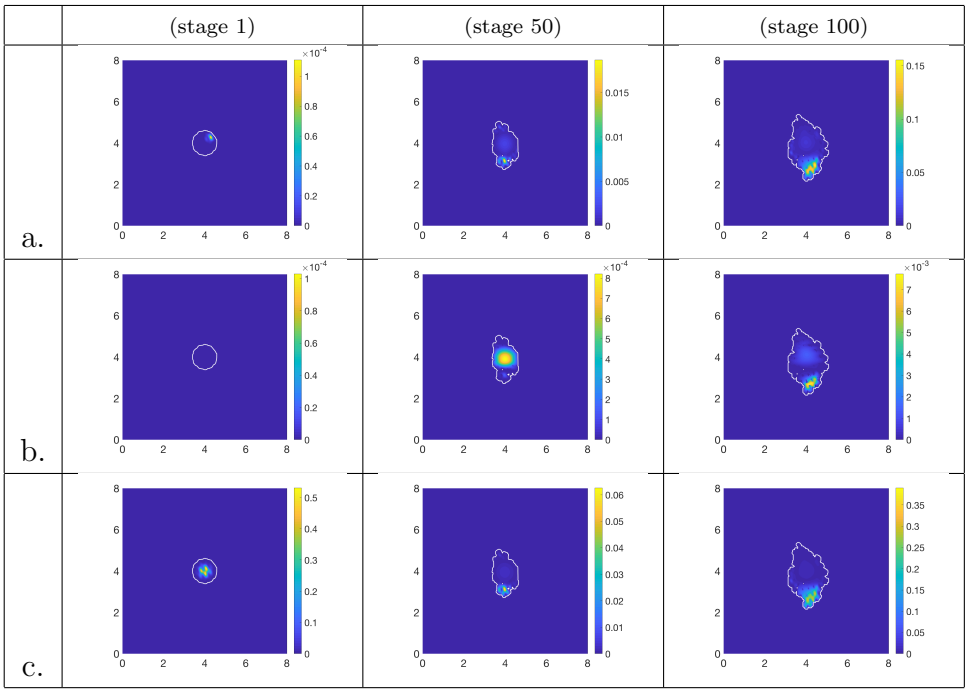

Figure 4.7: Multi-scale simulation results for macro-dynamics syncytia system (4.10) in the case of 50% fusion failure probability ($p_0 = 0.5$) at three macro-micro stages (1,50 and 100) for the baseline parameter values from Table 4.1, showing: a. infected cancer cells density; b. syncytia cancer cells density and c. total cancer cells density.

is influenced by the density of ECM, as well as the density of fusogenic oncolytic viruses (as more viruses could lead to larger syncytia, which extend larger pseudopods to move Sylwester et al. (1993)). In the following we generalise the macro-dynamics described in model (4.10) by assuming that syncytia diffusion coefficient is density dependent:

$$\begin{cases} \frac{\partial c}{\partial t} = D_c \Delta c - \eta_c \nabla \cdot (c \nabla u) + \mu_1 c(1-c) - \rho c v - \kappa c i, \\ \frac{\partial i}{\partial t} = D_i \Delta i - \eta_i \nabla \cdot (i \nabla u) + \rho c v + p_0 \kappa c i - \delta_i i, \\ \frac{\partial s}{\partial t} = \left(D_s \frac{v}{f_s(u,v)} \right) \Delta s - \eta_s \nabla \cdot (s \nabla u) + (1-p_0) \kappa c i - \delta_s s, \\ \frac{\partial u}{\partial t} = -u(\alpha_c c + \alpha_i i + \alpha_s s) + \mu_2 u(1-u-c-i-s), \\ \frac{\partial v}{\partial t} = D_v \Delta v - \eta_v \nabla \cdot (v \nabla u) + b_i i + b_s s - \rho c v - \delta_v v. \end{cases} \tag{4.13}$$

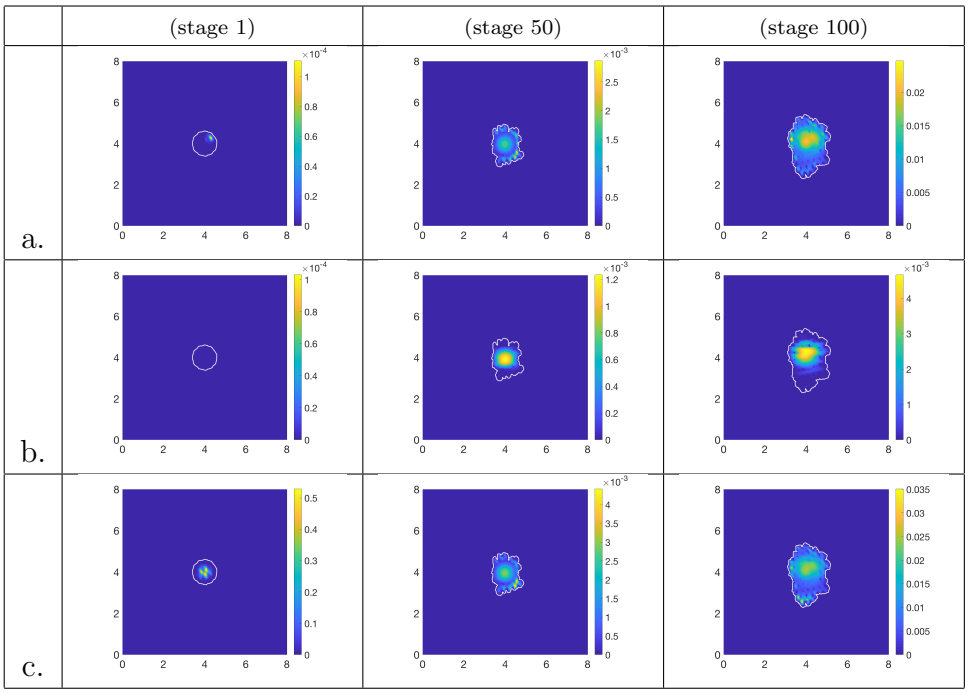

Figure 4.8: Multi-scale simulation results for macro-dynamics syncytia system (4.10) in the case of 25% fusion failure probability ($p_0 = 0.25$) at three macro-micro stages (1,50 and 100) for the baseline parameter values from Table 4.1, showing: a. infected cancer cells density; b. syncytia cancer cells density and c. total cancer cells density.

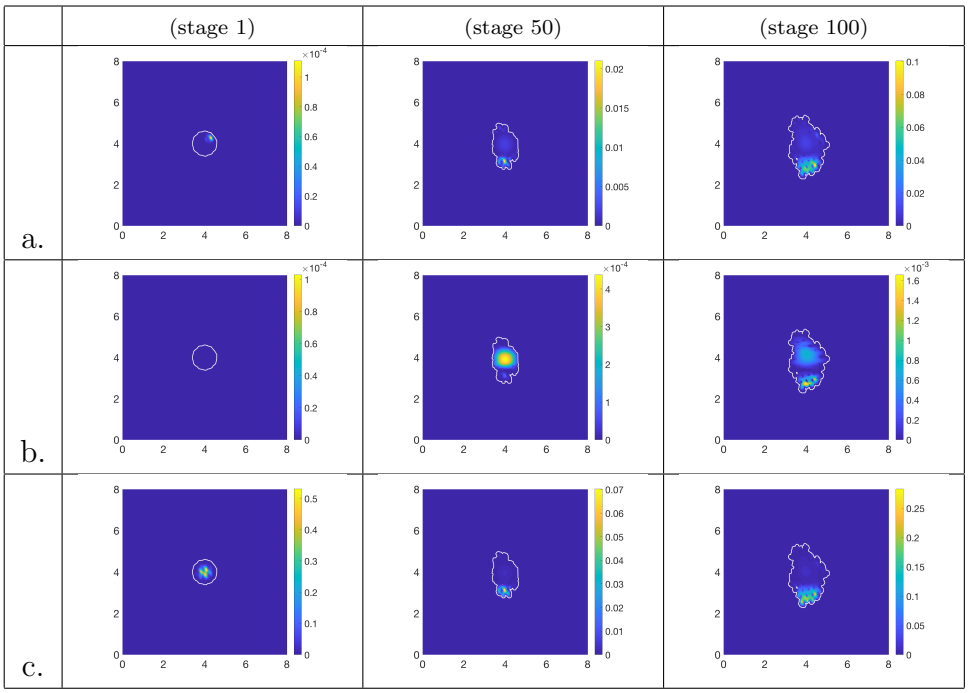

Figure 4.9: Multi-scale simulation results for macro-dynamics syncytia system (4.10) in the case of 75% fusion failure probability ($p_0 = 0.75$) at three macro-micro stages (1,50 and 100) for the baseline parameter values from Table 4.1, showing: a. infected cancer cells density; b. syncytia cancer cells density and c. total cancer cells density.

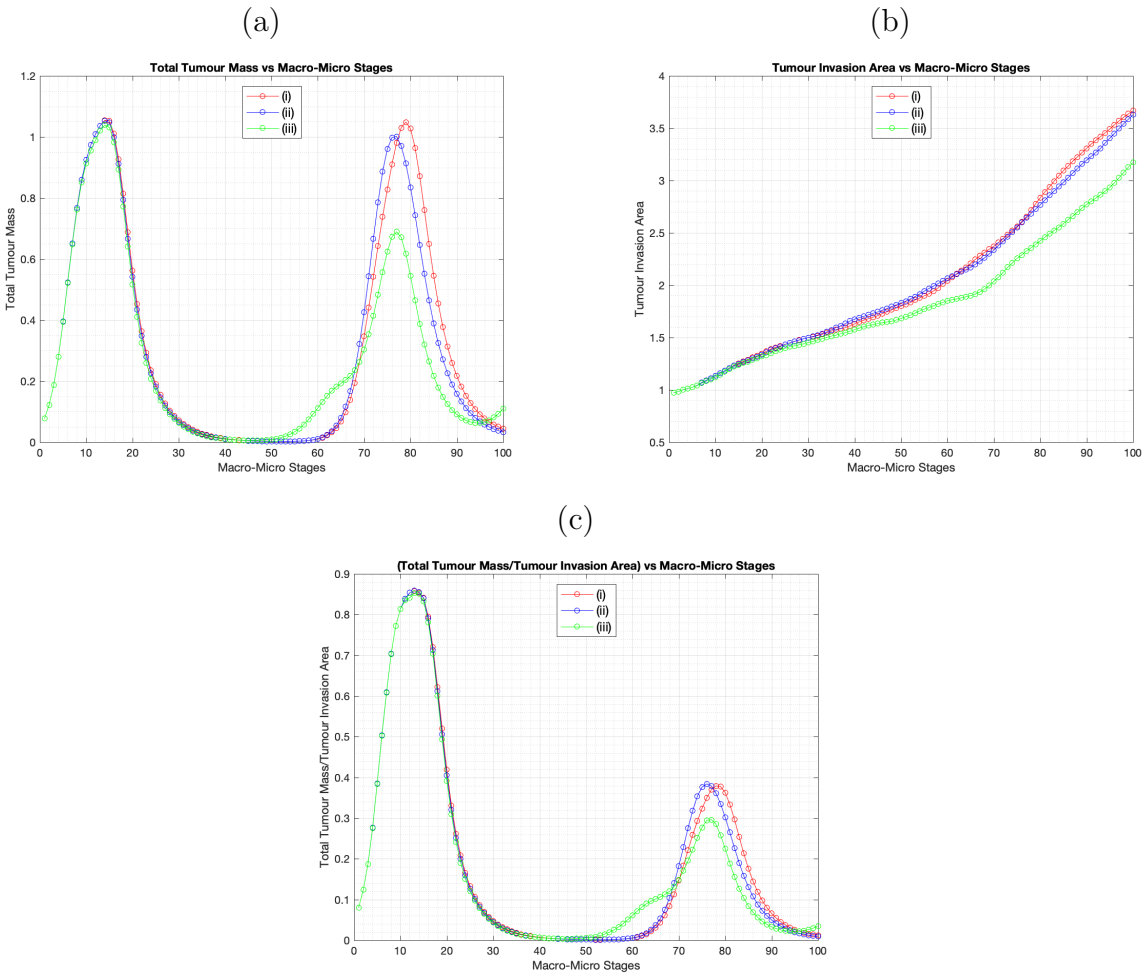

Figure 4.10: (a) Comparison of total tumour masses evolution over macro-micro stages 1 – 100 for the macro-dynamics case (4.10) for various fusion failure probabilities p_0. (b) Comparison of tumour invasion area over macro-micro stages 1 – 100 for the macro-dynamics case (4.10) for various fusion failure probabilities p_0. (c) Comparison of the evolution of the ratio of total tumour masses to tumour invasion area over macro-micro stages 1 – 100 for the macro-dynamics case (4.10) for various fusion failure probabilities p_0. (i) $p_0 = 0.25$; (ii) $p_0 = 0.50$; (iii) $p_0 = 0.75$.

Note that this model reduces to case (4.10) if we choose $f_s(u, v) = v$. In the following we consider two examples for f_s (both leading to a saturated diffusion coefficient for the syncytia structures):

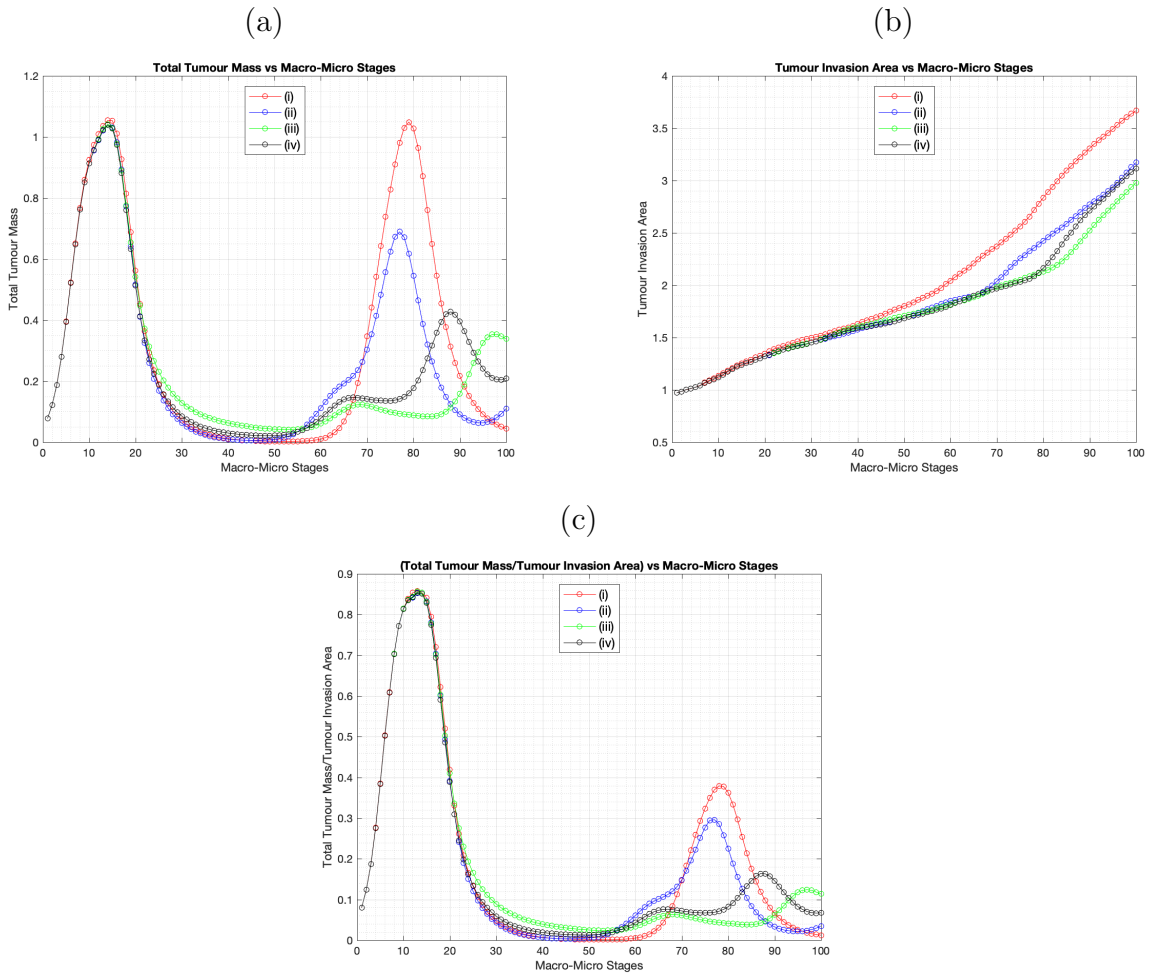

Figure 4.11: (a) Comparison of total tumour masses evolution over macro-micro stages 1 – 100 for the macro-dynamics case (4.10) for various fusion probabilities p_0. (b) Comparison of tumour invasion area over macro-micro stages 1 – 100 for the macro-dynamics case (4.10) for various fusion failure probabilities p_0 with respect to different values of b_s and δ_s. (c) Comparison of the evolution of the ratio of total tumour masses to tumour invasion area over macro-micro stages 1 – 100 for the macro-dynamics case (4.10) for various fusion probabilities p_0. (i) $p_0 = 0.25$, when $b_s = b_i$ and $\delta_s = \delta_i$; (ii) $p_0 = 0.75$ when $b_s = b_i$ and $\delta_s = \delta_i$. (iii) $p_0 = 0.25$ when $b_s = 1.5b_i$ and $\delta_s = \frac{\delta_i}{5}$; (iv) $p_0 = 0.75$ when $b_s = 1.5b_i$ and $\delta_s = \frac{\delta_i}{5}$.

i. $f_s(u, v)$ depends only on OV, and the dependence is linear:

$$f_s(u, v) = v + 1; \tag{4.14}$$

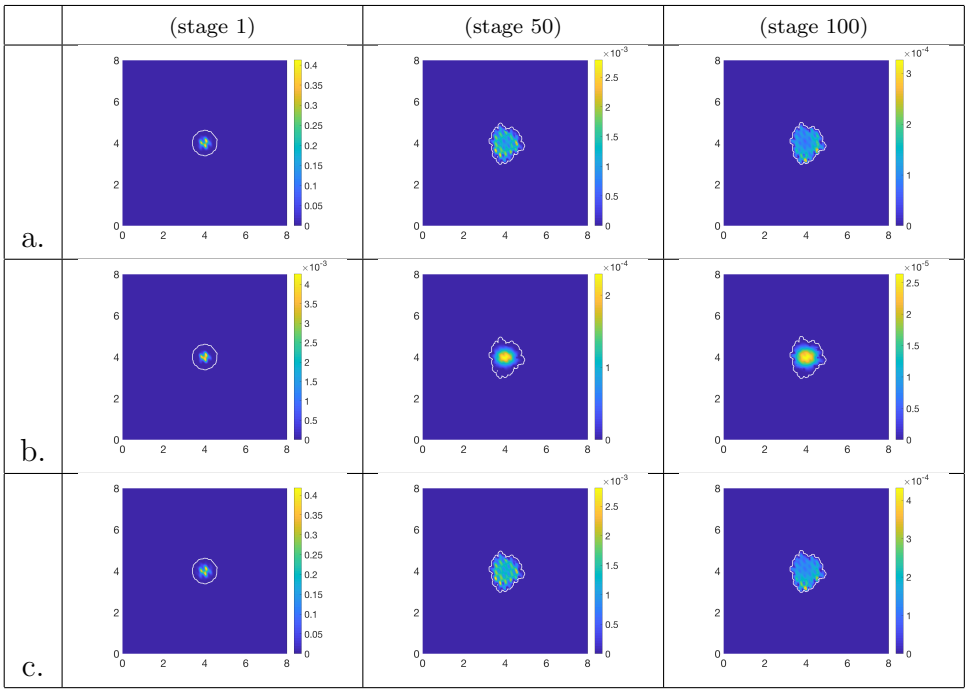

Figure 4.12: Multi-scale simulation results for macro-dynamics syncytia system (4.10) at three macro-micro stages (1,50 and 100) for the improved treatment scenario corresponding to the parameter values listed in Table 4.3, showing: a. infected cancer cells density; b. syncytia cancer cells density and c. total cancer cells density.

ii. $f_s(u, v)$ depends on both OV and ECM, and the dependence is linear:

$$f_s(u, v) = u + v + 1. \tag{4.15}$$

In Figure 4.15 we show the evolution of the total tumour mass (for the baseline parameters listed in Table (4.1)) over 100 micro-macro stages. We compare the baseline dynamics generated by model (4.10) (case (a) described by the red curve) with the dynamics generated by model (4.13)+(4.14) (case (b) described by the blue curve), and by model (4.13)+(4.15) (case (c) described by the green curve). Overall, the model with the density-dependent syncytia diffusion shows less tumour growth and smaller tumour invasion area during the later stages of tumour dynamics compared with the baseline model (with constant diffusion). This tumour reduction can

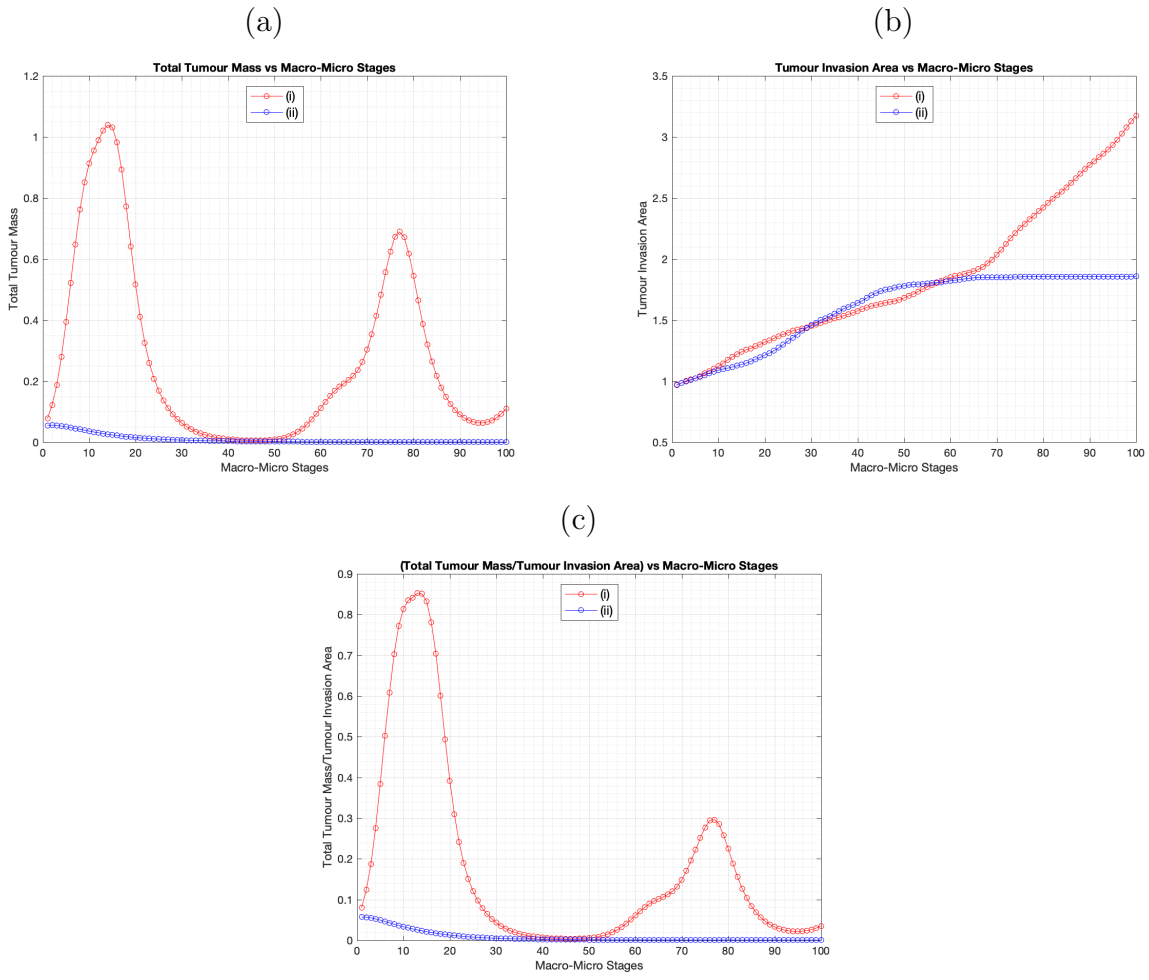

Figure 4.13: (a) Comparison of total tumour masses evolution over macro-micro stages 1 – 100 for the macro-dynamics case (4.10). (b) Comparison of tumour invasion area over macro-micro stages 1 – 100 for the macro-dynamics case (4.10). (c) Comparison of the evolution of the ratio of total tumour masses to tumour invasion area over macro-micro stages 1 – 100 for the macro-dynamics case (4.10). (i) baseline parameter values as listed in Table 4.1; (ii) parameter values for improved anti-tumour therapy as listed in Table 4.3.

be explained by the fact that syncytia diffusion (which depends on OV and ECM spatial distribution) leads to the accumulation of syncytia structures in areas with uninfected and infected tumour cells (the infected tumour cells releasing more OV), which ultimately causes more tumour destruction. We also note that there is no significant difference between the model dynamics with f_s described by either equations

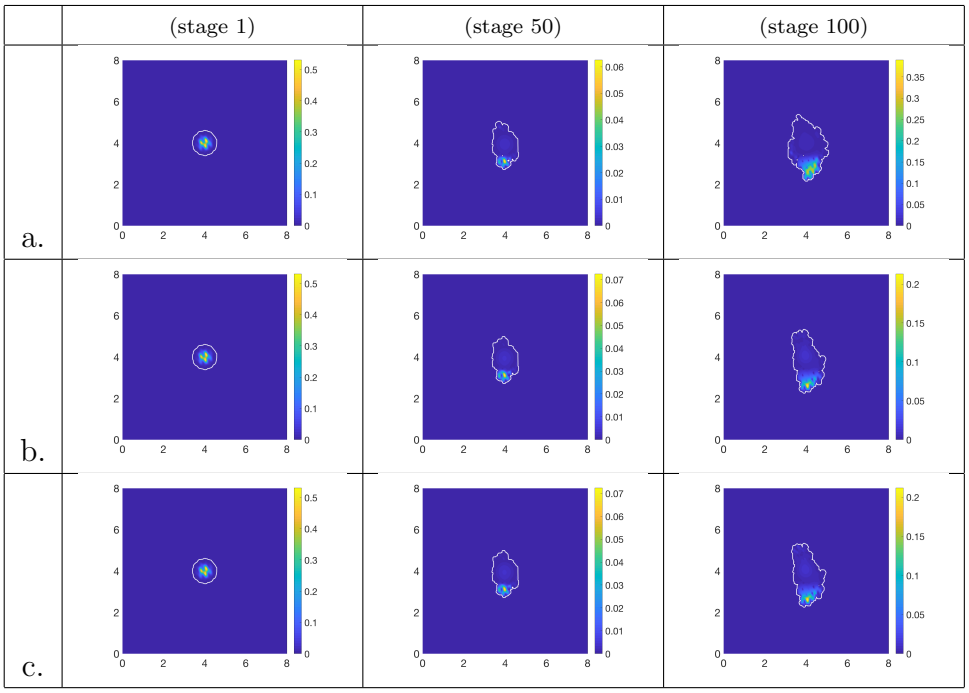

Figure 4.14: Multi-scale simulation results for macro-dynamics systems (4.10) (panels (a)), (4.13)+(4.14) (panels (b)), and (4.13)+(4.15) (panels (c)), for the baseline parameter values from Table 4.1. All figures show the total tumour distribution at three macro-micro stages: 1, 50 and 100.

(4.14) or (4.15). For a visual description of the effect of density-dependent syncytia diffusion on the spatial distribution of total tumour (uninfected+infected+syncytia cells) at different micro-macro simulation stages please see Figure 4.14.

4.5 Summary and Discussions

In this study, we extended a multi-scale moving boundary model for oncolytic cancer virotherapy introduced in Alzahrani et al. (2019), by considering a fusogenic virus that can form syncytia structures (which have been shown experimentally to improve tumour reduction and control Krabbe and Altomonte (2018); Ebert et al. (2004)). The presence of syncytia not only changes the macro-dynamics with respect to the cases studied in Alzahrani et al. (2019), but given the link across the scales

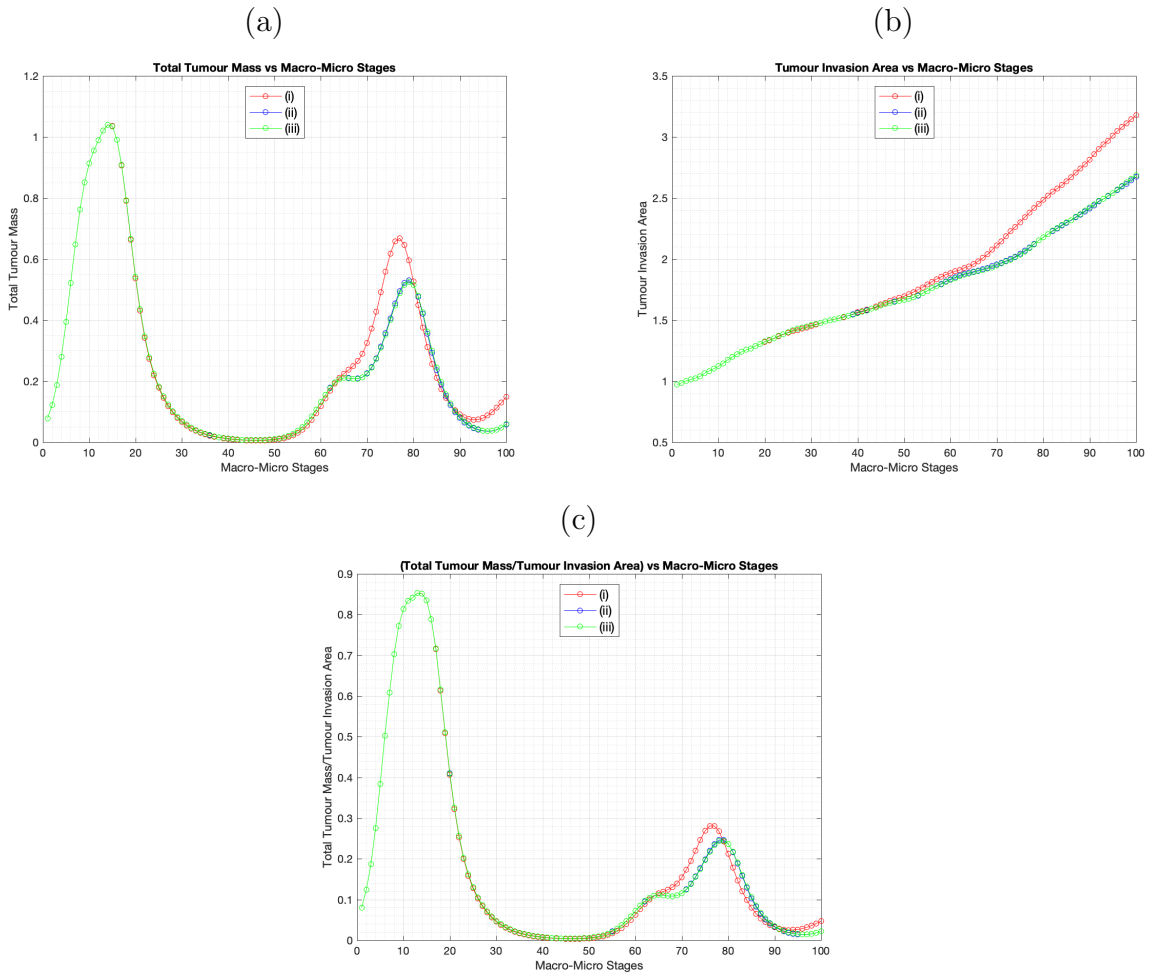

Figure 4.15: Comparison between the dynamics of the baseline model (4.10) (red curve labeled (i)) and the generalised model (4.13) (blue curve labeled (ii) for sub-case (4.14), and green curve labeled (iii) for sub-case (4.15)). (a) The evolution of total tumour mass (uninfected+infected+syncytia cells) over macro-micro stages 1 – 100. (b) The evolution of tumour invasion area over macro-micro stages 1 – 100. (c) The evolution of the ratio of total tumour masses to tumour invasion area over macro-micro stages 1 – 100 for the macro-dynamics case (4.13). All simulations have been performed using the baseline parameter values from Table 4.1.

(from macro to micro) detailed in Section 4.2.2 that involves this time also the syncytia cells, this also influences the micro-dynamics of the proteolytic activity that takes place along the tumour invasive edge. In turn, this altered proteolitic micro-dynamics has direct impact upon the progression of the tumour as well as

upon the changes of its morphology, leading to a different tumour behaviour than the one observed in Alzahrani et al. (2019). Further, we used this new multiscale model to investigate various hypotheses regarding the movement of these syncytia and their interactions with the tumour microenvironment across different scales. The macroscale interactions focused on the dynamics of (infected and uninfected) cancer cells, syncytia structures, virus particles and the surrounding extracellular matrix (ECM), while the microscale interactions focused on the degradation of ECM by enzymes produced by the tumour cells (see Figure 4.2).

Using a computational approach, we investigated different assumptions regarding the macroscale dynamics of syncytia structures: from the anti-tumour/pro-tumour effects of various diffusive and advective abilities of syncytia (see Figures 4.3-4.6), to the anti-tumour/pro-tumour effects of different probabilities of syncytia forming (see Figures 4.7-4.10). The results suggested that lower syncytia motility compared to single infected cells (i.e., $D_s < D_i$, and $\eta_s < \eta_i$) could lead to better anti-tumour outcomes. Moreover, higher probabilities (p_0) of fusogenic viruses failing to form syncytia seemed to lead to better anti-tumour outcomes. These results were likely caused by the specific baseline parameter values listed in Table 4.1, which were chosen to match the parameter values from Alzahrani et al. (2019).

To explain these unexpected results, we also investigated the combined effect of syncytia-forming probability and different death rates for the infected cells and syncytia (δ_i, δ_s), as well as different virus burst rates for the infected cells and syncytia (b_i, b_s); see Figure 4.11. The results suggested that more realistic parameter values (i.e., $b_s > b_i$, $\delta_s < \delta_i$, and $p_0 = 0.25 \Rightarrow (1 - p_0) = 0.75$) lead to better anti-tumour outcomes compared to the baseline case. We also investigated the effect of decreasing the values of some parameters associated with the proteolytic enzymes (i.e., lower enzymatic transport across tumour interface), and observed that this lead

to a slower tumour invasion and faster tumour elimination by the infected cells and syncytia; see Figures 4.12 - 4.13. We can conclude from our previous results that the outcome of the oncolytic therapy does not depend only on various macroscopic cell and virus particle dynamics, but also on the microscopic dynamics of enzymes involved in ECM degradation.

Panels (a) of Figures 4.5, 4.6, 4.10, 4.11 and 4.13 suggest that between the macro-micro stages 40 and 50 the tumour mass becomes very small. This would suggest that there is the possibility of tumour extinction by oscillations (see, although in another context, Caravagna et al. (2010); Donofrio (2010)). However, our model is deterministic, and as such it cannot capture: i) stochastic behaviours when the tumour mass is very small; ii) extrinsic stochastic fluctuations. Some extrinsic sources such as cell-to-cell fluctuations of transcription factors are a delicate matter in tumour modelling, (see (Donofrio, 2008, 2013)), due to that those variations in cells factor lead to fluctuations of the transcription and translation rates in the model parameters.

Finally, given that the syncytia structures are very large, their movement might be impacted by the density of ECM and/or the density of fusogenic virus particles. Thus, we investigated numerically the possibility that the random motility of these syncytia is not constant but depends on these densities (see equations (4.13)-(4.15)). The results in Figures 4.14 - 4.15 suggested that the assumption of density-dependent syncytia diffusion (versus constant diffusion) can impact the outcome of the oncolytic therapy. For the baseline parameter values shown in Table 4.1 the density-dependent diffusion lead to lower long-term tumour sizes and smaller tumour invasion areas, since the ECM density stopped the fast spread of syncytia, thus allowing the viruses to be more successful at killing the tumour cells.

A global multiscale analysis for this multiscale moving-boundary framework in its

entirety remains an open problem. However, questions regarding the local existence and uniqueness of the macro- and micro-dynamics, while exploring the top-down link in between, are currently in preparation and form the subject of a separate work. Finally, on the numerical side, while discussions and early tests concerning of the robustness have been successfully carried out in Trucu et al. (2013) where this multiscale moving boundary framework has been initially introduced, further investigations are still needed to establish an overall multiscale numerical consistency concept for this multiscale computational platform in its entirety.

We conclude this discussion by emphasising that while cell-fusion events are very important in cell biology (in both health and disease), their roles on the spread of viral infections are not always fully understood Compton and Schwartz (2017). In this study we formulated and tested computationally some hypotheses regarding the importance of various syncytium-related parameters on the spread of oncolytic viral infection and tumour reduction/elimination. One major limitation is the lack of experimental data to validate the modelling. It is however our hope that the hypotheses formulated in this paper will stimulate suitable biological experimental work that would challenge to validate our computational findings. Thus, the next step would be to combine this multiscale moving-boundary mathematical framework with *in vitro* or *in vivo* experiments for oncolytic viral therapies for cancer (see, for example, the spatial data from Kemler et al. (2019) on oncolytic virus spread), to try to approximate some parameter ranges and thus to make better predictions on possible treatment outcomes.

Chapter 5

Local Existence and Uniqueness of Solutions for Selected Macro-Micro Modelling of Cancer Response to Oncolytic Viral Therapy

5.1 Introduction

The main contribution of this chapter is to study the local existence and uniqueness of solutions for both macroscopic and microscopic models previously introduced in Chapter 3. In order to achieve that, we mainly adopt the approach and terminology introduced in Rodrigo (2008); Szymanska et al. (2009); Chaplain et al. (2011); Bitsouni et al. (2017) for similar mathematical models. However, the proof of local existence given in each work differs from each other in terms of proof methodology

and setting assumptions. For instance, the mechanism of the given proof in Rodrigo (2008) adopts a classical settings to show the local existence by Schauder's fixed point theorem, while in Szymanska et al. (2009) the theory of semigroups has been adopted to prove the existence of solutions locally in time by using Banach fixed point theorem. Furthermore, the presented mathematical models in Chaplain et al. (2011); Bitsouni et al. (2017) are based on systems of integro-differential equations (nonlocal integral) with appropriate kernels describing the spatial ranges for certain proposed cases, hence, their assumed spacial properties would differ from each other as well. However, generally they follow the same proof strategy to show that there is a local solution uniquely existed within a certain proposed space and a fixed time.

In order to show the existence of solutions for our model, we apply similar steps as in Rodrigo (2008); Szymanska et al. (2009); Chaplain et al. (2011); Bitsouni et al. (2017), which will ultimately enable us to use the Banach contraction theorem. In brief, we aim to show that inside a carefully chosen ball within an appropriately constructed function space naturally induced by our problems, we ensure that the solution of the PDE system exists and is unique. This will be achieved via a Banach Contraction Mapping argument. Indeed, in order to obtain that, we first rewrite the system in a general functional form that respects the assumptions and initial and boundary conditions of our problem. Then we will apply the classical semigroup framework (Henry, 1981) including space embeddings for Holder space of continuous functions. Finally, based on some essential mathematical concepts (including the sectorial operator, the lipschitzianity properties of our system, the triangle inequality, the continuity of the norm, the approximation of the Lebesgue and Bochner Integrals by sequences of step functions (Yosida, 1995)), we show that there exists a unique solution locally-in time within a certain proposed space for our model. Furthermore, we use similar technique to show the existence of solutions for

two macro-dynamics scenarios previously presented in section 3.3, namely, scenario (1) and scenario (3), in addition to the microscopic dynamics previously derived in section 3.4.

5.2 Local Existence and Uniqueness of Macroscopic Model 1.

In this section, we aim to study the existence and uniqueness locally-in-time of solution for the macroscopic model previously introduced in Alzahrani et al. (2019) and already explained in section 3.3. However, recall the macroscopic model as following:

$$\begin{cases} \frac{\partial c}{\partial t} = D_c \Delta c - \eta_c \nabla \cdot (c \nabla u) + \mu_1 c(1-c) - \rho c v, \\ \frac{\partial i}{\partial t} = D_i \Delta i + \rho c v - \delta_i i, \\ \frac{\partial u}{\partial t} = -u(\alpha_c c + \alpha_i i) + \mu_2 u(1-u-c-i), \\ \frac{\partial v}{\partial t} = D_v \Delta v + b i - \rho c v - \delta_v v. \end{cases} \tag{5.1}$$

Here and before setting up the local existence theorem, we start with some basic assumptions. To that end, since we deal with biological spatio-temporally distributed entities, the rates for random motility, logistic growth, death, and viral replication are naturally assumed to be positive i.e. $D_c, D_i, D_v, \mu_1, \mu_2, \delta_i, \delta_v, b \geq 0$. In addition to that, for simplicity, as proposed previously in Szymanska et al. (2009); Chaplain et al. (2011); Bitsouni et al. (2017), we define new general functions in terms of rewriting our model in a general form, namely:

$f_{1,1}(c,u)$ to describe non-local directionality corresponding to biased movement against ECM gradients (acquired due to ECM degradation), i.e. $f_{1,1}(c,u) \geq 0$;

$f_{1,2}(c)$ to be a general positive function describing the cancer cells proliferation

rate;

$f_{1,3}(c, v)$ to be a general positive function representing the rate of infection;

$f_{3,1}(c, i)$ and $f_{3,2}(c, i, u)$ concern the remodelling process of ECM, with the first function $f_{3,1}(c, i)$ describing a general form of ECM degradation, while $f_{3,2}(c, i, u)$ is representing a general ECM growth law with respect to c, i, u.

Thus, a generalised form of the macroscopic dynamics 5.1 on a bounded domain $\Omega \subset \mathbb{R}^n$ over the time interval $(0, \Delta T)$ is therefore obtained as:

$$\begin{cases} \frac{\partial c}{\partial t} = D_c \Delta c - \nabla \cdot (c f_{1,1}(c, u)) + c f_{1,2}(c) - f_{1,3}(c, v), \\ \frac{\partial i}{\partial t} = D_i \Delta i + f_{1,3}(c, v) - \delta_i i, \\ \frac{\partial u}{\partial t} = -u f_{3,1}(c, i) + u f_{3,2}(c, i, u), \\ \frac{\partial v}{\partial t} = D_v \Delta v + bi - f_{1,3}(c, v) - \delta_v v. \end{cases} \tag{5.2}$$

with the following initial conditions:

$$\begin{aligned} &c(0, x) = c_0(x) \geq 0, \;\; i(0, x) = i_0(x) \geq 0, \\ &u(0, x) = u_0(x) \geq 0, \;\; v(0, x) = v_0(x) \geq 0, \;\; \text{in } \Omega. \end{aligned} \tag{5.3}$$

We assume that there is no-flux passing through the smooth boundary $\partial\Omega$ for all cancer cells type (c, i) and ECM (u) as well as virus particles (v) i.e.

$$\langle \nabla c, \nu \rangle = \langle \nabla i, \nu \rangle = \langle \nabla v, \nu \rangle = 0 \;\text{ on }\; (0, \infty) \times \partial\Omega, \tag{5.4}$$

where ν is the normal outward unit for vector field to $\partial\Omega$ enhanced with the following condition regarding haptotactic motility:

$$\langle \nabla f_{1,1}(c, u), \nu \rangle = 0 \;\text{ on }\; (0, \infty) \times \partial\Omega. \tag{5.5}$$

Now, we propose a non-local mapping on the function $f_{1,1}(c, v)$ such that:

$$f_{1,1} : \mathcal{C}(\overline{\Omega} : \mathbb{R}) \times \mathcal{C}(\overline{\Omega} : \mathbb{R}) \mapsto \mathcal{C}^{1,\beta}(\overline{\Omega} : \mathbb{R}^n), \;\; \beta \in (0, 1], \tag{5.6}$$

where $\mathcal{C}$ represents the space of continuous functions and

$$f_{1,1}(c, u)(x) = \int_{\Omega} f^*_{1,1}(x, y, c(y), u(y))dy, \;\; \text{for } \; (c, u) \in \mathcal{C}(\overline{\Omega} : \mathbb{R}) \times \mathcal{C}(\overline{\Omega} : \mathbb{R}), \tag{5.7}$$

where $f^*_{1,1}$ is a continuous function over the following map:

$$f^*_{1,1} : \Omega^2 \times \mathbb{R}^2 \mapsto \mathbb{R}^n, \tag{5.8}$$

satisfying the following properties:

$$\begin{aligned} &f^*_{1,1}(x, y, 0, 0) = 0 \;\text{ for }\; (x, y) \in \Omega, \\ &f^*_{1,1}(\cdot, y, \gamma, \gamma^*) \in \mathcal{C}^{1,\gamma}(\overline{\Omega} : \mathbb{R}^n) \;\text{ for }\; y \in \Omega \;\text{ and }\; (\gamma, \gamma^*) \in \mathbb{R}^2. \end{aligned} \tag{5.9}$$

Furthermore, $f^*_{1,1}$ is assumed to satisfy the following assumption:
we have that there exists a constant $L_{f_{1,1}}$ such that, for any $(\gamma_1, \gamma^*_1), (\gamma_2, \gamma^*_2) \in \mathbb{R}^2$, the following inequality holds

$$\begin{aligned} |f^*_{1,1}(x, y, \gamma_1, \gamma^*_1) - f^*_{1,1}(x, y, \gamma_2, \gamma^*_2)| + |\partial_x f^*_{1,1}(x, y, \gamma_1, \gamma^*_1) - \partial_x f^*_{1,1}(x, y, \gamma_2, \gamma^*_2)| \\ \leq L_{f_{1,1}}(|\gamma_1 - \gamma_2| + |\gamma^*_1 - \gamma^*_2|). \end{aligned} \tag{5.10}$$

uniformly with respect to $(x, y) \in \Omega^2$. Now, for the remaining general functions; $f_{1,2}, f_{1,3}, f_{3,1}$ and $f_{3,2}$, we have the following assumptions based on what has been already shown in Chaplain et al. (2011) with additional consideration all of them

are locally Lipschitz functions, namely:

$$\begin{aligned} &f_{1,2}(c) : \mathbb{R} \mapsto \mathbb{R}, \\ &f_{1,3}(c, v) : \mathbb{R} \times \mathbb{R} \mapsto \mathbb{R}, \\ &f_{3,1}(c, i) : \mathbb{R} \times \mathbb{R} \mapsto \mathbb{R}, \\ &f_{3,2}(c, i, u) : \mathbb{R} \times \mathbb{R} \times \mathbb{R} \mapsto \mathbb{R}. \end{aligned} \tag{5.11}$$

Moreover; since c and v are continuous, then their image of Ω through these functions are compact and so the product of the images will be a compact set in $\mathbb{R}^2$, hence the given Lipschitz condition on $f_{1,3}$, we can always identify two positive constants A and B such that:

$$f_{1,3}(c, v) \leq A - Bc. \tag{5.12}$$

5.2.1 Preliminary setup and notations

For convenience, we would like to rewrite the system 5.2 in the following order:

$$\frac{\partial c}{\partial t} - D_c \Delta c = -\nabla c \cdot f_{1,1}(c, u) - c(\nabla \cdot f_{1,1}(c, u)) + c(1 + f_{1,2}(c)) - f_{1,3}(c, v) \tag{5.13}$$

$$\frac{\partial i}{\partial t} - D_i \Delta i + \delta_i i = f_{1,3}(c, v), \tag{5.14}$$

$$\frac{\partial u}{\partial t} = -u f_{3,1}(c, i) + u f_{3,2}(c, i, u), \tag{5.15}$$

$$\frac{\partial v}{\partial t} - D_v \Delta v + \delta_v v = bi - f_{1,3}(c, v). \tag{5.16}$$

Here, we consider the following operators:

$$\begin{aligned} S_1 &= -D_c\Delta c + 0I, \\ S_2 &= -D_i\Delta i + \delta_i I, \\ S_3 &= -D_v\Delta v + \delta_v I, \end{aligned} \tag{5.17}$$

where I is the identity operator. In Lebesgue space $X = L^p(\Omega)$, we have a common domain of the operators S_j where the real part of the spectrum of S_j is positive, i.e., $Re(\sigma(S_j)) > 0$, where $j = 1, 2, 3$. The domain of each S_j is denoted by $D(S_j)$ and is given by

$$D(S_j) := \{z \in W^{2,p} : \partial_\nu z|_{\partial\Omega} = 0\}, \tag{5.18}$$

where $W^{2,p}$ represents Sobolev space of all p^{th} integrable functions belonging to L^p whose weak derivatives up to order ≤ 2.

Now, for each S_j (the sectorial operator), then $-S_j$ is the infinitesimal generator of the analytic semigroup $\{e^{-tS_j}\}_{t\geq 0}$ (Henry, 1981). Thus, the Banach space of fractional powers is denoted by:

$$X^\zeta := D(S_j^\zeta), \tag{5.19}$$

where $j = 1, 2, 3$, the exponent $\zeta \in (0, 1)$, and $D(S_j^\zeta)$ represents the domain of S_j^ζ, with its graph norm being defined as in Henry (1981), namely: for any $x^* \in X^\zeta$, we have

$$||x^*||_{X^\zeta} := ||S_j^\zeta x^*||_X. \tag{5.20}$$

Following Henry (1981) again, we obtain that for any $\zeta \in (0, 1)$ we have

$$D(S_j) \subset X^\zeta \subset X \tag{5.21}$$

Further, we define the space

$$Y = X \times X \times W^{1,p}(\Omega) \times X, \tag{5.22}$$

which is equipped with the maximum norm

$$\begin{aligned} ||y||_Y &:= \max(||y_1||_X, ||y_2||_X, ||y_3||_{W^{1,p(\Omega)}}, ||y_4||_X) \\ &\qquad \text{for } \ y = (y_1, y_2, y_3, y_4) \in Y. \end{aligned} \tag{5.23}$$

Furthermore, Y^ζ denotes the space

$$Y^\zeta := X^\zeta \times X^\zeta \times W^{1,p}(\Omega) \times X^\zeta.$$

and via (5.21) we observe that this is included in Y, i.e.,

$$Y^\zeta \subset Y,$$

and so this is naturally equipped with the induced maximum norm

$$\begin{aligned} ||\cdot||_{Y^\zeta} &:= ||\cdot||_Y \Big/_{Y^\zeta} \\ &i.e., \\ ||y||_{Y^\zeta} &:= ||y||_Y \\ &= \max(||y_1||_X, ||y_2||_X, ||y_3||_{W^{1,p}(\Omega)}, ||y_4||_X) \\ &\qquad \text{for } \ y = (y_1, y_2, y_3, y_4) \in Y^\zeta. \end{aligned} \tag{5.24}$$

Finally, for an arbitrary time $T > 0$, we denote by

$$Y_T^\zeta = \mathcal{C}([0, T] : Y^\zeta), \tag{5.25}$$

endowed with the usual uniform norm

$$||y||_{Y_T^\zeta} := \sup_{s\in[0,T]} ||y(s)||_{Y^\zeta}, \tag{5.26}$$

Moreover, within the classical semigroup frameworks, Theorem 1.4.3 in Henry (1981) (page 26) shows that there exists a positive constant $C_\zeta > 0$ such that the following inequality holds:

$$||S_j^\zeta e^{-S_j t} z||_X \leq C_\zeta t^{-\zeta} e^{-\zeta_j^* t} ||z||_X, \text{ for } z \in X \tag{5.27}$$

where $0 < -\zeta_j^* < Re(\sigma(S_j))$, in parallel with,

$$||S_j^\zeta e^{-S_j t} z||_X \leq k_\zeta ||z||_{X^\zeta}, \text{ for } z \in X^\zeta. \tag{5.28}$$

where k_ζ is a positive constant.
In addition to 5.27 and 5.28, we have that also the following embedding holds true, namely:

$$X^\zeta \subset W^{1,p}(\Omega) \text{ for } \zeta > \frac{1}{2}, \tag{5.29}$$

$$X^\xi \subset \mathcal{C}^{0,q}(\overline{\Omega}) \text{ for } \frac{q}{2} + \frac{n}{2p} < \zeta < \frac{1}{2} + \frac{n}{2p}, \ q \in (0,1), \tag{5.30}$$

where $\mathcal{C}^{0,q}(\overline{\Omega})$ represents the space of all Holder continuous functions with q as an exponent value. Moreover,

$$\text{for any } \zeta \in (\frac{1}{2}, \frac{1}{2} + \frac{1}{2p}), \text{ when } p > n, \tag{5.31}$$

the given embeddings (5.29) and (5.30) are achieved.

Theorem 5.2.1 (Local Existence) *Assume that the initial conditions c_0, i_0 and*

$v_0 \in X^\zeta$ and $u_0 \in W^{1,p}(\Omega)$ are satisfied with all previous assumptions, then for any $T > 0$, the macroscopic model 5.13-5.16 has a unique local-in-time solution such that :

$$c, i, v \in \mathcal{C}([0, T) : X^\zeta) \ \textit{and} \ u \in \mathcal{C}([0, T) : W^{1,p}(\Omega)).$$

In addition, for $t > 0$, c, i and v are classical solutions and

$$sup(||c||_\infty + ||i||_\infty + ||u||_\infty + ||v||_\infty) < \infty.$$

Proof: In this proof, we follow similar steps as in Szymanska et al. (2009); Chaplain et al. (2011); Bitsouni et al. (2017), which will ultimately enable us to use the Banach contraction theorem to show the local existence of the solution for the macro-scale model 5.13-5.16.

Further, we recall that, from our previous assumptions, we already know that $c, i, v \in W^{1,p}(\Omega)$ as shown in the embedding 5.29 as well as each function of the general functions $f_{1,2}, f_{1,3}, f_{3,1}, f_{3,2}$ is a locally Lipschitz function, then by superposition property, we obtain $f_{1,2}, f_{1,3}, f_{3,1}, f_{3,2} \in W^{1,p}(\Omega)$. Thus, in the case when $p > n$, exploring the algebra structure with point-wise multiplication of $W^{1,p}(\Omega)$, the right hand side of 5.15 can be re-expressed in the form of the mapping

$$\begin{aligned} &F^* : Y^\zeta \longmapsto W^{1,p}(\Omega), \\ &\text{given by} \\ &F^*(c, i, u, v) := -u f_{3,1}(c, i) + u f_{3,2}(c, i, u), \end{aligned} \tag{5.32}$$

which is a locally Lipschitz mapping, as both $f_{3,1}$, $f_{3,2}$ and u are locally Lipschitz functions.

Furthermore, denoting now

$$r := \begin{pmatrix} c \\ i \\ u \\ v \end{pmatrix}, \qquad and \qquad S := \begin{pmatrix} S_1 & 0 & 0 & 0 \\ 0 & S_2 & 0 & 0 \\ 0 & 0 & 0 & 0 \\ 0 & 0 & 0 & S_3 \end{pmatrix}, \tag{5.33}$$

and rewriting also the right-hand side of 5.13 - 5.14 and 5.16 as the mappings

$$F_1, F_2, F_3 : Y^{\zeta} \longmapsto X$$

given by

$$\begin{aligned} F_1(c,i,u,v) &:= -\nabla c \cdot f_{1,1}(c,u) - c(\nabla \cdot f_{1,1}(c,u)) + c(1 + f_{1,2}(c)) - f_{1,3}(c,v), \\ F_2(c,i,u,v) &:= f_{1,3}(c,v), \\ F_3(c,i,u,v) &:= bi - f_{1,3}(c,v). \end{aligned} \tag{5.34}$$

we can then rewrite the entire system as

$$\begin{aligned} &\tfrac{dr}{dt} = Sr + (F_1(r), F_2(r), F^*(r), F_3(r))^T, \quad in \quad \Omega_T, \\ &r(0) := (c_0, i_0, u_0, v_0)^T, \quad in \quad \Omega_T. \end{aligned} \tag{5.35}$$

In this context, to complete the proof, we consider the map $P := (P_1, P_2, P_3, P_4)$, namely

$$P : Y_T^{\zeta} \mapsto Y_T^{\zeta}$$

given by

$$\begin{cases} P_1((c,i,u,v)(t)) := e^{-S_1 t}c_0 + \int_0^t e^{-S_1(t-s)}F_1(c(s),i(s),u(s),v(s))\mathrm{ds}, \\ P_2((c,i,u,v)(t)) := e^{-S_2 t}i_0 + \int_0^t e^{-S_2(t-s)}F_2(c(s),i(s),u(s),v(s))\mathrm{ds}, \\ P_3((c,i,u,v)(t)) := u_0 + \int_0^t F^*(c(s),i(s),u(s),v(s))\mathrm{ds}, \\ P_4((c,i,u,v)(t)) := e^{-S_3 t}v_0 + \int_0^t e^{-S_3(t-s)}F_3(c(s),i(s),u(s),v(s))\mathrm{ds}, \end{cases} \tag{5.36}$$

for which we will show in the following that for an appropriately small T, there exists a fixed point.

In order to achieve this, we proceed as follows. First, for an arbitrary $T > 0$, we consider the ball $B_{Y_T^\zeta}(0,R) \subset Y_T^\zeta$

$$B_{Y_T^\zeta}(0,R) = \{y \in Y_T^\zeta : ||y||_{Y_T^\zeta} \leq R\}, \tag{5.37}$$

with the radius $R > 0$ being chosen such that

$$\begin{aligned} &\max(||c_0||_{X^\zeta} + ||i_0||_{X^\zeta} + ||v_0||_{X^\zeta}) < \tfrac{R}{2k_\zeta}, \\ &\max(||u_0||_{W^{1,p}(\Omega)}) < \tfrac{R}{2}, \end{aligned} \tag{5.38}$$

where $(c_0, i_0, u_0, v_0) \in Y^\zeta$ and k_ζ satisfy the property 5.28. Using the Lipschitzianity property of each of the functions F_1, F_2, F_3, F^*, we obtain there exists a constant that depends only on the radius R, namely $M_R > 0$, such that

$$\sup_{y \in B_{Y_T^\zeta}(0,R)} \sup_{s\in[0,T]} ||(F_1(y(s)), F_2(y(s)), F^*(y(s)), F_3(y(s)))||_Y < M_R. \tag{5.39}$$

which is completely proved in Lemma 5.2.2.

We aim now to show that for a small enough time $T > 0$ (which will be appropriately chosen below) the mapping $P := (P_1, P_2, P_3, P_4)$ will be a contraction on

$B_{Y_T^\zeta}(0,R)$. For that purpose, let $T>0$ and let $(c,i,u,v)\in B_{Y_T^\zeta}(0,R)$ be arbitrarily considered. For the first operator P_1, from 5.36, we have that

$$||P_1(c,i,u,v)(t)||_{X^\zeta} = ||e^{-S_1 t}c_0 + \int_0^t e^{-S_1(t-s)}F_1(c(s),i(s),u(s),v(s))\mathrm{ds}||_{X^\zeta}, \tag{5.40}$$

then using the triangle inequality we obtain:

$$||P_1(c,i,u,v)(t)||_{X^\zeta} \leq ||e^{-S_1 t}c_0||_{X^\zeta} + ||\int_0^t e^{-S_1(t-s)}F_1(c(s),i(s),u(s),v(s))\mathrm{ds}||_{X^\zeta}, \tag{5.41}$$

Furthermore, using (5.20) the norm $||e^{-S_1 t}c_0||_{X^\zeta}$ can be re-expressed as

$$||e^{-S_1 t}c_0||_{X^\zeta} = ||S_1^\zeta x^*||_X \tag{5.42}$$

and so using the inequality 5.28, we get:

$$\begin{aligned} ||e^{-S_1 t}c_0||_{X^\zeta} &= ||S_1^\zeta x^*||_X \\ &\leq k_\zeta ||c_0||_{X^\zeta} \end{aligned} \tag{5.43}$$

which finally leads us to

$$||P_1(c,i,u,v)(t)||_{X^\zeta} \leq k_\zeta ||c_0||_{X^\zeta} + ||\int_0^t e^{-S_1(t-s)}F_1(c(s),i(s),u(s),v(s))\mathrm{ds}||_{X^\zeta}. \tag{5.44}$$

For the second norm on the right hand side of inequality (5.44) using the triangle inequality property and the continuity of the norm combined with the property of the Lebesgue integral as being the limit of a sequence of integrals (in the sense of

operator Bochner Integral (Yosida, 1995)) of simple (step) functions

$$\begin{aligned}\psi_n \;:=\; & \sum_{j=1}^{k_n} a_j^n \chi_{A_j^n} \nearrow e^{-S_1(t-s)} F_1(c(s), i(s), u(s), v(s)), \\ & \text{for appropriate operator coefficients } \{a_j^n\}_{j=1\ldots k_n} \\ & \text{and } \{A_j^n\}_{j=1\ldots k_n} \text{ Borel } \sigma- \text{ algebra of } [0,T], \text{ for all } n \in \mathbb{N},\end{aligned}$$

we obtain that

$$\begin{aligned}||\int_0^t e^{-S_1(t-s)} F_1(c(s),i(s),u(s),v(s))\mathrm{ds}||_{X^\zeta} &\leq ||\lim_{n\to\infty} \sum_{j=1}^{k_n} a_j^n \chi_{A_j^n}||_{X^\zeta} \\ &= \lim_{n\to\infty} ||\sum_{i=1}^{k_n} a_j^n \chi_{A_j^n}||_{X^\zeta} \\ &\leq \lim_{n\to\infty} \sum_{i=1}^{k_n} ||a_j^n \chi_{A_j^n}||_{X^\zeta} \\ &\leq \lim_{n\to\infty} \sum_{i=1}^{k_n} ||a_j^n||_{X^\zeta} \chi_{A_j^n} \\ &= \int_0^t ||e^{-S_1(t-s)} F_1(c(s),i(s),u(s),v(s))||_{X^\zeta} ds\end{aligned} \tag{5.45}$$

Therefore, using now inequalities (5.27) and (5.38), from (5.45) we obtained that

$$\begin{aligned}||\int_0^t e^{-S_1(t-s)} F_1(c(s),i(s),u(s),v(s))\mathrm{ds}||_{X^\zeta} &\leq \int_0^t ||e^{-S_1(t-s)} F_1(c(s),i(s),u(s),v(s))||_{X^\zeta} ds \\ &\leq M_R \int_0^T C_\zeta (t-s)^{-\zeta} e^{-\zeta_1^*(t-s)} \mathrm{ds}\end{aligned} \tag{5.46}$$

Hence we get the following estimate for the norm of P_1, namely:

$$\begin{aligned}||P_1(c,i,u,v)(t)||_{X^\zeta} &\leq k_\zeta ||c_0||_{X^\zeta} + M_R \int_0^T C_\zeta (t-s)^{-\zeta} e^{-\zeta_1^*(t-s)} \mathrm{ds} \\ &\leq \tfrac{R}{2} + M_R \tfrac{C_\zeta T^{1-\zeta}}{1-\zeta}.\end{aligned} \tag{5.47}$$

Proceeding now in a similar manner also for the operators P_2 and P_4 (by following an identical sequence of steps as those described in equations (5.40)-(5.47)), we obtain

for these the following estimates, namely:

$$||P_2(c,i,u,v)(t)||_{X^\zeta} \leq \frac{R}{2} + M_R \frac{C_\zeta T^{1-\zeta}}{1-\zeta}. \tag{5.48}$$

and

$$||P_4(c,i,u,v)(t)||_{X^\zeta} \leq \frac{R}{2} + M_R \frac{C_\zeta T^{1-\zeta}}{1-\zeta}. \tag{5.49}$$

On the other hand, for the remaining operator P_3, based on (5.38) and (5.39), we obtain:

$$\begin{aligned}
||P_3(c,i,u,v)(t)||_{W^{1,p(\Omega)}} &= ||u_0 + \int_0^t F^*(c(s),i(s),u(s),v(s))\mathrm{ds}||_{W^{1,p(\Omega)}} \\
&\leq ||u_0||_{W^{1,p(\Omega)}} + ||\int_0^t F^*(c(s),i(s),u(s),v(s))\mathrm{ds}||_{W^{1,p(\Omega)}} \\
&\leq \frac{R}{2} + \int_0^t ||F^*(c(s),i(s),u(s),v(s))||_{W^{1,p(\Omega)}}\mathrm{ds} \\
&\leq \frac{R}{2} + \int_0^t \sup_{y \in B_{Y_T^\zeta}(0,R)} ||(F_1(y),F_2(y),F^*(y),F_3(y))||_{Y^\zeta}\mathrm{ds} \\
&\leq \frac{R}{2} + \int_0^t M_R ds \\
&\leq \frac{R}{2} + M_R T
\end{aligned} \tag{5.50}$$

Thus, by choosing now a small enough $T > 0$ such that

$$\{M_R \frac{C_\zeta T^{1-\zeta}}{1-\zeta}, M_R T\} \leq \frac{R}{2}. \tag{5.51}$$

we obtain that indeed

$$||(P_1((c,i,u,v)(t)), P_2((c,i,u,v)(t)), P_3((c,i,u,v)(t)), P_4((c,i,u,v))(t))||_{Y^\zeta} \leq R$$

$$\forall t \in [0,T]$$

hence

$$||(P_1(c,i,u,v),P_2(c,i,u,v),P_3(c,i,u,v),P_4(c,i,u,v))||_{Y_T^\zeta} \leq R$$

which implies that

$$(P_1(c,i,u,v),P_2(c,i,u,v),P_3(c,i,u,v),P_4(c,i,u,v)) \in B_{Y_T^\zeta}(0,R)$$

and finally leads to

$$(P_1,P_2,P_3,P_4)(B_{Y_T^\zeta}(0,R)) \subset B_{Y_T^\zeta}(0,R).$$

Finally, to show now that the mapping (P_1,P_2,P_3,P_4) is a contraction on $B_{Y_T^\zeta}(0,R)$, let $y_1,y_2 \in B_{Y_T^\zeta}(0,R)$ and an arbitrary $t \in [0,T]$ (with $T>0$ as chosen in (5.51)). Using (5.20) - (5.27), (5.26) and (5.45) combined with the Lipschitzianity of F_1, we obtain that

$$\begin{aligned}
||P_1(y_1)(t)-P_1(y_2)(t)||_{X^\zeta} &\leq \int_0^t ||e^{-S_1(t-s)}(F_1(y_1(s))-F_1(y_2(s)))||_{X^\zeta}\mathrm{ds} \\
&\leq \int_0^T ||e^{-S_1(t-s)}\chi_{t-s>0}(s)(F_1(y_1(s))-F_1(y_2(s)))||_{X^\zeta}\mathrm{ds} \\
&= \int_0^T ||S_1^\zeta e^{-S_1(t-s)}\chi_{t-s>0}(s)(F_1(y_1(s))-F_1(y_2(s)))||_{X}\mathrm{ds} \\
&\leq \int_0^T C_\zeta(t-s)^{-\zeta}e^{\zeta_j^*(t-s)}\chi_{t-s>0}(s)||F_1(y_1(s))-F_1(y_2(s)))||_{X}\mathrm{ds} \\
&\leq \int_0^T C_\zeta(t-s)^{-\zeta}e^{\zeta_j^*(t-s)}\chi_{t-s>0}(s)k_1||y_1(s)-y_2(s)||_{Y^\zeta}\mathrm{ds} \\
&\leq \int_0^T C_\zeta(t-s)^{-\zeta}e^{\zeta_j^*(t-s)}\chi_{t-s>0}(s)k_1||y_1-y_2||_{Y_T^\zeta}\mathrm{ds}. \\
&\leq C_\zeta k_1\left(\int_0^T (t-s)^{-\zeta}e^{\zeta_j^*(t-s)}\chi_{t-s>0}(s)\mathrm{ds}\right)||y_1-y_2||_{Y_T^\zeta}.
\end{aligned} \tag{5.52}$$

Moreover, estimates of the same type as obtained in (5.52) are obtained in a similar fashion for the remaining operators P_2, P_3 and P_4. Thus, choosing an appropriately

small $T > 0$ that makes the right hand side integrals smaller than

$$\frac{1}{2C_\zeta \max\{k_1,k_2,k_3,k^*\}} \quad \text{(with } k_1, k_2, k_3, k^* \text{ being the Lipschitz constants for } F_1, F_2, F^*, F_3\text{)}, \tag{5.53}$$

for any $y_1, y_2 \in B_{Y_T^\zeta}(0, R)$, we obtain that

$$||(P_1, P_2, P_3, P_4)(y_1)(t) - (P_1, P_2, P_3, P_4)(y_2)(t)||_{Y_T^\zeta} \leq \tfrac{1}{2}||y_1 - y_2||_{Y_T^\zeta}. \tag{5.54}$$

Therefore, (P_1, P_2, P_3, P_4) is a contraction that has also the property that

$$(P_1, P_2, P_3, P_4)(B_{Y_T^\zeta}(0, R)) \subset B_{Y_T^\zeta}(0, R).$$

Hence, the restriction

$$(P_1, P_2, P_3, P_4) : B_{Y_T^\zeta}(0, R) \to B_{Y_T^\zeta}(0, R)$$

is a contraction, and as $B_{Y_T^\zeta}(0, R)$ is a complete metric space, via Banach Contraction Theorem (Yosida, 1995), we obtain that indeed there exist a unique point $(c^*, i^*, u^*, v^*) \in B_{Y_T^\zeta}(0, R)$, which is in fact the unique local solution for our system. □

Lemma 5.2.2 *If F^* and F_1, F_2, F_3 defined in* (5.32) *and* (5.34) *are Lipschitz functions, then inequality* (5.39) *holds true.*

Proof: Let us suppose $F_j, (j = 1, 2, 3)$ are Lipschitz functions, then using the definition of the Lipschitzianity we have that there exists $k_j > 0$ such that, for any

$y \in B_{Y_T^\zeta}(0,R)$ and any $s \in [0,T]$, we have that

$$||F_j(y(s)) - F_j(0)||_X \leq k_j ||y(s) - 0||_{Y^\zeta} \leq k_j ||y - 0||_{Y_T^\zeta} \leq k_j R.$$

Therefore, we obtain that $k_j R$ is an upper bound for the set

$$\{||F_j(y(s)) - F_j(0)||_X \,|\, s \in [0,T]\},$$

and so using simply the definition of supremum, we obtain that

$$\sup_{s\in[0,T]} ||F_j(y(s)) - F_j(0)||_X \leq k_j R. \tag{5.55}$$

However, we note that for any $y \in B_{Y_T^\zeta}(0,R)$ we can rewrite the norm of $||F_j(y)||$ as

$$||F_j(y(s))||_X = ||F_j(0) + (F_j(y(s)) - F_j(0))||_X, \quad \forall s \in [0,T]$$

and so we have that

$$||F_j(y(s))||_X \leq ||F_j(0)||_X + ||(F_j(y(s)) - F_j(0)||_X, \quad \forall s \in [0,T],$$

therefore, using (5.55) we obtain that

$$\begin{aligned} ||F_j(y(s))||_X &\leq ||F_j(0)||_X + \sup_{s\in[0,T]} ||F_j(y(s)) - F_j(0)||_X \\ &\leq ||F_j(0)||_X + k_j R, \qquad \forall s \in [0,T]. \end{aligned}$$

Therefore, we have that $||F_j(0)||_X + k_j R$ is an upper bound for the set

$$\{||F_j(y(s))||_X \,|\, s \in [0,T]\},$$

and so using again the definition of the supremum, we obtain that

$$\begin{aligned} \sup_{s\in[0,T]} ||F_j(y(s))||_X &\leq ||F_j(0)||_X + Rk_j \\ &\leq \max_{i=1,2,3} ||F_j(0)||_X + R \max_{i=1,2,3} k_j. \end{aligned} \tag{5.56}$$

for any $y \in B_{Y_T^\zeta}(0,R)$.

Finally, since F^* is also Lipschitz, following identical steps as above, we also obtain that there exists $k^* > 0$ such that for any $y \in B_{Y_T^\zeta}(0,R)$ we have:

$$\sup_{s\in[0,T]} ||F^*(y(s))||_{W^{1,p}} \leq ||F^*(0)||_{W^{1,p}} + k^*R. \tag{5.57}$$

Hence, denoting

$$M_R := \max(\max_{i=1,2,3} ||F_j(0)||_X + R \max_{i=1,2,3} k_j \ , \ ||F^*(0)||_{W^{1,p}} + k^*R), \tag{5.58}$$

from (5.56) and (5.57), we obtain, for any $y \in B_{Y_T^\zeta}(0,R)$, we have that the following inequality holds

$$||(F_1(y(s)), F_2(y(s)), F^*(y(s)), F_3(y(s)))||_Y \leq M_R \qquad \forall s \in [0,T], \tag{5.59}$$

which implies that M_R is an upper bound for the set

$$\{||(F_1(y(s)), F_2(y(s)), F^*(y(s)), F_3(y(s)))||_Y \mid s \in [0,T]\}$$

Therefore, using again the definition of supremum we obtain that

$$\sup_{s\in[0,T]} ||(F_1(y(s)), F_2(y(s)), F^*(y(s)), F_3(y(s)))||_Y < M_R, \qquad \forall y \in B_{Y_T^\zeta} \tag{5.60}$$

which implies that M_R is also an upper bound for the set

$$\{ \sup_{s\in[0,T]} ||(F_1(y(s)), F_2(y(s)), F^*(y(s)), F_3(y(s)))||_Y \,|\, y \in B_{Y_T^\zeta}\},$$

and so using one last time the definition of the supremum, we finally obtain that

$$\sup_{y\in B_{Y_T^\zeta}(0,R)} \sup_{s\in[0,T]} ||(F_1(y(s)), F_2(y(s)), F^*(y(s)), F_3(y(s)))||_Y < M_R. \tag{5.61}$$

□

5.3 Local Existence and Uniqueness of Macroscopic Model - 2.

In section 5.2, we proved theorem 5.2.1 via using Banach Contraction Theorem which states the following, there is a unique local solution of the macroscopic system (5.2) such that,

$$c, i, v \in \mathcal{C}([0,T) : X^\zeta) \text{ and } u \in \mathcal{C}([0,T) : W^{1,p}(\Omega)).$$

Based on a such result, we study the existence of the unique local solution for the third macroscopic system (scenario) as introduced in Alzahrani et al. (2019), namely:

$$\begin{cases} \frac{\partial c}{\partial t} = D_c \Delta c - \eta_c \nabla \cdot (c \nabla u) + \mu_1 c(1-c) - \rho c v, \\ \frac{\partial i}{\partial t} = D_i \Delta i - \eta_i \nabla \cdot (i \nabla u) + \rho c v - \delta_i i, \\ \frac{\partial u}{\partial t} = -u(\alpha_c c + \alpha_i i) + \mu_2 u(1-u-c-i), \\ \frac{\partial v}{\partial t} = D_v \Delta v - \eta_v \nabla \cdot (v \nabla u) + bi - \rho c v - \delta_v v. \end{cases} \tag{5.62}$$

Indeed, this macroscopic scenario (5.62) differes from the baseline macroscpoic system (5.2) in terms of the motility behaviour for two macroscopic components, namely: infected cancer cell and virus particles for which a haptotaxis movement role was considered.

Following similar steps as in section 5.2, we first define new general functions, namely:

$f_{2,2}(i)$ to be a general positive function representing the removal rate of infected cells;

$f_{4,1}(v,u)$ to describe non-local directionality corresponding to biased movement against ECM gradients (acquired due to ECM degradation), i.e. $f_{4,1}(v,u) \geq 0$;

$f_{4,2}(i)$ to be a general positive function representing the virus replication rate;

$f_{4,3}(v)$ to be a general positive function representing the removal rate of virus particles.

Hence, we generalise the macroscopic dynamics (5.62) to be written in the following form:

$$\begin{cases} \frac{\partial c}{\partial t} = D_c \Delta c - \nabla \cdot (c f_{1,1}(c,u)) + c f_{1,2}(c) - f_{1,3}(c,v), \\ \frac{\partial i}{\partial t} = D_i \Delta i - \nabla \cdot (i f_{2,1}(i,u)) + f_{1,3}(c,v) - f_{2,2}(i), \\ \frac{\partial u}{\partial t} = -u f_{3,1}(c,i) + u f_{3,2}(c,i,u), \\ \frac{\partial v}{\partial t} = D_v \Delta v - \nabla \cdot (v f_{4,1}(v,u)) + f_{4,2}(i) - f_{1,3}(c,v) - f_{4,3}(v), \end{cases} \tag{5.63}$$

with taking into account that all notations in this section are written with respect to the previous section (5.2), thus we would not re-define any repeated notations. However, we use the same proposed initial conditions (5.3) with taking into consideration that there is no-flux passing through the tumour boundary $\partial\Omega$ for all components as presented in (5.4) with the following conditions regarding haptotactic motility for all cancer cells type (c,i) and the virus particles (v), namely:

$$\begin{aligned} \langle \nabla f_{1,1}(c,u), \nu \rangle &= 0 \text{ on } (0,\infty) \times \partial\Omega, \\ \langle \nabla f_{2,1}(i,u), \nu \rangle &= 0 \text{ on } (0,\infty) \times \partial\Omega, \\ \langle \nabla f_{4,1}(v,u), \nu \rangle &= 0 \text{ on } (0,\infty) \times \partial\Omega. \end{aligned} \tag{5.64}$$

Moreover, in a similar fashion of assuming a non-local mapping (5.6) on the function $f_{1,1}(c,v)$, we propose new non-local mappings for $f_{2,1}(i,u)$ and $f_{4,1}(v,u)$ respectively,

$$\begin{aligned} f_{2,1}: &\ \mathcal{C}(\overline{\Omega}:\mathbb{R}) \times \mathcal{C}(\overline{\Omega}:\mathbb{R}) \mapsto \mathcal{C}^{1,\beta}(\overline{\Omega}:\mathbb{R}^n), \quad \beta \in (0,1], \\ f_{4,1}: &\ \mathcal{C}(\overline{\Omega}:\mathbb{R}) \times \mathcal{C}(\overline{\Omega}:\mathbb{R}) \mapsto \mathcal{C}^{1,\beta}(\overline{\Omega}:\mathbb{R}^n), \quad \beta \in (0,1]. \end{aligned} \tag{5.65}$$

for which we can define

$$\begin{aligned} f_{2,1}(i,u)(x) &= \int_\Omega f^*_{2,1}(x,y,i(y),u(y))dy, \text{ for } (i,u) \in \mathcal{C}(\overline{\Omega}:\mathbb{R}) \times \mathcal{C}(\overline{\Omega}:\mathbb{R}), \\ f_{4,1}(v,u)(x) &= \int_\Omega f^*_{4,1}(x,y,v(y),u(y))dy, \text{ for } (v,u) \in \mathcal{C}(\overline{\Omega}:\mathbb{R}) \times \mathcal{C}(\overline{\Omega}:\mathbb{R}), \end{aligned} \tag{5.66}$$

where $f^*_{2,1}$ and $f^*_{4,1}$ are continuous functions over the following maps:

$$\begin{aligned} f^*_{2,1} &: \Omega^2 \times \mathbb{R}^2 \mapsto \mathbb{R}^n, \\ f^*_{4,1} &: \Omega^2 \times \mathbb{R}^2 \mapsto \mathbb{R}^n, \end{aligned} \tag{5.67}$$

satisfying the same properties as previously presented in (5.9) and (5.10) for the function $f_{1,1}$, in such way we obtain similar properties for both functions $f^*_{2,1}$ and $f^*_{4,1}$ as well.

Furthermore, the functions $f_{1,2}, f_{1,3}, f_{3,1}$ and $f_{3,2}$ are already assumed to be locally Lipschitz functions as presented in (5.11), hence in a similar manner, we suppose the functions $f_{2,2}, f_{4,2}$ and $f_{4,3}$ are locally Lipschitz as well with the following mappings:

$$\begin{aligned} &f_{2,2}(i) : \mathbb{R} \mapsto \mathbb{R}, \\ &f_{4,2}(i) : \mathbb{R} \mapsto \mathbb{R}, \\ &f_{4,3}(v) : \mathbb{R} \mapsto \mathbb{R}. \end{aligned} \tag{5.68}$$

Based on a such definitions the following theorem holds true.

Theorem 5.3.1 (Local Existence) *Assume that the initial conditions c_0, i_0 and $v_0 \in X^\zeta$ and $u_0 \in W^{1,p}(\Omega)$ are satisfied with all previous assumptions (5.17-5.31), then for any $T > 0$, the macroscopic model 5.63 has a unique local-in-time solution such that :*

$$c, i, v \in \mathcal{C}([0,T) : X^\zeta) \text{ and } u \in \mathcal{C}([0,T) : W^{1,p}(\Omega)).$$

In addition, for $t > 0$, c, i and v are classical solutions and

$$sup(||c||_\infty + ||i||_\infty + ||u||_\infty + ||v||_\infty) < \infty.$$

In order to prove Theorem (5.3.1), we follow an identical sequence of steps as those described in Theorem (5.2.1) combined with the preliminary setting up relations from (5.17) to (5.31) to confirm that there exists a unique solution $(c^*, i^*, u^*, v^*) \in B_{Y_T^\zeta}(0, R)$, which is in fact the unique local solution for system (5.63).

5.4 Local Existence and Uniqueness of Microscopic Model.

In this section, we aim to show the existence of the unique local solution of the microscopic system introduced in Trucu et al. (2016) and then used in Peng et al. (2017); Alzahrani et al. (2019), namely:

$$\begin{cases} \frac{\partial a}{\partial \tau} = D_a \Delta a - \psi_{11} ap + (\psi_{12} - \psi_{13} a) f_{uPA}^{\epsilon Y}(y, \tau), \\ \frac{\partial p}{\partial \tau} = D_p \Delta p - \psi_{21} ap - \psi_{22} p \, f_{PAI-1}^{\epsilon Y}(y, \tau) + \psi_{23} m, \\ \frac{\partial m}{\partial \tau} = D_m \Delta m + \psi_{31} a f_{uPA}^{\epsilon Y}(y,\tau) + \psi_{32} p f_{PAI-1}^{\epsilon Y}(y,\tau) - \psi_{33} m. \end{cases} \tag{5.69}$$

To that end, we first define new general functions in order to write our microscopic model into a generlised form, namely:

$g_{1,1}(a, p)$ to be a general positive function representing the inhibition of uPA caused by PAI-1;

$g_{1,2}(f_{uPA}^{\epsilon Y})$ to be a general positive function describing uPA production caused by the source function $f_{uPA}^{\epsilon Y}$;

$g_{1,3}(a, f^{\epsilon Y}_{uPA})$ to be a general positive function representing the decay in the uPA density caused by cancer cells' uPA receptors (uPAR);

$g_{2,1}(a, p)$ to be a general positive function describing the removal rate of PAI-1 through binding to uPA;

$g_{2,2}(p, f^{\epsilon Y}_{PAI-1})$ to be a general positive function describing the removal rate of PAI-1 through binding to surrounding ECM $f^{\epsilon Y}_{PAI-1}$;

$g_{2,3}(m)$ to be a general positive function representing the production of PAI-1 through plasmin activation;

$g_{3,1}(a, f^{\epsilon Y}_{uPA})$ to be a general positive function representing the production of plasmin due to direct plasminogen activation (through uPA binding to uPAR);

$g_{3,2}(p, f^{\epsilon Y}_{PAI-1})$ to be a general positive function representing the production of plasmin due to direct plasminogen activation (through binding of PAI-1 to neighbouring ECM);

$g_{3,3}(m)$ to be a general positive function describing the removal rate of plasmin.

Thus, the general form of the microscopic system is written as follows:

$$\begin{cases} \frac{\partial a}{\partial \tau} = D_a \Delta a - g_{1,1}(a,p) + g_{1,2}(f^{\epsilon Y}_{uPA}) - g_{1,3}(a, f^{\epsilon Y}_{uPA}), \\ \frac{\partial p}{\partial \tau} = D_p \Delta p - g_{2,1}(a,p) - g_{2,2}(p, f^{\epsilon Y}_{PAI-1}) + g_{2,3}(m), \\ \frac{\partial m}{\partial \tau} = D_m \Delta m + g_{3,1}(a, f^{\epsilon Y}_{uPA}) + g_{3,2}(p, f^{\epsilon Y}_{PAI-1}) - g_{3,3}(m). \end{cases} \tag{5.70}$$

with the following initial conditions:

$$\begin{aligned} &a(0,x) = a_0(x) \geq 0, \;\; p(0,x) = p_0(x) \geq 0, \\ &m(0,x) = m_0(x) \geq 0, \;\; \text{in } \Omega. \end{aligned} \tag{5.71}$$

Moreover, we suppose that there is no-flux passing through the smooth boundary $\partial\Omega$ for all micro components i.e.

$$\langle \nabla a, \nu \rangle = \langle \nabla p, \nu \rangle = \langle \nabla m, \nu \rangle = 0 \text{ on } (0, \infty) \times \partial\Omega, \tag{5.72}$$

where ν is the normal outward unit for vector field to $\partial\Omega$. Furthermore, the functions $g_{1,1}(a,p)$, $g_{1,2}(f^{\epsilon Y}_{uPA})$, $g_{1,3}(a, f^{\epsilon Y}_{uPA})$, $g_{2,1}(a,p)$, $g_{2,2}(p, f^{\epsilon Y}_{PAI-1})$, $g_{2,3}(m)$, $g_{3,1}(a, f^{\epsilon Y}_{uPA})$, $g_{3,2}(p, f^{\epsilon Y}_{PAI-1})$ and $g_{3,3}(m)$ are assumed to be locally Lipschitz functions as exactly assumed previously in (5.11), hence in a similar manner, we suppose these functions defined within the following mappings:

$$\begin{aligned}
&g_{1,1}(a,p) : \mathbb{R} \times \mathbb{R} \mapsto \mathbb{R},\\
&g_{1,2}(f^{\epsilon Y}_{uPA}) : \mathbb{R} \mapsto \mathbb{R},\\
&g_{1,3}(a, f^{\epsilon Y}_{uPA}) : \mathbb{R} \times \mathbb{R} \mapsto \mathbb{R}\\
&g_{2,1}(a,p) : \mathbb{R} \times \mathbb{R} \mapsto \mathbb{R},\\
&g_{2,2}(p, f^{\epsilon Y}_{PAI-1}) : \mathbb{R} \times \mathbb{R} \mapsto \mathbb{R},\\
&g_{2,3}(m) : \mathbb{R} \mapsto \mathbb{R},\\
&g_{3,1}(a, f^{\epsilon Y}_{uPA}) : \mathbb{R} \times \mathbb{R} \mapsto \mathbb{R},\\
&g_{3,2}(p, f^{\epsilon Y}_{PAI-1}) : \mathbb{R} \times \mathbb{R} \mapsto \mathbb{R},\\
&g_{3,3}(m) : \mathbb{R} \mapsto \mathbb{R}.
\end{aligned} \tag{5.73}$$

Theorem 5.4.1 (Local Existence) *Assume that the initial conditions a_0, p_0 and $m_0 \in X^{\varsigma}$ are satisfied with all previous assumptions (5.17-5.31), then for any $T > 0$, the microscopic model 5.70 has a unique local-in-time solution such that :*

$$a, p, m \in \mathcal{C}([0,T) : X^{\varsigma}).$$

In addition, for $t > 0$, a, p and m are classical solutions and

$$sup(||a||_\infty + ||p||_\infty + ||m||_\infty) < \infty.$$

In order to prove Theorem 5.4.1, we use the preliminary setting up relations from (5.17) to (5.31) and we follow similar sequence of steps as those described in Theorem (5.2.1) to show that there exists a unique solution $(a^*, p^*, m^*) \in B_{Y_T^\zeta}(0, R)$, which is in fact the unique local solution for system (5.69).

Chapter 6

Conclusion and Discussions

The main contribution of this work is to propose a novel multi-scale moving boundary framework to describe the complex interactions between tumour and oncolytic viruses (OV). The mathematical perspective was based on coupled systems of partial differential equations both at macro-scale (tissue-scale) and at micro-scale (cell-scale) which are linked through a double feedback loop. On one hand, at the tissue-scale (macro-scale), we have studied multiple scenarios upon some biological observations starting with accounting for the coupled dynamics of cancer cells (uninfected and infected), the surrounding extracellular matrix (ECM), and oncolytic viruses (OV). Then, we have extended this basic macroscopic scenario to include an investigation of more biological observed cases such as (diffusion ability for cancer cells concentration in the spacial domain and the haptotactic migration rule for the directed motility behaviour of cancer cells densities and OV particles towards higher ECM gradients). On other hand, at the micro-scale (cellular scale) we adopted the proteolytic enzymatic system presented in Trucu et al. (2016); Peng et al. (2017), namely, urokinase plasminogen activator (uPA), to include our new approach of tumour-OV interactions. Indeed, those coupled systems of partial dif-

ferential equations both at macro-scale (tissue-scale) and at micro-scale (cell-scale) are connected through a double feedback link (crucial cross-talk). Furthermore, we have carried out a functional analysis investigation to show that the solutions of both the macroscopic model and the microscopic model have a locally-in-time unique solution within an appropriately considered space of function. However, in the following, we will discuss the key modelling and computational points regarding the viral therapy and the analytical findings that have been obtained in this work.

In Chapter 3 we have studied tumour-OV dynamics with the multiscale moving boundary context, bringing together the activity of this interraction at two scales, namely, macroscopic (tissue scale) and microscopic (cell scale) with taking into considerations these two-scales have been computed within our maximal reference domain Y. At the tissue scale, we first explore the coupled dynamics of this interaction within $\Omega(t) \subset Y$ that includes four players, namely, cancer cells densities (uninfected cells and viral-infected cells), surrounding ECM distribution and OV particles. Furthermore, building on some biological observations (Laird, 1964; Nowak and May, 2000; Guiot et al., 2003; Chaplain and Lolas, 2005; Camara et al., 2013; Vähä-koskela and Hinkkanen, 2014), we have assumed multiple scenarios for their dynamical interaction, namely: macro-dynamics scenario (1) equation (3.10); macro-dynamics scenario (2) equation (3.12); and macro-dynamics scenario (3) equation (3.14). At the same time, at the cell-scale we account for the proteolytic dynamics of uPA system within the outer proliferating rim of the tumour boundary $\partial\Omega(t)$ (section 3.4). Indeed, the connection between both scales occurs through a double feedback loop released via top-down link and bottom-up link. As we previously mentioned in Chapters 2, 3 and 4, the top-down link between macro-scale and micro-scale indicates the procedure of how the source of uPA is induced from the macro-scale either through secretion by the cancer cells or simply by activation

from the surrounding ECM within the tumour proliferating rim were mathematically expressed by the formulae in (3.16) and (3.18). The bottom-up link between micro-scale and macro-scale refers to the induced informations from the micro-dynamics activity that is up-taken at the macro-scale and determines the tumour boundary relocation.

We have extended the computational approach of the multiscale numerical framework previously introduced in Trucu et al. (2013). This numerical framework combines a finite difference method to solve the macroscopic system with a finite element method to solve the microscopic system. Building on that our developed numerical framework includes all required changes for our new modelling assumptions involving the finite difference schemes, approximating the diffusion and haptotactic terms, modifying the initial conditions for the macro-dynamics and the boundary conditions for micro-dynamics. Besides that, we added new strategies to improve the numerical outcome including tumour boundary unification, controlling ECM heterogeneity out of the tumour boundary $\partial\Omega(t)$ region. In the following context we first give a summary of the overall results of our numerical investigations in Chapter 3, then we discuss the key factors impacting the viral therapy outcomes.

In order to track the macro-micro dynamics behaviour on the maximal tissue domain ($Y = [0, 8] \times [0, 8]$) and what conditions that lead to improved tumour suppression, we first have chosen a list of baseline parameters as listed in Tables 3.1 and 3.3 which is based on the published studies Camara et al. (2013); Peng et al. (2017). Then, we numerically investigate the findings of our modelling for three macroscale scenarios (3.10), (3.12), and (3.14) in terms of validating the impact of changing some of most essential parameters involved in virus dynamics and spread, namely, the viral infection rate (ρ), the natural death rate of infected cancer cells (δ_i), ECM degradation rates by uninfected cancer cells (α_c) and infected cancer cells

(α_i), the virus replication rate (b), and the amount of the initial administered virus doses.

Based on the baseline parameters list 3.1, for all scenarios of the macroscopic models as presented in (3.10), (3.12) and (3.14), the tumour boundary $\partial\Omega(t)$ is expanding within Y in related to haptotatic migration rule against ECM gradients. Although, a better tumour reduction occurs in the case of considering the haptotactic migration of both virus-infected cells and virus particles towards higher ECM gradients. However, one of the most essential factors impacting tumour mass and invasion area is the viral infection rate (ρ). Experimental studies have shown that increasing or decreasing the viral infection rate (ρ) leads to an important variation in tumour size (Maroun et al., 2017), therefore we have done a numerical investigation for the effect of the infection rate on the total tumour dynamics (uninfected + infected) concluding that increasing the rate at which the oncolytic virus infects the cancer cells plays a central role in the development of the viral therapy i.e. any increase in (ρ) (with respect to the baseline value) definitely leads to more tumour suppression. Additionally, in order to observe the viral therapy outcomes from another perspective, we examined tumour invasion in the terms of the effect of the death rate of infected cells δ_i. Decreasing δ_i (with respect to baseline values) leads to a dramatically reduction in the uninfected cancer cells within the viral-interactions areas in $\Omega(t)$, while increasing δ_i prevents tumour suppression improvement. However, δ_i alone does not make a clear difference in the overall tumour mass, although its variation still play a key role in the density of uninfected cancer cells within virus accumulation areas. This gave rise to examine different parameters, namely, ECM degradation rates α_c and α_i. Indeed, the process of tumour invasion of the surrounding tissue and the viral spread depends on the partial degradation of ECM. Therefore, the variation of ECM degradation rates are expected to be crucial within

viral therapy. In order to investigate this impact, we chose doubling both degradation rates (with respect to the baseline) where that showed the dependancy of the success or failure of the oncolytic virus distribution within tumour site, i.e. whenever ECM is degraded, OV has more chances to spread within the tumour tissue and pass to the accumulated areas of uninfected cancer cells. Actually in case of increasing ECM degradation rates, the haptotactic migration of both infected and uninfected cancer cells is oriented towards regions of higher ECM levels. This enables cancer cells (infected and uninfected) to be accumulated within certain areas causing higher degree of infection which leads in its turn to a clear decrease in the total tumour mass.

Further, one of crucial features for oncolytic viruses is its ability to replicate within the tumour site when connecting to surrounding cancer cells. Hence, the number of virus particles release by an infected cancer cell (b) is an expected crucial factor on the overall therapy process Maroun et al. (2017). Indeed, what we have found from increasing the replication rate of virus particles (with respect to baseline value) is exactly matching what we have expected, i.e., when increasing (b), the total tumour mass is always below the baseline scenario. Otherwise, in the absence of the replicating feature, the morphology of the growing tumour is increased in the spatial tissue domain which in turn leads to a clear increase in the tumour size and mass. Moreover, A special attention was paid to the importance of virus dosage on the viral therapy as this also presented interest for experimental works by Rommelfanger et al. (2011); Vähä-koskela and Hinkkanen (2014). Alongside the dosage size, the amount and the location in regards to the initial tumour size also play a central role as well Bajzer et al. (2008); Rioja et al. (2016). However, we numerically investigated all these factors to conclude the following. Increasing the initial viral dosage leads to a clear rapid decrease in tumour mass and size over the first 30

stages. Then the tumour distribution came back to a normal growth in comparison with baseline growth. However, the virus dosage is still an open question where new virus doses need to be applied in proper sites at later stages so that we could reach to better tumour suppression scenario. Finally, based on the previous findings in this chapter, we proposed an alternative Table 3.2 (with respect to the baseline values) to obtain more improved and controlled tumour suppression scenario. In this new context, we tried to combine the following assumptions, decreasing (the natural death rate of infected cancer cells) and increasing (the infection rate of cancer cells, ECM degradation rate and the virus replication rate), in parallel to having five initial virus doses on five various locations within tumour site $\Omega(t)$ and boundary $\partial\Omega(t)$. Building on such assumptions, we obtained a complete control of the tumour mass which in turn leads to a faster viral therapy. Furthermore, the distribution of uninfected cancer is preserved at very low levels for all macro-micro stages. Even though we examined both macro-dynamics scenarios for longer observation of time, we still had the same control over the the total tumour mass.

In Chapter 4 we have extended our previous chapter (published already in Alzahrani et al. (2019)) to include the impact of a fusogenic oncolytic virus that can form syncytia structures to explore the outcome of the newly emerging oncolytic viral therapy. Experimental studies in most clinical trials agreed on the variation of OV impact on the viral therapy due to many factors such as virus type, size, etc. Hence, some subclass of OV leads to formation of syncytia structures resulting better anti-tumour scenario (Meerani and Yao, 2010; Kauman et al., 2015; Krabbe and Altomonte, 2018; Ebert et al., 2004). Thus, based on our extended multiscale framework, at the macro-scale we take into account new modelling hypotheses to describe the dynamical behaviour for tumour-OV interactions involving five macroscopic components, namely, uninfected cancer cells (c), infected cancer

cells (i), syncytia cancer cells (s), ECM (u) and OV (v). At the micro-scale, we take into consideration the proteolytic ezymatic system (uPA) to be computed within the tumour boundary $\partial\Omega(t)$. Again, we have used the same connection methodology (cross-talk) to pass the solutions between macro-scale and micro-scale, in addition to passing the obtained informations at the current macro-micro stage to the next stage. We also added a series of requirements into the computational approach of the multiscale numerical framework to involve our new modelling assumptions as detailed in Chapter 4. To get further understanding of how our new modelling approach, focus must be placed on our previous findings. To validate this, we have considered multiple cases regarding the tumour-OV interactions in the presence of cells syncytium, namely, Macro-dynamics case (1) equation (4.8), Macro-dynamics case (2) equation (4.9), Macro-dynamics case (3) equation (4.10) and Macro-dynamics case (4) equation (4.13), where, in brief, all macroscopic cases are centred on assumptions regarding either the absence or the presence of syncytia cancer cells diffusion within the spatial domain with and without haptotactically directional movement towards higher ECM gradients.

Based on the previous results (presented in Chapter 3), we began our numerical investigation by using the baseline parameters summarised in Tables 4.1 and 4.2 to examine three cases of syncytia motility/lack-of-motility. In the first case, we assumed syncytia structures has the lack of movement within the domain, but syncytia cells still has its own impact upon the process of remodelling and degradation ECM components. Based on this scenario, we observed an increased accumulation of syncytia structures formation in those regions characterised by lower mass of cancer cell. However, in the second macro-dynamic case (4.9), we take into consideration the random motility of syncytia structures within the domain although we still ignored the haptotactic rule of its directional movement to ECM. Herein we explored

the effect of various values of the diffusion coefficient of syncytia cancer cells D_s on the overall dynamics of our multiscale moving boundary modelling. Further, this variation in D_s values was taken with respect to the values of the diffusion coefficient of single infected cells D_i. During the numerical investigations, we concluded that increasing the random motility rate of syncytia cancer cells leads to an undesirable situation of viral therapy, while decreasing that rate causes to a considerably reduction in the overall tumour mass and in the invasion area spread. This could be explained as follows, slower syncytia diffusion within the domain leads to a localised release of the virus particles and that in turn lead to increase the process of the tumour suppression.

For the third case of the macro-dynamics cases, we proposed the directional movement rule of syncytia cancer cells towards higher ECM gradients to be haptotactics and this hypothesis was described mathematically by the macro-dynamics (4.10). In order to observe the effect of various syncytia haptotactic velocities η_s on the overall dynamics and viral therapy progress, we chose various values of η_s with respect to the baseline values of the haptotactic velocities for both the single infected cancer cells η_i and virus particles η_v. Our investigation showed that the best choice of haptotactic velocity of syncytia η_s is to be chosen equal or almost equal to η_v but it should be less than η_i in order to obtain a better viral therapy results in a comparison with the baseline outcome.

One other important factor on the overall viral therapy is the fusion failure probability p_0. Although this crucial factor plays a key role in determining the density of syncytia cancer cells within the invasion process on the domain Y, its choice should be built on reasonable estimated values for the replication and death rates b_s, δ_s of syncytia cancer cells with respect to the estimated values of single infected cancer cells. Therefore, we chose a higher syncytia replication rate, i.e., $(b_s > b_i)$ and a

lower syncytia natural death rates, i.e., ($\delta_s < \delta_i$). Based on that, we examined the variation of the fusion failure probability p_0 to conclude that higher probabilities of syncytium formation (i.e., lower p_0) leads to better and faster viral therapy over all macro-micro stages. However, we still have another example showing the most powerful control of tumour invasion scenario obtained by Table 4.3 associated with Table 4.2. This example has been obtained by combining best parameters choices depending on the previous findings (Chapter 3) and current results (Chapter 4).

Finally, we have studied the case when the random motility rate of syncytia cancer cells is not a constant. Indeed, this assumption is more closed to reality scenarios due to that the diffusion of syncytia is influenced by the surrounding densities, namely, ECM and OV. Hence, we chose to incorporate this hypothesis into our third macro-dynamics case, namely, (4.10). We generalised the mathematical modelling of this macro-dynamics case to include two sub-cases in terms of syncytia density dependent, namely, macro-dynamics sub-case (4.13)-(4.14) and macro-dynamics sub-case (4.13)-(4.15). In the first sub-case (4.14) we investigated the syncytia diffusion linear dependancy only on OV dynamics, while in for the considered sub-case (4.15) we studied the syncytia diffusion linear dependancy on both dynamics OV and ECM. The general findings apparently showed that both assumed scenarios of the macroscopic model with the density-dependent syncytia diffusion gave more tumour suppression which means getting a better viral therapy case over all macro-micro stages. However, we did not find any clear difference between both sub-cases in terms of the tumour reduction. In fact, the main cause of this tumour suppression is based on the accumulation of syncytia formation in areas with uninfected and infected tumour cells, which in turn leads to releasing more OV within a certain area on the tumour site $\Omega(t)$, hence, a better and a faster tumour reduction occurs within this area.

In Chapter 5 we developed further mathematical analysis to support our numerical investigations those have been done in the previous chapters. We have studied the local existence solutions and their uniqueness within proposed spatio-temporal domains for three mathematical modelling, namely, two scenarios of the macroscopic models, (3.10) (rewritten in a general form in (5.2)) and (3.14) (rewritten in a general form in (5.63)), in addition to the microscopic model previously introduced in 3.4 (rewritten in a general form in (5.70)). For analysis we followed similar methodology previously explored also in Rodrigo (2008); Szymanska et al. (2009); Chaplain et al. (2011); Bitsouni et al. (2017) while taking into consideration the differences in modelling assumption. In this chapter, we first began to prove the existence of the unique solution for the baseline macroscopic scenario (5.2). The proof has been obtained via fixed point argument involving Banach Contraction Theorem (Yosida, 1995). To achieve this, we took advantage of essential mathematical concepts involving the classical semigroup frameworks presented in Henry (1981), such as: the sectorial operator, the lipschitzianity properties, space embeddings for Holder continuous functions, the triangle inequality, the continuity of the norm, the property of the Lebesgue Integral and Bochner Integral (Yosida, 1995). Based on these, we have concluded that there exist a unique local-in-time solution for the macroscopic scenario (5.2). Furthermore, in a similar manner we applied the same analytical sequence of steps as those described in Theorem (5.2.1) to show the existence and uniqueness locally-in-time of solutions for both models, the macroscopic scenario (5.63) (for more details see Theorem (5.70)) and the microscopic model (for more details see Theorem (5.4.1)).

In order to validate the estimation of the parameters regime that has been used during this work, in this thesis we have already examined the model performance against some biological observations. The initial estimation of model parameters

was mainly based on the taken values from the following references, Camara et al. (2013), Peng et al. (2017), Biesecker et al. (2009) and Alzahrani et al. (2019). Since our baseline estimation of the parameter values ensures an appropriate fit in a comparison with some biological observations, we have either minimised or maximised some of the parameters in order to examine the modelling performance against certain biological observations such as examining the effect of viral infection speed within tumour dynamics. However, there are still challenges and open questions in terms of the validation and limitation of the model parameters. One of these challenges is how to determine the amount of the viral dosage and at which stage of cancer invasion should it be given during treatment process. However, in the future we aim to focus more in the impact of the spatial distribution of viral dosage and ECM sensitivity upon the viral therapy outcome. Furthermore, we still have the chance to develop our current work in relation to improving the theoretical and the computational two-scale framework to involve three scales, namely, intracellular scale, cellular scale and tissue scale, in addition to developing the analysis part to include the existence of solutions globally-in-time for the two-scale model within two dimensional space. Finally, there are still many interesting research points in the field of multi-scale modelling of cancer - oncolytic virus interaction which require further development and future work.

Appendix A

A.1 Description of Multi-scale Numerical Framework

For completeness, in this section, we present the numerical framework first interduced in (Trucu et al., 2013) and then later extended and applied in the following studies (Trucu et al., 2016; Peng et al., 2017; Alzahrani et al., 2019). The computational framework stands for computing two dimensional multiscale modelling in which based on two numerical methods, namely: Finite Difference Method (FDM) and Finite Element Method (FEM). At the macro-scale, the macro-dynamics is computed by the finite difference approach involving central differences and midpoint approximations. While at the micro-scale, the finite element approach is used to compute the micro-dynamics on the micro-domain namely, $\mathcal{P}^*_\epsilon(t)$. However, in the following, we first describe the discretisation, give a short description for the macro-dynamics computation process, and explore the interpolation used to express the top-down link (that enables the source for the micro-dynamics induced by the macro-scale).

A.1.1 The big picture: spatial domain discretisation at both macro and micro - scales

We assume that the tumour $\Omega(t)$ grows within a maximal reference spacial domain Y, which is taken in our numerical experiments to be the rectangular region $Y := [0, 8] \times [0, 8]$. Details of the macro-solver are given in the next appendix subsection. We discretise Y uniformly in both spatial directions with a equal mesh size $\Delta x = \Delta y = 0.03125$.

In addition, the time interval $[t_0, t_0 + \Delta t]$ is discretised by uniformly time step with a size $\delta\tau = \frac{\hat{\delta}t}{k}$.

Finally, for the micro-domains and micro-dynamics, the discretisation steps can be summarised as follows:

1. For any time instance $t_0 \geq 0$, any boundary micro-domain $\epsilon Y \in \mathcal{P}(t_0)$ is centred a boundary point $x \in \partial\Omega(t_0) \cap \epsilon Y$, having its size $\epsilon = 2\Delta x = 0.0625$.

2. The top-down nonlocal source terms is done in brief as follows. We use directly the non-local formula at the overlapping macro-micro mesh points and use micro-scale barycentric coordinates to interpolate at all other micro-points $y \in \epsilon Y \setminus \{(i\Delta x, j\Delta x) \,|\, i, j = 1...q\}$. This is explored in full details in Section 2.4.1.

3. On each ϵY we then solve the micro-dynamics via finite element by involving bilinear shape function on a square micro-mesh placed on ϵY.

A.1.2 Macro-solver

- (Temporal discretisation) The solver uses the Method of Lines in which the time marching for the macro-system has been approximated by predictor corrector method (predicting with Euler and correcting with Trapezoidal method).

- The predictor is given by

$$\hat{c}_{i,j}^{n+1} = c_{i,j}^{n} + \hat{\delta}t(F(c_{i,j}^{n}, v_{i,j}^{n}))$$

- The corrector is given by

$$c_{i,j}^{n+1} = c_{i,j}^{n} + \frac{1}{2}\hat{\delta}t(F(c_{i,j}^{n}, v_{i,j}^{n}) + F(c_{i,j}^{n+1}, v_{i,j}^{n+1}))$$

- (Spatial discretisation) At any discrete spatial point $(i\Delta x, j\Delta x)$, $\forall i, j = 1, ..., q$, and any given time node $t^n := t_0 + n\hat{\delta}t$, $\forall n = 0, ..., N$, the spatial operator of the right hand side is represented by the following approximations, namely: the diffusion is approximated by a midpoint approximations scheme as follows:

$$(\Delta c)_{i.j}^{n} \approx \frac{(c_x)_{i+\frac{1}{2},j}^{n} - (c_x)_{i-\frac{1}{2},j}^{n}}{\Delta x} + \frac{(c_y)_{i,j+\frac{1}{2}}^{n} - (c_y)_{i,j-\frac{1}{2}}^{n}}{\Delta y}$$

and the haptotaxis term is approximated by:

$$\nabla \cdot (c\nabla u)_{i,j}^{n} \approx \frac{(c)_{i+\frac{1}{2},j}^{n}(u_x)_{i+\frac{1}{2},j}^{n} - (c)_{i-\frac{1}{2},j}^{n}(u_x)_{i-\frac{1}{2},j}^{n}}{\Delta x} + \frac{(c)_{i,j+\frac{1}{2}}^{n}(u_y)_{i,j+\frac{1}{2},}^{n} - (c)_{i,j-\frac{1}{2}}^{n}(u_y)_{i,j-\frac{1}{2}}^{n}}{\Delta y},$$

where

$$
\begin{aligned}
(c_x)^n_{i+\frac{1}{2},j} &= \tfrac{(c)^n_{i+1,j}-(c)^n_{i,j}}{\Delta x} \quad \& \quad (u_x)^n_{i+\frac{1}{2},j} = \tfrac{(u)^n_{i+1,j}-(u)^n_{i,j}}{\Delta x} \\
(c_x)^n_{i-\frac{1}{2},j} &= \tfrac{(c)^n_{i,j}-(c)^n_{i-1,j}}{\Delta x} \quad \& \quad (u_x)^n_{i-\frac{1}{2},j} = \tfrac{(u)^n_{i,j}-(u)^n_{i-1,j}}{\Delta x} \\
(c_y)^n_{i,j+\frac{1}{2}} &= \tfrac{(c)^n_{i,j+1}-(c)^n_{i,j}}{\Delta x} \quad \& \quad (u_y)^n_{i,j+\frac{1}{2}} = \tfrac{(u)^n_{i,j+1}-(u)^n_{i,j}}{\Delta x} \\
(c_y)^n_{i,j-\frac{1}{2}} &= \tfrac{(c)^n_{i,j}-(c)^n_{i,j-1}}{\Delta x} \quad \& \quad (u_y)^n_{i,j-\frac{1}{2}} = \tfrac{(u)^n_{i,j}-(u)^n_{i,j-1}}{\Delta x}.
\end{aligned}
$$

and $(c)^n_{i+\frac{1}{2},j}, (c)^n_{i-\frac{1}{2},j}, (c)^n_{i,j+\frac{1}{2}}, (c)^n_{i,j-\frac{1}{2}}$ are given here via the following midpoint rules:

$$
\begin{cases}
c^n_{i+\frac{1}{2},j} & := \frac{c^n_{i,j}+c^n_{i+1,j}}{2}, \\
c^n_{i-\frac{1}{2},j} & := \frac{c^n_{i,j}+c^n_{i-1,j}}{2}, \\
c^n_{i,j+\frac{1}{2}} & := \frac{c^n_{i,j}+c^n_{i,j+1}}{2}, \\
c^n_{i,j-\frac{1}{2}} & := \frac{c^n_{i,j}+c^n_{i,j-1}}{2}.
\end{cases}
$$

A.1.3 Micro-solver

- Define Neumann boundary conditions on every micro domain ϵY.
- Assume the following initial conditions, $a(x,t) = p(x,t) = m(x,t) = 0$.
- Using midpoint rule for integral sources and a trapezoidal predictor-corrector for time integration.
- Use finite element method to solve the micro-system on each boundary micro-domain ϵY.

A.1.4 Bottom-up Link

- Intialize for Next Macro-Micro Stage.
- If the invasion probability is applied, compute new direction and magnitude of the movement.
- Replace the initial conditions with the solution at the final time of the previous macro-micro stage.
- Repeat the macro-micro solver on the new expanded domain $\Omega(t_0 + \Delta t)$.

A.2 Sensitivity Analysis for ECM Initial Conditions

In Figure A.1, we explore the sensitivity of heterogeneity within the ECM initial conditions on the overall viral therapy. We consider three cases for the ECM initial condition, which range from completely homogeneous ECM to certain level of spatial inhomogeneities in the ECM. These are given mathematically through

$$u(x,0) = \frac{1}{2} + \gamma \frac{(0.3sin(4\pi \left\|x\right\|_2) + sin(4\pi \left\|(4,0) - x\right\|_2))}{2}.$$

where the parameter γ controls the heterogeneity level. Finally, in this numerical experiment we use the baseline parameters set 4.1 alongside the one-dose virus initial condition presented in 3.2(c). Figure A.1 shows the outcome of this sensitivity exploration, and we observe there that as ECM heterogeneity increases the tumour evolution moves away from the compact growth exhibited in the homogeneous case, leading to a more complicated tumour morphology.

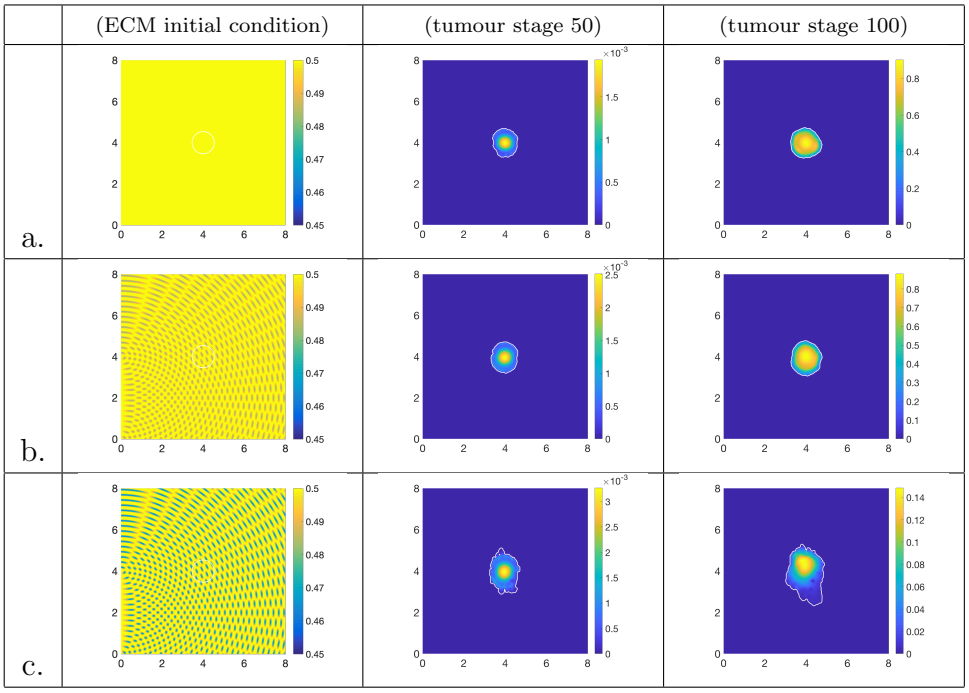

Figure A.1: Multi-scale simulation involving macro-dynamics (4.10) and three cases of ECM initial conditions, that correspond to the following three levels of the heterogeneity parameter γ, namely: a. $\gamma = 0$; b. $\gamma = 0.0625$; c. $\gamma = 0.125$. Left column shows the initial ECM distribution, while middle and right columns show the total tumour distribution at stages (50 and 100).

Bibliography

Adam, J.A., 1986. A simplified mathematical model of tumour growth. *Math. Biosci.* **81**(2), 229–244.

Agarwal, M., Bhadauria, A.S., 2011. Mathematical modelling and analysis of tumour therapy with oncolytic virus. *Applied Mathematics* **2**(1), 131–140.

Alemani, D., Pappalardo, F., Pennisi, M., Motta, S., Brusic, V., 2012. Combining cellular automata and lattice boltzmann method to model multiscale avascular tumor growth coupled with nutrient diffusion and immune competition. *Journal of Immunological Methods* **376**(1), 55 – 68.

Alemany, R., 2013. Viruses in cancer treatment. *Clinical and Translational Oncology* **15**(3), 182–188.

Alzahrani, T., Eftimie, R., Trucu, D., 2019. Multiscale modelling of cancer response to oncolytic viral therapy. *Mathematical Biosciences* **310**, 76–95. doi:10.1016/j.mbs.2018.12.018.

Andasari, V., Gerisch, A., Lolas, G., South, A., Chaplain, M.A.J., 2011. Mathematical modelling of cancer cell invasion of tissue: biological insight from mathematical analysis and computational simulation. *J. Math. Biol.* **63**(1), 141–171.

Anderson, A.R.A., 2005. A hybrid mathematical model of solid tumour invasion: the importance of cell adhesion. *Math. Medic. Biol.* **22**, 163–186.

Anderson, A.R.A., Chaplain, M.A.J., Newman, E.L., Steele, R.J.C., Thompson, A.M., 2000. Mathematical modelling of tumour invasion and metastasis. *J. Theor Med* **2**(2), 129–154.

Andreasen, P.A., Egelund, R., Petersen, H.H., 2000. The plasminogen activation system in tumor growth, invasion, and metastasis. *Cell Mol Life Sci* **57**(1), 25–40. doi:10.1007/s000180050497.

Andreasen, P.A., Georg, B., Lund, L.R., Riccio, A., Stacey, S.N., 1990. Plasminogen activator inhibitors: hormonally regulated serpins. *Molecular and Cellular Endocrinology* **68**(1), 1 – 19. doi:10.1016/0303-7207(90)90164-4.

Andreasen, P.A., Kjøller, L., Christensen, L., Duffy, M.J., 1997. The urokinase-type plasminogen activator system in cancer metastasis: a review. *Int. J. Cancer* **72**(2), 1–22. doi:10.1002/(SICI)1097-0215(19970703)72:1<1::AID-IJC1>3.0.CO;2-Z.

Ayala-Breton, C., Russell, L., Russell, S., Peng, K.W., 2014. Faster replication and higher expression levels of viral glycoproteins give vesicular stomatitis virus/measles virus hybrid VSV-FH a growth advantage over measles virus. *J. Virology* **88**, 8332–8339.

Bai, Y., Hui, P., Du, X., Su, X., 2019. Updates to the antitumour mechanism of oncolytic virus. *Thoracic Cancer* , 1–5.

Bajzer, Z., Carr, T., Josić, K., Russell, S., Dingli, D., 2008. Modelling of cancer virotherapy with recombinant measles viruses. *Theor. Biol.* **252**, 109–122.

Balachandran, S., Porosnicu, M., Barber, G.N., 2001. Oncolytic activity of vesicular stomatitis virus is effective against tumors exhibiting aberrant p53, ras, or myc function and involves the induction of apoptosis. *Journal of Virology* **75**(7), 3474–3479. URL: https://jvi.asm.org/content/75/7/3474, doi:10.1128/JVI.75.7.3474-3479.2001, arXiv:https://jvi.asm.org/content/75/7/3474.full.pdf.

Berg, D., Offord, C., Kemler, I., Ennis, M., Chang, L., Paulik, G., Bajzer, Z., Neuhauser, C., Dingli, D., 2019. *In vitro* and *in silico* multidimensional modelling of oncolytic tumour virotherapy dynamics. *PLoS Comput. Biol.* **15**(3), e1006773.

Biesecker, M., Kimn, J.H., Lu, H., Dingli, D., Bajzer, Z., 2009. Optimization of virotherapy for cancer. *Bulletin of Mathematical Biology* **72**, 469–489.

Bitsouni, V., Chaplain, M.A.J., Eftimie, R., 2017. Mathematical modelling of cancer invasion: The multiple roles of tgf- pathway on tumour proliferation and cell adhesion. *Mathematical Models and Methods in Applied Sciences* **27**(10), 1929–1962.

Bœuf, F.L., Batenchuk, C., ha -Koskela, M.V., Breton, S., Roy, D., Lemay, C., Cox, J., Abdelbary, H., Falls, T., Waghray, G., Atkins, H., Stojdl, D., Diallo, J.S., Kærn, M., Bell, J.C., 2013. Model-based rational design of an oncolytic virus with improved therapeutic potential. *Nature Communications* **4**, 1974.

Byrne, H., Chaplain, M., 1996a. Modelling the role of cell-cell adhesion in the growth and development of carcinomas. *Math Comput Model* **24**(12), 1–17. doi:10.1016/S0895-7177(96)00174-4.

Byrne, H., Chaplain, M., Pettet, G., Mcelwain, D.L.S., 2001. A mathematical model of trophoblast invasion. *Appl. Math. Lett.* **14**(8), 1005–1010.

Byrne, H.M., Chaplain, M., 1995a. Growth of nonnecrotic tumours in the presence and absence of inhibitors. *Math. Biosci.* **130**, 151–181.

Byrne, H.M., Chaplain, M., 1995b. Mathematical models for tumour angiogenesis: numerical simulations and nonlinear wave solutions. *Bull. Mathe. Biol.* **57**(3), 461–486.

Byrne, H.M., Chaplain, M., 1998. Necrosis and apoptosis: Distinct cell loss mechanisms in a mathematical model of avascular tumour growth. *J. Theor. Medic.* **1**, 223–235.

Byrne, H.M., Chaplain, M.A., 1996b. Modelling the role of cell-cell adhesion in the growth and developement of carcinoma. *Math. Comput. Model.* **24**(12), 1–17.

Camara, B.I., Mokrani, H., Afenya, E., 2013. Mathematical modelling of glioma therapy using oncolytic viruses. *Mathematical Biosciences and Engineering* **10**(3), 565–578.

Caravagna, G., Donofrio, A., Milazzo, P., Barbuti, R., 2010. Tumour suppression by immune system through stochastic oscillations. *Journal of Theoretical Biology* **265**(3), 336–345.

Chaplain, M., Lachowicz, M., Szymanska, Z., Wrzosek, D., 2011. Mathematical modelling of cancer invasion: The importance of cell-cell adhesion and cell-matrix adhesion. *Math. Model. Meth. Appl. Sci.* **21**(4), 719–743.

Chaplain, M., Stuart, A., 1993. A model mechanism for chemotactic response of endothelial cells to tumour angiogenesis factor. *J. Math. Appl. Medic. Biol.* **10**, 149–168.

Chaplain, M.A., 1996. Avascular growth, angiogenesis and vascular growth in solid tumours: The mathematical modelling of the stages of tumour development. *Math. Comput. Model.* **23**(6), 47–87.

Chaplain, M.A., Graziano, L., Preziosi, L., 2006. Mathematical modelling of the loss of tissue compression responsiveness and its role in solid tumour development. *Mathematical Medicine and Biology* **23**, 197–229.

Chaplain, M.A.J., Lolas, G., 2005. Mathematical modelling of cancer cell invasion of tissue: The role of the urokinase plasminogen activation system. *Math Mod Meth Appl S* **15**, 1685–1734. doi:10.1142/S0218202505000947.

Chaplain, M.A.J., Lolas, G., 2006. Mathematical modelling of cancer invasion of tissue: Dynamic heterogeneity. *Netw Heterog Media* **1**(3), 399–439. doi:10.3934/nhm.2006.1.399.

Chen, Y., Williams, V., Filippova, M., Filippov, V., Duerksen-Hughes, P., 2014. Viral carcinogenesis: Factors inducing dna damage and virus integration. *Cancers* **6**, 2155–2186.

Choi, I.K., Strauss, R., Richter, M., Yun, C.O., Lieber, A., 2013. Strategies to increase drug penetration in solid tumors. *Frontiers in Oncology* **3**, 1–18.

Compton, A., Schwartz, O., 2017. They might be giants: does syncytium formation sink or spread HIV infection? *PLoS Pathog.* **13**(2), e1006099.

Cox, T., Erler, J., 2011. Remodeling and homeostasis of the extracellular matrix: implications for fibrotic diseases and cancer. *Dis. Model Mech.* **4**(2), 165–178.

Deakin, N.E., Chaplain, M.A.J., 2013. Mathematical modelling of cancer cell invasion: the role of membrane-bound matrix metalloproteinases. *Front. Oncol.* **3**(70), 1–9.

Degryse, B., 2011. Editorial [hot topic: The urokinase receptor system as strategic therapeutic target: Challenges for the 21st century (executive guest editor: Bernard degryse)]. *Current Pharmaceutical Design* **17**, 1872 – 1873.

Dingli, D., Offord, C., Myers, R., Peng, K.W., Carr, T., Josić, K., Russell, S., Bajzer, Z., 2009. Dynamics of multiple myeloma tumour therapy with a recombinant measles virus. *Cancer Gene Therapy* **16**, 873–882.

Dmitrieva, N., Yu, L., Viapiano, M., Cripe, T., Chiocca, E., Glorioso, J., Kaur, B., 2011. Choindroitinase ABC I-mediated enhancement of oncolytic virus spread and anti tumour efficacy. *Clin. Cancer Res.* **17**(6), 1362–1372.

Donofrio, A., 2008. "noisy oncology": Some caveats in using gaussian noise in mathematical models of chemotherapy, in: Hosking, R.J., Venturino, E. (Eds.), Aspects of Mathematical Modelling. Birkhäuser Verlag AG, Basel, Switzerland. Mathematics and Biosciences in Interaction, pp. 229–234.

Donofrio, A., 2010. On the interaction between the immune system and an exponentially replicating pathogen. *Mathematical Biosciences & Engineering* **7**(3), 579–602.

Donofrio, A., 2013. Bounded Noises in Physics, Biology, and Engineering. Modeling and Simulation in Science, Engineering and Technology, Birkhauser.

Ebert, O., Shinozaki, K., Kournioti, C., Park, M.S., García-Sastre, A., Woo, S.L.C., 2004. Syncytia induction enhances the oncolytic potential of vesicular stomatitis virus in virotherapy for cancer. *Cancer Research* **64**(9), 3265–3270. doi:10.1158/0008-5472.CAN-03-3753.

Enderling, H., Chaplain, M., 2013. Mathematical modeling of tumor

growth and treatment. *Current pharmaceutical design* **20**. doi:10.2174/138161281966613112515043 4.

Endres, M., Kneitz, S., Orth, M.F., Perera, R.K., Zernecke, A., Butt, E., 2016. Regulation of matrix metalloproteinases (mmps) expression and secretion in mda-mb-231 breast cancer cells by lim and sh3 protein 1 (lasp1). *Oncotarget* **7**(39), 64244–64259. doi:10.18632/oncotarget.11720.

Filley, A., Dey, M., 2017. Immune system, friend or foe of oncolytic virotherapy? *Frontiers in Oncology* **7**(106), pp. 8. doi:10.3389/fonc.2017.00106.

Friedman, A., Lai, X., 2018. Combination therapy for cancer with oncolytic virus and checkpoint inhibitor: A mathematical model. *Plos One* **13**(2), 1–21.

Fukuhara, H., Ino, Y., Todo, T., 2016. Oncolytic virus therapy: a new era of cancer treatment at dawn. *Cancer Sci.* **107**, 1373–1379.

Gatenby, R.A., 1995. The potential role of transformation-induced metabolic changes in tumor-host interaction. *Cancer Res* **1766**, 4151–4156.

Gatenby, R.A., Gawlinski, E.T., 1996. A reaction-diffusion model of cancer invasion. *Cancer Res.* **56**, 5745–5753.

Gerisch, A., Chaplain, M., 2008. Mathematical modelling of cancer cell invasion of tissue: Local and non-local models and the effect of adhesion. *J Theor Biol* **250**(4), 684 – 704. doi:10.1016/j.jtbi.2007.10.026.

Greenspan, H.P., 1976. On the growth and stabiligy of cell cultures and solid tumours. *J. Theor. Biol.* **56**, 229–242.

Guiot, C., Degiorgis, P., Delsanto, P., Gabriele, P., Diesboeck, T., 2003. Does

tumour growth follow a "universal law"? *Journal of Theoretical Biology* **225**, 147–151.

Hanahan, D., Weinberg, R.A., 2000. The hallmarks of cancer. *Cell* **100**, 57–70.

Hanahan, D., Weinberg, R.A., 2011. Hallmarks of cancer: The next generation. *Cell* **144**(5), 646–674.

Harpold, H.L., Alvord, Ellsworth C., J., Swanson, K.R., 2007. The evolution of mathematical modeling of glioma proliferation and invasion. *Journal of Neuropathology and Experimental Neurology* **66**(1), 1–9.

Hassona, Y., Cirillo, N., Heesom, K., Parkinson, E.K., Prime, S.S., 2014. Senescent cancer-associated fibroblasts secrete active mmp-2 that promotes keratinocyte dyscohesion and invasion. *British Journal Of Cancer* **111**, 1230–1237. doi:10.1038/bjc.2014.438.

Henry, D., 1981. Geometric theory of semilinear parabolic equations. *Lecture Notes in Mathematics,Springer* .

Herschke, F., Plumet, S., Duhen, T., Azocar, O., Druelle, J., Laine, D., WIld, T., Rabourdin-Combe, C., Gerlier, D., Valentin, H., 2007. Cell-cell fusion induced by measles virus amplifies the type-I interferon response. *J. Virol.* **81**(23), 12859–12871.

Higuchi, H., Bronk, S., Bateman, A., Harrington, K., Vile, R., Gores, G., 2000. Viral fusogenic membrane glycoprotein expression causes syncytia formation with bioenergetic cell death: implications for gene therapy. *Cancer Research* **60**, 6396–6402.

Hoffner, B., Iodice, G., Gasal, E., 2016. Administration and handling of talimogene laherparepvec: an intralesional oncolytic immunotherapy for melanoma. *Oncology Nursing Forum* **43**(2), 219–226.

Huang, J.H., Zhang, S.N., Choi, K.J., Choi, I.K., Kim, J.H., Lee, M., Kim, H., Yun, C.O., 2009. Therapeutic and tumor-specific immunity induced by combination of dendritic cells and oncolytic adenovirus expressing il-12 and 4-1bbl. *Molecular therapy : the journal of the American Society of Gene Therapy* , doi:10.1038/mt.2009.205.

Huda, S., Weigelin, B., Wolf, K., Tretiakov, K.V., Polev, K., Wilk, G., Iwasa, M., Emami, F.S., Narojczyk, J.W., Banaszak, M., Soh, S., Pilans, D., Vahid, A., Makurath, M., Friedl, P., Borisy, G.G., Kandere-Grzybowska, K., Grzybowski, B.A., 2018. Lévy-like movement patterns of metastatic cancer cells revealed in microfabricated systems and implicated in vivo. *Nature communications* **9**(1), 4539–4539.

Hudson, A.L., Colvin, E.K., 2016. Transgenic mouse models of sv40-induced cancer. *ILAR* **57**(1), 44–54.

Jacobsen, K., Pilyugin, S.S., 2015. Analysis of a mathematical model for tumor therapy with a fusogenic oncolytic virus. *Mathematical Biosciences* **270**, 169–182.

Jacobsen, K., Russell, L., Kaur, B., Friedman, A., 2015. Effects of ccn1 and macrophage content on glioma virotherapy: A mathematical model. *Bulletin of Mathematical Biology* **77**(6), 984–1012.

Kalluri, R., Zeisberg, M., 2006. Fibroblasts in cancer. *Nat. Rev. Cancer.* **6**(5), 392–401.

Karev, G.P., Novozhilov, A.S., Koonin, E.V., 2006. Mathematical modelling of tumour therapy with oncolytic viruses: effects of parametric heterogeneity on cell dynamics. *Biology Direct* **1**(30), 1745–6150.

Kaufman, H.L., Kohlhapp, F.J., Zloza, A., 2016. Oncolytic viruses: a new class of immunotherapy drugs. *Cancer Immunotherapy* **15**(2), doi:10.1038/nrd4663.

Kauman, H., Kohlhapp, F., Zloza, A., 2015. Oncolytic viruses: a new class of immunotherapy drugs. *Nature Reviews* **14**, 642–662.

Kemler, I., Ennis, M., Neuhauser, C., Dingli, D., 2019. *In Vivo* imaging of oncolytic measles virus propagation with single-cell resolution. *Molecular Therapy: Oncolytics* **12**, 68–78.

Kim, P., Crivelli, J., Choi, I.K., Yun, C.O., Wares, J., 2015. Quantitative impact of immunomodulation versus oncolysis with cytokine-expressing virus therapeutics. *Mathematical Biosciences and Engineering* **12**(4), 841–858.

Kim, Y., Lee, H.G., Dmitrieva, N., Kim, J., Kaur, B., Friedman, A., 2014. Choindroitinase abc i-mediated enhancement of oncolytic virus spread and anti tumor efficacy: A mathematical model. *Plos One* **9**(7), 1–19.

Krabbe, T., Altomonte, J., 2018. Fusogenic viruses in oncolytic immunotherapy. *Cancers* **10**, 216.

Laaroussi, A.E.A., hia, M.E., Rachik, M., Benlahmar, E., Rachik, Z., 2014. Analysis of a mathematical model for treatment of cancer with oncolytic virotherapy. *Applied Mathematical Sciences* **8**(19), 929–940.

Laird, A., 1964. Dynamics of tumour growth. *Br. J. Cancer* **18**, 490–502.

Laird, A.K., 1965. Dynamics of tumour growth: Comparison of growth rates and extrapolation of growth curve to one cell. *British Journal of Cancer* **19**(2), 278–291.

Larson, C., Oronsky, B., Scicinski, J., Fanger, G.R., Stirn, M., Oronsky, A., Reid, T.R., 2015. Going viral: a review of replication-selective oncolytic adenoviruses. *Oncotarget* **6**(24).

Lawler, S., Speranza, M., Cho, C., Chiocca, E., 2017. Oncolytic viruses in cancer treatment: A review. *JAMA Oncol.* **3**(6), 841–849.

Lina, Y., Zhanga, H., Lianga, J., Lia, K., Zhua, W., Fub, L., Wangb, F., Zhengc, X., Shic, H., Wua, S., Xiaoa, X., Chena, L., Tanga, L., Yana, M., Yanga, X., Tana, Y., Qiua, P., Huanga, Y., Yind, W., Sua, X., Hue, H., Huf, J., Yana, G., 2014. Identification and characterization of alphavirus m1 as a selective oncolytic virus targeting zap-defective human cancers. *PNAS* **111**(42), E4504–E4512.

Lu, W., Zheng, S., Li, X.F., Huang, J.J., Zheng, X., Li, Z., 2004. Intra-tumor injection of h101, a recombinant adenovirus, in combination with chemotherapy in patients with advanced cancers: A pilot phase ii clinical trial. *World J Gastroenterol.* **10**(24), 3634–3638.

Macfarlane, R.G., Pilling, J., 1947. Fibrinolytic activity of normal urine. *Nature* **159**(4049), 779–779. doi:10.1038/159779a0.

Macnamara, C., Eftimie, R., 2015. Memory versus effector immune responses in oncolytic virotherapies. *J. Theor. Biol.* **377**, 1–9.

Malinzi, J., Eladdadi, A., Sibanda, P., 2017. Modelling the spatiotemporal dynamics of chemovirotherapy cancer treatment. *J. Biological Dynamics* **11**(1), 244–274.

Malinzi, J., Sibanda, P., Mambili-Mamboundou, H., 2015. Analysis of virotherapy in solid tumor invasion. *Mathematical Biosciences* **263**, 102–110.

Marchini, A., Scott, E., Rommelaere, J., 2016. Overcoming barriers in oncolytic virotherapy. *Viruses* **8**(9), 1–22.

Maroun, J., noz Alïa, M.M., Ammayappan, A., Schulze, A., Peng, K.W., Russell, S., 2017. Designing and building oncolytic viruses. *Future Medicine* **12**(4), 193–213.

Martins, M., Ferreira, S., Vilela, M., 2007. Multiscale models for the growth of avascular tumors. *Physics of Life Reviews* **4**(2), 128 – 156.

Meerani, S., Yao, Y., 2010. Oncolytic viruses in cancer therapy. *European Journal of Scientific Research* **40**(1), 156–171.

Nagano, S., Perentes, J.Y., Jain, R.K., Boucher, Y., 2008. Cancer cell death enhances the penetration and efficacy of oncolytic herpes simplex virus in tumors. *Cancer Research* **68**, 3795–3802.

Nowak, M.A., May, R.M., 2000. Virus dynamics: Mathematical principles of Immunology and Virology. Oxford University Press, Oxford.

Painter, K.J., Hillen, T., 2011. Spatio-temporal chaos in a chemotaxis model. *Physica D.* **240**, 363–375.

Paiva, L.R., Binny, C., Ferreira, S.C., Martins, M.L., 2009. A multiscale mathematical model for oncolytic virotherapy. *Cancer Research* **69**(3), 1205–1211.

Peng, K.W., TenEyck, C.J., Galanis, E., Kalli, K.R., Hartmann, L.C., Russell, S.J., 2002. Intraperitoneal therapy of ovarian cancer using an engineered measles virus. *Cancer Research* **62**(16), 4656–4662.

Peng, L., Trucu, D., Lin, P., Thompson, A., Chaplain, M.A.J., 2017. A multiscale mathematical model of tumour invasive growth. *Bulletin of Mathematical Biology* **79**(3), 389–429.

Perelson, A., Kirschner, D., Boer, R.D., 1993. Dynamics of HIV infection of $cd4^+$ t cells. *Math. Biosci.* **114**, 81–125.

Perelson, A., Neumann, A., Markowitz, M., Leonard, J., Ho, D., 1996. HIV-1 dynamics in vivo: Virion clearance rate, infected cell life-span, and viral generation time. *Science* **271**, 1582–1586.

Perumpanani, A., Sherratt, J., Norbury, J., Byrne, H., 1996. Biological inferences from a mathematical model for malignant invasion. *Invas. Metast.* **16**(4-5), 209–221.

Perumpanani, A., Simmons, D., Gearing, A., Miller, K., Ward, G., Norbury, J., Schneemann, M., Sherratt, J., 1998. Extracellular matrix-mediated chemotaxis can impede cell migration. *Proceed. Royal Soci. Biol. Sci.* **265**(1413), 2347–2352.

Petrie, R.J., Doyle, A.D., Yamada, K.M., 2009. Random versus directionally persistent cell migration. *Nature Reviews Molecular Cell Biology* **10**(8), 538–549.

Pierce, C.B., Shikes, R., Fink, L.M., 1978. Cancer: A Problem of Developmental Biology. Prentice-Hall, Englewood Cliffs, New Jersey.

Ploug, M., 2003. Structure-function relationships in the interaction between the urokinase-type plasminogen activator and its receptor. *Current Pharmaceutical Design* **9**(19), 1499–1528.

Preziosi, L., Tosin, A., 2009. Multiphase modelling of tumour growth and extracellular matrix interaction: mathematical tools and applications. *J. Math. Biol.* **58**, 625–656.

Psiuk-Maksymowicz, K., 2013. Multiphase modelling of desmoplastic tumour growth. *Journal of Theoretical Biology* **329**, 52–63.

Qian, B.Z., Pollard, J.W., 2010. Macrophage diversity enhances tumor progression and metastasis. *Cell* **141**(1), 39–51.

Ratajczyk, E., Ledzewicz, U., Leszczynski, M., Friedman, A., 2017. The role of tnf-α inhibitor in glioma virotherapy: A mathematical model. *Mathematical Biosciences and Engineering* **14**, 305–319.

Rioja, V.L.D., Isern, N., Fort, J., 2016. A mathematical approach to virus therapy of glioblastomas. *Biology Direct* **11**(1), pp. 12. doi:10.1186/s13062-015-0100-7.

Rodrigo, C.M., 2008. Local existence and uniqueness of regular solutions in a model of tissue invasion by solid tumours. *Mathematical and Computer Modelling* **47**(5-6), 604–613.

Rommelfanger, D., Offord, C., Dev, J., Bajzer, Z., Vile, R., Dingli, D., 2011. Dynamics of melanoma tumour therapy with vesicular stomatitis virus: explaining the variability in outcomes using mathematical modelling. *Gene Therapy* **19**, 543–549.

Russo, M., Siravegna, G., Blaszkowsky, L.S., Corti, G., Crisafulli, G., Ahronian, L.G., Mussolin, B., Kwak, E.L., Buscarino, M., Lazzari, L., Valtorta, E., Truini, M., Jessop, N.A., Robinson, H.E., Hong, T.S., Mino-Kenudson, M., Di Nicolantonio, F., Thabet, A., Sartore-Bianchi, A., Siena, S., Iafrate, A.J., Bardelli, A., Corcoran, R.B., 2016. Tumor heterogeneity and lesion-specific response to targeted therapy in colorectal cancer. *Cancer Discovery* **6**(2), 147–153. URL: https://cancerdiscovery.

aacrjournals.org/content/6/2/147, doi:10.1158/2159-8290.CD-15-1283, arXiv:https://cancerdiscovery.aacrjournals.org/content/6/2/147.full.pdf.

Santiago, D., Heidbuechel, J., Kandell, W., Walker, R., Djeu, J., Engeland, C., Abate-Daga, D., Enderling, H., 2017. Fighting cancer with mathematics and viruses. *Viruses* **9**, 239.

Sebastien, B., Clare, L., Afshin, B., Amanda, T., JML, E., Lynn, H., Hahnfeldt, P., 2014. Classical mathematical models for description and prediction of experimental tumor. *PLoS Comput Biol* **10**(8).

Seery, V., 2017. Intralesional therapy. *Clinical Journal of Oncology Nursing* **21**(4), 76–86.

Seymour, L., Fisher, K., 2016. Oncolytic viruses: finally delivering. *British Journal of Cancer* **114**, 357–361.

Sobel, G., Mohler, S., Jones, N., Dowdy, A., M.M., G., 1952. Urokinase: an activator of plasma profibrinolysin extracted from urine. *Am J Physiol* **171**(768-769).

Stamenkovic, I., 2000. Matrix metalloproteinases in tumor invasion and metastasis. *Seminars in Cancer Biology* **10**, 415–433.

Stolarska, M.A., Kim, Y., Othmer, H.G., 2009. Multi-scale models of cell and tissue dynamics. *Philos. Trans. A. Math. Phys. Eng. Sci.* **367**(1902), 3525–3553.

Stroock, D.W., Varadhan, S.S., 1997. Multidimensional Diffusion Processes. Springer, Heidelberg.

Swift, S.L., Stojdl, D.F., 2016. Big data offers novel insights for oncolytic virus immunotherapy. *Viruses* **8**(2), 45.

Sylwester, A., Wessels, D., Anderson, S., Warren, R., Shutt, D., Kennedy, R., Soll, D., 1993. HIV-induced syncytia of a T cell line form single giant pseudopods and are motile. *Journal of Cell Science* **106**(3), 941–953.

Szymanska, Z., Rodrigo, C.M., Lachowicz, M.A., Chaplain, M.A.J., 2009. Mathematical modelling of cancer invasion of tissue: the role and effect of nonlocal interactions. *World Scientific Publishing Company* **19**(2), 257–281.

Tjorve, K.M.C., Tjorve, E., 2017. The use of gompertz models in growth analyses, and new gompertz-model approach: An addition to the unified-richards family. *PLOS ONE* **12**(6), 1–17.

Trucu, D., Domschke, P., Gerisch, A., Chaplain, M.A., 2016. Mathematical Models and Methods for Living Systems. Springer International Publishing Switzerland. volume 2167 of *CIME Lecture Notes in Mathematics (eds. L. Preziosi et al.)*. chapter Multiscale Computational Modelling and Analysis of Cancer Invasion. pp. 275–321.

Trucu, D., Lin, P., Chaplain, M.A.J., Wang, Y., 2013. A multiscale moving boundary model arising in cancer invasion. *Multiscale Model. Simul.* **11**(1), 309–335.

Vähä-koskela, M., Hinkkanen, A., 2014. Tumour restriction to oncolytic virus. *Biomedicine* **2**, 163–194.

Venkatraman, L., Chia, S.M., Narmada, B.C., White, J.K., Bhowmick, S.S., Jr., C.F.D., So, P.T., Tucker-Kellogg, L., Yu, H., 2012. Plasmin triggers a switch-like decrease in thrombospondin-dependent activation of tgf-1. *Biophysical Journal* **103**(5), 1060 – 1068.

Webb, S., Sherratt, J., Fish, R., 1999. Alterations in proteolytic activity at low ph

and its association with invasion: a theoretical model. *Clin. Experim. Metast.* **17**(5), 397–407.

Weiger, M.C., Vedham, V., Stuelten, C.H., Shou, K., Herrera, M., Sato, M., Losert, W., Parent, C.A., 2013. Real-time motion analysis reveals cell directionality as an indicator of breast cancer progression. *PLOS ONE* **8**(3), 1–12.

Weinberg, R.A., 2006. The Biology of Cancer. Garland Science, New York.

Wodarz, D., 2016. Computational modelling approaches to the dynamics of oncolytic viruses. *Wiley Interdiscip. Rev. Syst. Biol.* **8**, 242–252.

Wodarz, D., Chan, C.N., Trinité, B., Komarova, N.L., Levy, D.N., 2014. On the laws of virus spread through cell populations. *J Virol* **88**(22), 13240–8.

Wodarz, D., Hofacre, A., Lau, J.W., Sun, Z., Fan, H., Komarova, N.L., 2012. Complex spatial dynamics of oncolytic viruses in vitro: Mathematical and experimental approaches. *PLoS Comput Biol* **8**(6).

Wodarz, D., Komarova, N., 2009. Towards predictive computational models of oncolytic virus therapy: Basis for experimental validation and model selection. *Plos One* **4**(1), e4271.

Wollmann, G., Tattersall, P., AN, A.V.D.P., 2005. Targeting human glioblastoma cells: comparison of nine viruses with oncolytic potential. *J Virol* **79**(10), 6005–22.

Wong, H., Lemoine, N., Wang, Y., 2010. Oncolytic viruses for cancer therapy: overcoming the obstacles. *Viruses* **2**(1), 78–106.

Wu, P.H., Giri, A., Sun, S.X., Wirtz, D., 2014. Three-dimensional cell migration does not follow a random walk. *Proceedings of the National Academy of Sciences* **111**(11), 3949–3954.

Yosida, K., 1995. Functional Analysis. 1431-0821. 6 ed., Springer-Verlag Berlin Heidelberg.

Zeh, H., Downs-Canner, S., McCart, J., Guo, Z., Rao, U., Ramalingam, L., Thorne, S., Jones, H., Kalinski, P., Wieckowski, E., O'Malley, M., Daneshmand, M., Hu, K., Bell, J., Hwang, T., Moon, A., Breitbach, C., Kirn, D., Bartlett, D., 2015. First-in-man study of western reserve strain oncolytic vaccinia virus: safety, system spread, and anti tumour activity. *Molecular Therapy* **23**(1), 2020–214.

Zhang, J.M., An, J., 2007. Cytokines, inflammation and pain. *Int Anesthesiol Clin* **45**(2), 27–37.